Dissertation

submitted to the

Combined Faculties for the Natural Sciences and for Mathematics

of the Ruperto-Carola University of Heidelberg, Germany

for the degree of

Doctor of Natural Sciences

Put forward by

Diplom-Physikerin: Nadine Hoffmann

Born in: Landau in der Pfalz

Oral examination: 29.04.2015

Experimental Study on the Contact Freezing of Supercooled Micro-Droplets in Electrodynamic Balance

Referees: Prof. Dr. Thomas Leisner
Prof. Dr. Klaus Pfeilsticker

Zusammenfassung

Im Rahmen dieser Arbeit wurde die heterogene Eisnukleation unterkühlter Mikrotropfen untersucht, welche durch den Kontakt mit eisaktiven Partikeln (ice nucleating particle (INP)) ausgelöst wurde. Die Kontaktgefrierergebnisse wurden mit den Ergebnissen von Immersionsgefrierexperimenten verglichen. Kontaktgefrieren ist die bisher am wenigsten verstandene heterogene Gefriermode. Der gleichen INP löst in der Kontaktgefriermode bei höheren Temperaturen Gefrieren aus als in der Immersionsmode.
Es wurde ein elektrodynamischer Levitator verwendet um einzelne, unterkühlte Mikrotropfen aus deionisiertem Wasser zu speichern. Der Tropfen ist einem Aerosolstrom ausgesetzt, der Partikel beinhaltet, die nach ihrer Mobilität sortiert wurden. Das Einbringen eines Tropfens in die EDB und das Detektieren von Gefrierereignissen ist automatisiert. In diesem Experiment ist es möglich die Kollisionsrate der Partikel zu berechnen und damit eine Wahrscheinlichkeit für das Gefrieren bei einem einzelnen Kontakt anzugeben. Des Weiteren können mit diesem experimentellen Aufbau Experimente in der Immersionsmode durchgeführt werden.
Als eisaktive Partikel wurden einige atmosphärisch relevante Mineralienstaubkomponenten (Hämatit, Feldspat, Illit, Kaolinit), Cellulose, SNOMAX®, Birkenpollen-Wasch-Wasser und eine Mischung aus Illit und Birkenpollen-Wasch-Wasser untersucht. Die resultierenden Kontaktgefrierwahrscheinlichkeiten zeigen eine Temperatur-, Partikelgrößen- und Materialabhängigkeit. Um die Ergebnisse aus Immersions- und Kontakgefrierexperimenten vergleichen zu können, wird die Dichte an eisaktiven Stellen (Ice Nucleating Active Site density) berechnet. Mit Ausnahme von SNOMAX® und Birkenpollen-Wasch-Wasser zeigen alle untersuchten Materialien eine höhere Anzahl an eisaktiven Stellen in der Kontaktgefriermode als in der Immersionsmode.

Abstract

The aim of this work, was to investigate the heterogeneous ice nucleation of supercooled micro-droplets induced by contact with an ice nucleating particle (INP). The contact freezing is poorly quantified but can be potentially important for understanding precipitation mechanisms via cloud glaciation in mixed clouds. The contact freezing results are compared to results of freezing experiments in the immersion mode. The same INP is ice active at higher temperatures in the contact mode than in the immersion mode.
An electrodynamic balance was used to levitate single, supercooled micro-droplets of deionized water. The droplet is exposed to a flow of mobility-selected aerosol particles. The injection of droplets and the detection of freezing events is automated. In this experiment, it is possible to calculate the collision rate separately, and the probability of freezing on a single contact. Furthermore, immersion freezing experiments are performed in the same experimental setup, and a direct comparison between immersion and contact mode is possible.
As ice nucleating particles, some relevant atmospheric minerals (hematite, feldspar, illite, kaolinite), cellulose, SNOMAX®, birch pollen washing water and a mixture of illite and birch pollen washing water have been investigated. The resulting contact freezing probabilities show a temperature, particle size, and material dependency. For comparison of immersion and contact freezing results an Ice Nucleating Active Site (INAS) density has been calculated. With exclusion of SNOMAX® and birch pollen washing water, all particles have been shown to be more ice active in the contact freezing mode than in immersion mode.

Contents

1 Introduction and motivation

Climate change and, consequently, climate research are becoming increasingly important, not least because of the looming threat of global warming and subsequent increase in impact of certain types of natural disasters. As part of the climate system, clouds and microscopic airborne solid particles or liquid droplets, so-called aerosols, are important components of the atmosphere.

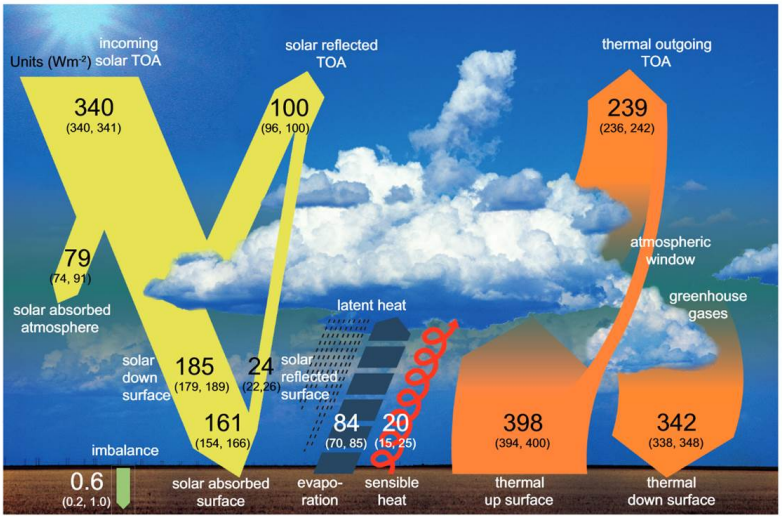

Figure 1.1: Schematic diagram of the global energy balance of the Earth [Wild et al., 2013]

Clouds influence both the Earth's radiation budget and its hydrological cycle. They cover about half of the planet [Salby, 2012], and depending on their top temperature and height, clouds can cool or warm the Earth's surface.

Figure 1.1 shows a schematic diagram of the global mean energy balance of the Earth [Wild et al., 2013]. Clouds and the atmosphere reduce the amount of incoming solar radiation reaching the Earth's surface from about $340\,\mathrm{Wm}^{-2}$ to about $185\,\mathrm{Wm}^{-2}$. The numbers given in Wild et al. [2013] are very close to the numbers of Trenberth et al. [2009], but the amount of outgoing longwave radiation is shown in more detail in Trenberth et al. [2009]. They estimate that about $169\,\mathrm{Wm}^{-2}$ of the total outgoing longwave radiation ($239\,\mathrm{Wm}^{-2}$) is emitted by the atmosphere and about $30\,\mathrm{Wm}^{-2}$ is emitted by clouds.

The aerosol particles in the atmosphere can have a direct influence on solar radiation due to scattering or absorption, or an indirect influence by serving as cloud condensation nuclei (CCN) or ice nucleating particles (INP) [Seinfeld and Pandis, 2006]. Figure 1.2 shows the global average radiative forcing estimated in 2011 relative to the year 1750 [Stocker et al., 2013]. It is easy to see that particularly anthropogenic gases like carbon dioxide (CO_2) and nitrous oxide (N_2O) increase the warming effect vastly. Mineral dust, sulfate (SO_3), nitrate (NH_3), and organic carbon compensate somewhat for the warming effect of black carbon, but this compensation is negligible, as is the cooling effect of clouds. In total, the anthropogenic warming effect has been increasing continuously since the begin of the industrial era in the 1750s.

Whether aerosol particles act as CCN or INP depends on the aerosol type and prevailing conditions like temperature and humidity. Another factor is the variation of the number concentration of aerosols. It can change the cloud droplet population and size, which influences the albedo of a cloud and its areal extent [Seinfeld and Pandis, 2006].

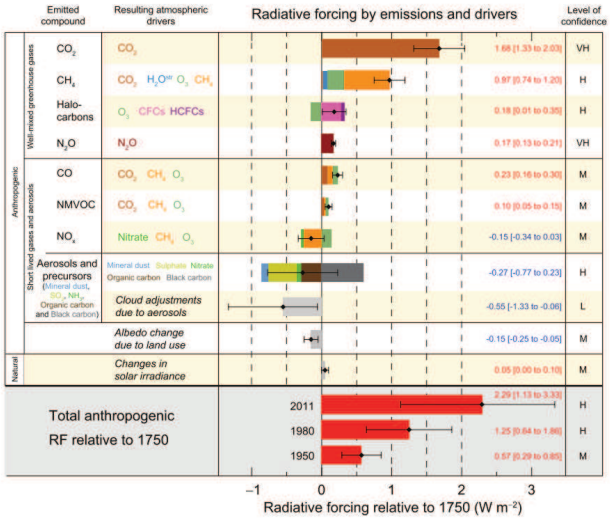

Figure 1.2: Radiative forcing estimates in 2011 relative to 1750. The values are global average radiative forcing, partitioned according to the emitted compounds or processes that result in a combination of drivers [Stocker et al., 2013].

Ice formation in clouds is important for the radiative properties of clouds as well as for the formation of precipitation. Since most weather-relevant processes happen in the lower or middle troposphere, the temperature is not low enough for homogeneous freezing, and ice nucleating particles are necessary to glaciate a cloud [Roedel, 2000]. Currently, not all ice formation processes in clouds are understood, and to support

further research on this topic, the Deutsche Forschungsgesellschaft (DFG) funds the Ice Nuclei research UnIT (INUIT) to study heterogeneous ice formation in the atmosphere. The project is split into three working packages: laboratory studies, field measurements, and modeling, combining nine research projects. For the laboratory studies, the project focuses on reference aerosols like hematite, illite, kaolinite and feldspar as atmospherically relevant aerosol components, and uses SNOMAX® to represent bacteria. Since every participating institute uses the same aerosol, it is possible to compare the results of different experimental methods.

As part of research project 7, conducted as "Comprehensive process studies of heterogeneous ice nucleation: from single cloud droplets to cloud simulation", this thesis analyzes the contact freezing of single cloud droplets at the Institute for Meteorology and Climate Research – Atmospheric Aerosol Research (IMK-AAF), Karlsruhe Institute of Technology (KIT). Contact freezing is one of four heterogeneous freezing modes and, up to now, the least understood [Ladino Moreno et al., 2013]. But it is potentially the most important freezing mode, since droplets freeze in the contact mode at higher temperatures than in the immersion mode for the same INP (e.g. Shaw et al. [2005], Diehl et al. [2002]).

The question, whether the contact freezing mode is relevant for the freezing processes in the atmosphere has not been answered until now [Ladino Moreno et al., 2013], and there are controversial discussions about that. Some studies have found that the contact freezing mode is likely responsible for the glaciation of certain cloud regions (e.g. Hobbs and Rangno [1985], Ansmann [2005], Seifert et al. [2011]). In contrast, other studies (e.g. Twohy et al. [2010], Philips et al. [2007]) found the opposite. Obviously, more research is necessary.

Several groups have been investigating the contact freezing mode with different experimental setups. For example, Pitter and Pruppacher [1973], Levin and Yankofsky [1983], Diehl et al. [2002] and von Blohn et al. [2005] used a wind tunnel. Another approach used cloud chambers like the CoLlision Ice Nucleation CHamber (CLINCH) [Ladino et al., 2011a] or the Contact Ice Nucleation Chamber (CINC) [Niehaus et al., 2014b]. In other experiments, a cold plate (e.g. Shaw et al. [2005], Durant and Shaw [2005], Fornea et al. [2009]) was used. Levitating single droplets in an acoustic levitator (e.g. Ettner et al. [2004]) or an electrodynamic balance, as used in this experiments and, for example, in Svensson et al. [2009], is another method to investigate the contact freezing mode.

The experimental setup of the work in hand leverages of an electrodynamic balance (EDB) to levitate single micro-droplets of deionized water, and an aerosol system to produce a mobility-selected particle flow. The particle flow passes through the EDB, and some of the particles collide with the droplet and eventually initialize freezing. The experimental setup was built by Daniel Rzesanke [Rzesanke, 2012], who used it first for contact freezing experiments. Following his work, I started with experiments for my diploma thesis, and afterward for my doctoral thesis. During this time, considerable improvements have been introduced into the setup, including

aerosol generation, humidification of the aerosol path to reduce droplet evaporation, and an electrostatic precipitator for fast filtering of charged aerosol particles.

The difficulty in all these methods is determining, how many particles have collided with the droplet, and whether freezing occurred on first contact, or whether further contacts are necessary to initiate freezing. Most of the past studies reported the fraction of frozen droplets as the only measurable experimental quantity, but do not quantify the particle-droplet-collisions. Without this information, a comparison of results should be approached with caution. To consider the contact freezing mode in models, it is also necessary to know the collision rate and freezing probability separately. A major advantage of the experimental setup used in this work is that it is possible to calculate the collision rate of every single experiment, and it is also possible to verify the calculated collision rate by ejecting droplets onto a Si-wafer and counting the collected particles (described in section 4.3).

The objective of this thesis was to investigate the "INUIT reference aerosols" in the contact freezing mode, and to determine a probability for freezing on a single contact (henceforth referred to as "contact freezing probability"). Since it was possible to give precise information about the collision rate, these results can also be used for modeling.

In the 2nd chapter, the formation of clouds is described briefly, the homogeneous and heterogeneous nucleation are explained, and the contact freezing mode and its role in clouds is discussed. At the end of that chapter I will give an overview of atmospheric aerosols and their sources, and the aerosol materials used in this work are described.

Chapter 3 includes all information about the experimental setup and the devices used for the size selection and counting of the aerosol particles.

In the 4th chapter, the possible freezing scenarios are discussed and the statistical description of contact and immersion freezing of droplet ensembles is given, followed by the description of the experimental verification of the collection efficiency and the uncertainty analysis.

In chapter 5 the experimental results are shown, and the possibility to compare contact and immersion freezing results is discussed.

Chapter 6 contains summary and conclusion as well as providing an outlook for the next stage of INUIT.

2 Clouds and aerosols

In this chapter, the formation of clouds and the properties of water in gas, liquid, and solid phase are discussed. The contact freezing mode and its potential role in clouds is described. These sections follow mainly Pruppacher and Klett [2004] and Seinfeld and Pandis [2006]. At the end of the chapter, I will give an overview of atmospherically relevant aerosol particles and their sources, and the aerosol materials used in these measurements are discussed. Parts of the following sections are similar to the relevant sections for ice nucleation and aerosols in my diploma thesis [Hoffmann, 2012].

2.1 Cloud formation

In this section, I will give a brief overview of cloud formation processes in "warm" tropospheric clouds, since contact nucleation would only be relevant there. A detailed description can be found in Seinfeld and Pandis [2006] or Mason [1971]. For water droplet formation in particle-free air, a supersaturation of water vapor at several hundred percent is necessary [Roedel, 2000]. The actual number depends on the droplet radius – the smaller the radius, the higher the needed supersaturation. Much more energy-efficient, and already possible at slightly supersaturated conditions, is the heterogeneous condensation of water vapor on cloud condensation nuclei (CCN).

To supersaturate the water vapor in an air parcel, the amount of water must remain stable when the temperature decreases. The cooling of the air parcel can happen isobarically, for example, as a result of moving horizontally over a cooler surface or adiabatic expansion.

The growth rate of a single droplet is a function of the cooling rate, temperature and vapor density. The description of a large population of single droplets, like in a cloud, is much more complicated. Now the growth rate additionally depends on the concentration and size distribution of the droplets, the type of ice nucleating particles, and the scale and intensity of the turbulence in the cloud [Mason, 1971].

Let's first look at the growth rate of a single droplet. The change of the droplet's mass m by time is given as:

$$\frac{dm}{dt} = 2\pi D_p D_v (c_{w,\infty} - c_w) \tag{2.1}$$

with the droplet diameter D_p, the coefficient of diffusion of water vapor in air D_v, and $c_{w,\infty}$ and c_w the concentration of water in the environment far away from the droplet and the equilibrium water vapor concentration of the droplet, respectively (both given in mass per volume of air) [Seinfeld and Pandis, 2006]. Using the ideal-gas law and the Clausius-Clapeyron equation, the growth rate of an atmospheric droplet can be written as [Seinfeld and Pandis, 2006]:

$$D_p \frac{dD_p}{dt} = \frac{S_{\nu,\infty} - \exp\left(\frac{4M_w\sigma_w}{RT_\infty\rho_w D_p} - \frac{6n_s M_w}{\pi\rho_w(D_p^3 - d_u^3)}\right)}{\frac{\rho_w RT_\infty}{4p^\circ(T_\infty)D'_\nu M_w} + \frac{\Delta H_\nu \rho_w}{4k'_a T_\infty}\left(\frac{\Delta H_\nu M_w}{T_\infty R} - 1\right)} \tag{2.2}$$

with $S_{\nu,\infty}$ the environmental saturation, M_w the molecular weight of water, σ_w the solution surface tension, T_∞ the temperature of the environment, n_s the number of solute moles, d_u the diameter of the insoluble particle, $p^\circ(T_\infty)$ the saturation vapor pressure, D'_ν the modified diffusivity of water vapor (according to [Fukuta and Walter, 1970]), $\Delta H_\nu \rho_w$ the latent heat for water evaporation, and k'_a the effective thermal conductivity of air.

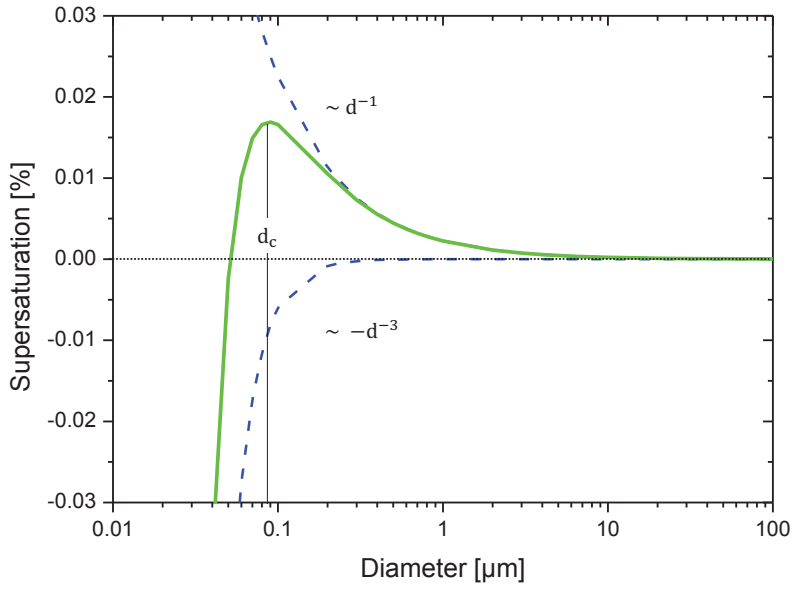

Figure 2.1: Influence of Kelvin effect and solute effect on the droplet growth [Seinfeld and Pandis, 2006], calculated for $5 \cdot 10^{-18}$ g NaCl in a droplet at a temperature of 293 K

The first and second term in the denominator correspond to the diffusivity of water vapor and temperature differences between the droplet and its environment.

The first term in the exponent gives the contribution of the Kelvin effect. This effect describes how a curved surface reduces the strength of molecular bonds, and

consequently, the vapor pressure over a convex interface is always higher than the vapor pressure over a flat surface.

The second term in the exponent accounts for the Raoult's law, which describes the vapor pressure reduction over an ideal solution. This solute effect is necessary to describe droplets with dissolved substances like salts or acids. The Kelvin effect and Raoult's law are combined in the so-called Köhler equation [Pruppacher and Klett, 2004], shown in figure 2.1. If the droplet diameter d is smaller than a critical diameter d_c, a thermodynamic equilibrium prevails and the growth of the droplet is reversible. If $d > d_c$, the thermodynamic equilibrium is gone and the droplet can grow as long as it is in a supersaturated environment.

In a droplet population, Seinfeld and Pandis [2006] show that in the absence of condensation, the saturation varies linearly with the updraft velocity and is decreased by water condensation. They suggest that the supersaturation inside the cloud is the result of a balance between the cooling rate and the liquid water increase. Particles with critical supersaturation lower than the maximum supersaturation become activated, grow, and become cloud droplets.

The activated droplets can reach a size of about 20 µm to 100 µm in diameter; by vapor condensation under particularly favorable conditions, the droplets can grow up to 500 µm. However, outside of the tropics, a droplet growth in the range between 500 µm and 5 mm is needed to initiate precipitation, which cannot be achieved by condensation alone [Malberg, 2007].

In most cases, other processes are needed to allow droplets growth to a rain drop size. These are the coalescence between colliding droplets and the Wegener-Bergeron-Findeisen process, which postulates that rain with larger droplets occurs due to ice crystal growth on the expense of liquid droplets. Because of the lower saturation of vapor pressure over ice, ice crystals can grow faster than water droplets. Large ice crystals fall out, and depending on the temperature profile, reach the Earth's surface as snow or rain.

2.2 Cloud microphysics

2.2.1 Liquid water and water vapor

The amount of water a particle-free air parcel is carrying at a constant pressure, depends on its temperature. The relative humidity (RH [%]) gives the ratio of the partial pressure of water vapor to the saturation vapor pressure of water at a certain temperature, and consequently the amount of water molecules per air volume [Seinfeld and Pandis, 2006].

For constant pressure, water vapor will condense on a surface at a certain temperature (so-called dewpoint) where RH = 100% [Seinfeld and Pandis, 2006], or will freeze on a surface without going into liquid phase (so-called frost point). To prevent ice grow in the setup, the dew and frost point are important to know to perform the experiments.

Under standard conditions, water is liquid down to a temperature of 0 °C, and would change to the solid phase for subzero temperatures. In the atmosphere, liquid cloud droplets can exist down to about −36 °C (e.g. Pruppacher and Klett [2004]), and in exceptional cases even down to −40.7 °C [Heymsfield and Miloshevich, 1993]. Obviously, water can exist in a supercooled, metastable phase before freezing starts [Pruppacher and Klett, 2004]. The explanation for this behavior is that a system has to overcome an energy barrier before transforming into the solid phase, which has less potential energy.

Liquid water is a mixture of single water molecules and clusters which permanently build and decay. The number of clusters existing simultaneously at a certain time is temperature dependent [Némethy and Scheraga, 1964]. The lower the temperature, the higher the number of simultaneously existing clusters. In supercooled conditions, the hydrogen bonds live longer at higher supercooling. At one point the molecules build a cluster of critical size. Now the cluster starts to grow, and will not decay again.

2.2.2 Homogeneous freezing

A pure supercooled water drop can freeze because of the local fluctuation of density and temperature, which causes the formation of a nucleus of critical size. This mechanism is described by the classical theory of homogeneous nucleation and is based on three assumptions: a) The nucleus has a spherical shape, b) the density and the surface tension can be described by a macroscopic quantity, and c) the sizes of the nuclei are distributed according to the Boltzmann law [Pruppacher and Klett, 2004].

Since the volume and the temperature of the total system remains constant during the formation of nuclei, the process can be described by the free energy $G = U - TS$ [Nolting, 2012] with the inner energy U, temperature T, and entropy S. To start the homogeneous nucleation process, the system has to overcome two energy barriers: one to create an ice nucleus (ΔG), and one to enable water molecules to break the bond with the surrounded molecules and form a bond to the nucleus (ΔF_{diff}).

The free energy of a pure liquid substance (here supercooled water) of i molecules is given by $G_l = i \cdot \mu_l$. The free energy of the same liquid substance at the same temperature, but with a solid i-mer is given by $G_{l/s} = i_l \cdot \mu_l + i \cdot \mu_s + A_{\text{si}} \cdot \sigma_{l/s}$. Here μ_l and μ_s are the chemical potential of the liquid (in the following with index "w" for water) and solid (in the following with index "i" for ice), respectively. A_{si} is the

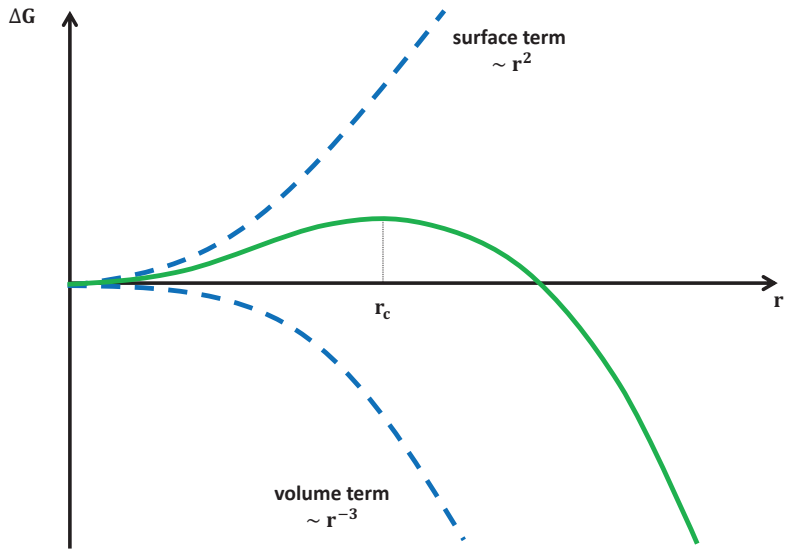

Figure 2.2: Free energy of the ice nucleus formation depending on the ice nucleus radius [Pruppacher and Klett, 2004]

surface of the ice nucleus and $\sigma_{l/s}$ the interfacial energy between ice nucleus and liquid phase.

The free energy difference ΔG of supercooled water with and without a spherical ice nucleus with a radius r is consequently given by:

$$\Delta G = -\frac{4}{3}\pi \cdot r^3 \cdot n_i(\mu_w - \mu_i) + \Omega \cdot \sigma_{i/w} \tag{2.3}$$

with the number concentration of water molecules n_i, and the surface area of the i-mer Ω.

The equation consists of two terms (depicted in figure 2.2). The first term describes the free energy decrease caused by the change in chemical potential due to the conversion from liquid to solid phase (volume-dependent term). The second term describes the energy required to create the surface (surface-dependent term). ΔG_c achieves a maximum at a certain critical nucleus radius, but the critical size is an unstable equilibrium. Should one molecule leave the surface of the nucleus, the nucleus would decay again. Should one more molecule attach to the nucleus of critical size, the nucleus would grow.

Finding the maximum of the curve yields a critical nucleus radius r_c and energy barrier ΔG_c [Seinfeld and Pandis, 2006]:

$$r_c = \frac{2\sigma_{i/w}}{n_i(\mu_w - \mu_i)} \quad \text{and} \quad \Delta G_c = \frac{4\pi}{3}\sigma_{i/w} r_c^2 \tag{2.4}$$

Using the Kelvin equation [Seinfeld and Pandis, 2006], the free energy change due to formation of a nucleus can be written as:

$$\Delta G_c = \frac{16\pi}{3} \frac{V_M^2 \sigma_{i/w}^3}{(kT \ln(S))^2} \tag{2.5}$$

V_M is the molar volume of ice, S gives the ratio of vapor pressure over water and ice, and k is the Boltzmann constant.

As mentioned above, the second energy barrier that has to be overcome is associated with the diffusion energy ΔF_{diff}. According to Zobrist et al. [2007] ΔF_{diff} is given as:

$$\Delta F_{\text{diff}}(T) = \frac{\partial \ln(D_\nu(T))}{\partial T} kT^2 \tag{2.6}$$

$D_\nu(T)$ describes the temperature dependent diffusion coefficient of water.

The bonding energy of the nucleus is not experimentally measurable. What is measurable, is the rate of the phase transformation events from liquid to solid phase at a certain temperature, the so-called homogeneous freezing rate J. This rate is described by a statistical first order process similar to radioactive decay. Assuming an ensemble of identical elementary volumes V, the number of unfrozen volumes N_u will decay with time in the following way:

$$\frac{dN_u}{dt} = -J_{\text{hom}} \cdot V \cdot N_u \tag{2.7}$$

Integration yields:

$$\int_{N_0}^{N_u} \frac{dN_u'}{N_u'} = -\int_0^t J_{\text{hom}} \cdot V dt' \quad \Rightarrow \quad \ln\left(\frac{N_u}{N_0}\right) = -J_{\text{hom}} \cdot V \cdot t \tag{2.8}$$

J_{hom} gives the nucleation rate coefficient, which describes the rate of ice nuclei appearing. Every elementary volume containing at least one critical nucleus would freeze. The nucleation rate is given (e.g. in [Pruppacher and Klett, 2004]) as:

$$J = 2n_w \frac{kT}{h} \frac{\rho_w}{\rho_i} \sqrt{\frac{\sigma_{i/w}}{kT}} \exp\left(-\frac{\Delta G + \Delta F_{\text{diff}}}{kT}\right) \tag{2.9}$$

Here n_w describes the number of water molecules, which are in contact with the ice nucleus surface, and ρ_w and ρ_i are the density of water and ice, respectively. The system tries to redress the energy barrier with the frequency $\frac{kT}{h}$.

A precise description and derivation of the homogeneous freezing rate coefficient are given in Pruppacher and Klett [2004] or Seinfeld and Pandis [2006], for example.

2.2.3 Heterogeneous nucleation of ice

In heterogeneous freezing processes, ice nucleating particles (INP) reduce the energy needed to form an ice nucleus, which enables heterogeneous freezing to be initiated at higher temperatures than homogenous freezing. Since in the lower and middle troposphere the temperature is not low enough for homogeneous freezing, the heterogeneous freezing processes are important for the ice formation in clouds at those levels [Seinfeld and Pandis, 2006].

The four heterogeneous freezing modes are depicted in figure 2.3. Deposition freezing describes the ice formation from the vapor phase. In the condensation freezing mode, the water vapor condenses on the INP first, and the freezing starts in the liquid phase. In case the INP is already immersed in a water droplet at temperatures above 0 °C, and the INP initializes freezing when the droplet becomes cooled down to subzero temperatures, the freezing is said to be in the immersion mode. If the freezing is initialized by the contact of an INP with a supercooled droplet, the droplet freezes due to contact freezing mode. [Vali et al., 2014]

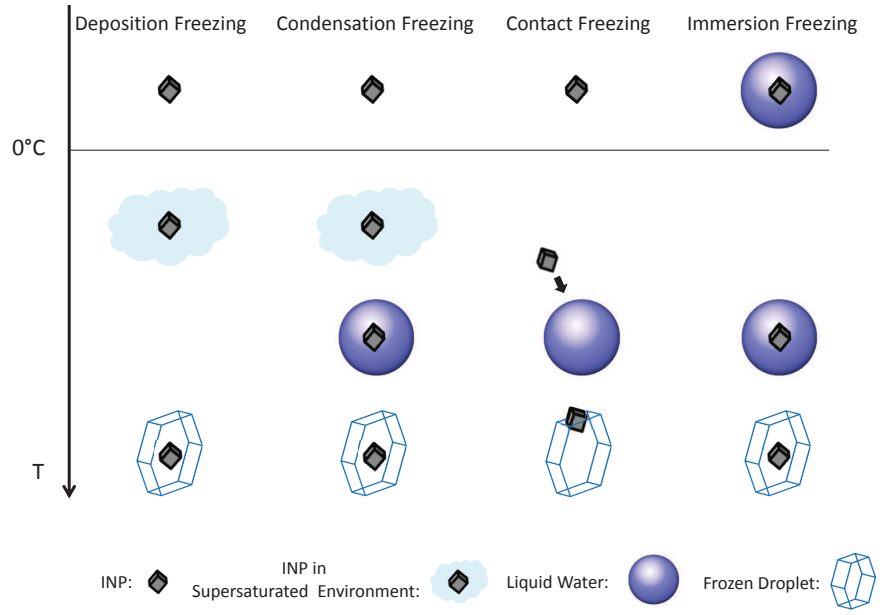

Figure 2.3: Schematic diagram of heterogeneous freezing mechanisms [Vali, 1985]

In the following, the heterogeneous ice nucleation is discussed briefly. Detailed descriptions are given in, e.g. Mason [1971], Seinfeld and Pandis [2006], or Pruppacher and Klett [2004].

According to the Volmer-Weber-nucleation-theory [Volmer, 1939], the free energy transformation during the heterogeneous nucleation processes can be described following the situation shown in figure 2.4.

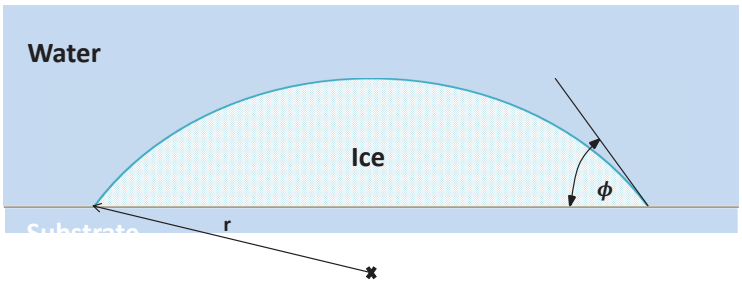

Figure 2.4: Spherical ice nucleus in contact with liquid water and substrate [Mason, 1971]

A spherical ice nucleus is located on a plane substrate, and is surrounded by supercooled water. The contact angle φ between substrate and ice nucleus is described by [Fletcher, 1962]:

$$m = \cos(\varphi) = (\sigma_{p,w} - \sigma_{p,i}) / \sigma_{i,w} \tag{2.10}$$

Indices i and w mean ice and supercooled water, respectively. The substrate represents an ice nucleating particle, which is described by index p. $\sigma_{p,w}$, $\sigma_{p,i}$ and $\sigma_{i,w}$ give the energy of interfaces between particle and supercooled water, particle and ice nucleus, and ice nucleus and supercooled water, respectively.

The change of the free energy due to the formation of an ice nucleus is given by [Mason, 1971]:

$$\Delta G = \rho_i \frac{\mathrm{N_A}}{M_i} (\mu_i - \mu_w) V_i + \sigma_{i,w} A_{i,w} + (\sigma_{p,i} - \sigma_{p,w}) A_{p,i} \tag{2.11}$$

$A_{i,w} = 2\pi r^2 (1 - m)$ and $A_{p,i} = \pi r^2 (1 - m^2)$ are the surface area of interfaces between ice nucleus and supercooled water, and particle and ice nucleus, respectively. $V_i = \frac{\pi r^2}{3} (2 + m) (1 - m)^2$ gives the volume of the spherical ice nucleus and M_i describes the molar mass of ice.

The critical nucleus radius r_{crit} results from $\partial / \partial r (\Delta G) = 0$ [Mason, 1971]:

$$r_{\mathrm{crit}} = \frac{2 M_i \sigma_{i,w}}{\rho_i R T \ln(S)} \tag{2.12}$$

Substituting 2.12 into 2.11 gives the radius dependent energy needed to form an ice nucleus in heterogeneous nucleation processes [Mason, 1971]:

$$\Delta G_{\mathrm{het}} = \frac{16 \pi M_i^2 \sigma_{i,w}^3}{3 (\rho_i R T \ln(S))^2} f(m) \tag{2.13}$$

The free energy of a critical nucleus formation in a heterogeneous process differs from a homogeneous process only by a factor $f(m) = \frac{1}{4}(2+m)(1-m)^2$ [Mason, 1971].

The factor $f(m)$ is a number between 0 and 1, whereby the limiting case $f = 0$ means a contact angle of $\varphi = 0°$ and $f = 1$ a contact angle of $\varphi = 180°$. In reality, the particle usually does not have a planar surface as assumed in theory. Assuming the INP is a sphere with radius r_p, $f(m)$ changes to $f(m, x)$ which is given by [Mason, 1971]:

$$f(m,x) = \frac{1}{2}\left[1 + \left(\frac{1-mx}{g}\right)^3 + x^3\left(2 - 3\delta + \delta^3\right) + 3mx^2\left(\delta - 1\right)\right] \tag{2.14}$$

with $\delta = \frac{x-m}{g}$, $g = (1 + x^2 - 2mx)^{\frac{1}{2}}$ and the rate $x = \frac{r_p}{r_{\text{crit}}}$.

Analogous to the homogeneous nucleation coefficient (eq. 2.9), the nucleation rate coefficient for the heterogeneous case is given by:

$$j_{\text{het}} = \frac{k_B T}{h} \cdot \pi r_{\text{crit}}^2 \cdot n_w \cdot \exp\left(\frac{-\Delta G_{\text{het}} + \Delta F_{\text{diff}}}{k_B T}\right) \tag{2.15}$$

2.3 Contact freezing and its potential role in clouds

The first references to the contact freezing mechanism and experimental setups to investigate it were described for example by Rau [1950], Fletcher [1969], Pitter and Pruppacher [1973], Cooper [1974], or Fukuta [1975]. Rau [1950] conducted the first experiments using a closed cooling chamber, where no contamination from room air was possible. The review paper of Ladino Moreno et al. [2013] gives an overview of experimental setups used to investigate contact freezing, hypotheses to explain this freezing mode, and the current understanding in respect to the relevance in clouds. In the following, I will give a brief overview of experimental methods to compare them with the setup used in this work.

Some research groups have used a wind tunnel to investigate contact freezing (e.g., Pitter and Pruppacher [1973], Levin and Yankofsky [1983], Diehl et al. [2002], and von Blohn et al. [2005]). In this kind of experimental setup, a particle containing flow pass through a tube from below, and balance a droplet against gravity. Some of the particles collide with the droplet, and eventually initialize freezing. Pitter and Pruppacher [1973] found for kaolinite and montmorillonite a "significantly higher efficiency when they act by contact with the surface of a supercooled drop than when they act from inside the drop" (figure 2.5).

Levin and Yankofsky [1983] have investigated bacteria cells in the contact and immersion mode. The authors observed that the contact freezing mode was more efficient by about 2 °C. Diehl et al. [2002] and von Blohn et al. [2005] investigated

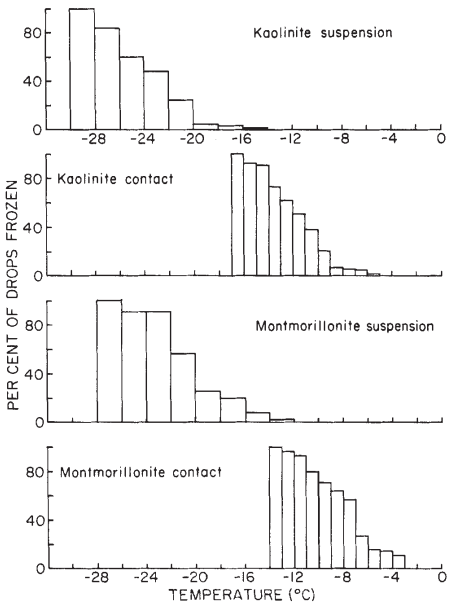

Figure 2.5: "Comparison between the freezing temperature of drops frozen by contact with clay particles and freezing temperature of drops frozen by clay particles suspended in them. Wind tunnel experiments." [Pitter and Pruppacher, 1973]

different types of pollen in the contact and immersion mode. All pollen types showed a higher median freezing temperature (temperature at which 50% of the observed droplets are frozen) in the contact mode than in the immersion mode.

Another method uses a cloud chamber like the CoLlision Ice Nucleation CHamber (CLINCH) (Ladino et al. [2011b] and Ladino et al. [2011a]) (figure 2.6). CLINCH is a continuous flow chamber consisting of two parallel plates (variable between 20 cm and 80 cm) which are temperature controlled with a cryostat. The droplets are injected at the top of the chamber, and the aerosol particles carried by an air flow, enter the chamber through two inlets at the head of the chamber. While moving through the chamber, the droplets can interact with the aerosol particles, and freezing can be detected by an Ice Optical DEtector (IODE). [Ladino et al., 2011a]

Ladino et al. [2011a] found that the particle size is an important parameter for contact freezing. For particles of 800 nm the on-set temperature for freezing was 7 °C higher than for 400 nm. The authors compared their results to the immersion freezing results of [Lüönd et al., 2010], and can only observe a difference between contact and immersion mode for frozen fractions lower than 0.4, but in that range "there are some hints for contact freezing being more efficient than immersion freezing, but these comparisons have to be taken with caution because of the large measurement uncertainties of immersion freezing at the lowest frozen fraction" [Ladino et al., 2011a].

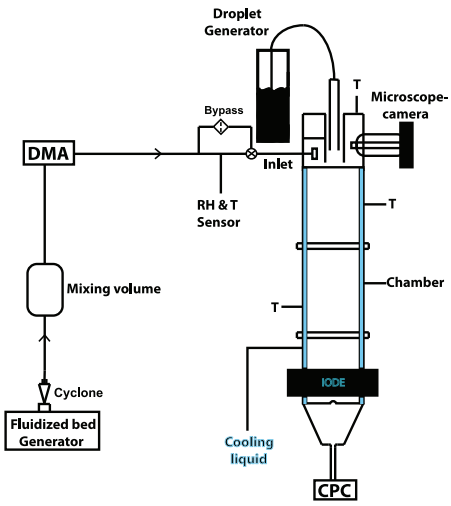

Figure 2.6: "Schematic of the experimental setup of the Collision Ice Nucleation Chamber (CLINCH) for contact freezing. Aerosol generation and size selection are shown on the left side, whereas the actual measurement and the droplet generation are shown in the right side. The interaction between particles and droplets takes place within the chamber, and the detection area is located at the bottom of the chamber. T marks the locations of the thermocouples" [Ladino et al., 2011a]

An electrodynamic balance, as used in these experiments, and for example in Svensson et al. [2009], is another method to investigate the contact freezing mode. Here, the particles collide with a freely levitated droplet, and eventually initialize freezing. This method can investigate only one droplet at a time. Svensson et al. [2009] investigated the influence of relative humidity on the contact freezing mode using kaolinite particles as INP. The authors observed a much higher on-set temperature when water vapor was inserted to the chamber. The results are shown in figure 5.23.

The challenge in wind tunnel, chamber and levitator experiments is to find out, how many particles collide with the droplet and what size the colliding particles had.

In other experiments, a cold stage with supercooled droplets on it is used to investigate contact freezing. For example Shaw et al. [2005], Durant and Shaw [2005], Bunker et al. [2012], and Niehaus et al. [2014b] put one droplet on a cold plate, and a single INP is in contact with the droplet, or an air flow containing particles streams through the droplet. After the experiment the droplets evaporate and the number of particles collected by a droplet can be counted. Durant and Shaw [2005] as well as Fornea et al. [2009] did contact freezing experiments "inside-out", which means the INP touches the droplet surface from inside out and not from outside in as in all the other methods. Durant and Shaw [2005] provide the possible explanation, that it is

only important, that the particle is in contact with the droplet surface, but it does not matter whether the particle is located outside or inside the droplet.

Bunker et al. [2012] collected size selected Arizona Test Dust and kaolinite particles on a single droplet located onto a cold plate, respectively. "The experiments show that there is a temperature, size and composition dependence to contact freezing by these two mineral dusts" [Bunker et al., 2012].

Niehaus et al. [2014b] analyzed single droplets on a temperature-controlled copper stage. The particles deposited out of an airstream. The authors observed that "ice nucleation by the bacteria Pseudomonas Syringae is found to be more efficient in the contact mode than in the immersion mode by two orders of magnitude at $-3\,°C$ with the difference diminishing by $-8\,°C$" [Niehaus et al., 2014b]. In further experiments, Niehaus et al. [2014a] compared three kinds of mineral dust and three strains of bacteria in the contact mode, and found that in "contrast to the mineral dusts, an ice-negative strain of Pseudomonas fluorescens is an order of magnitude more effective at every temperature tested". An ice-positive strain of Pseudomonas syringae is even more efficient than the ice-negative strain [Niehaus et al., 2014a].

Shaw et al. [2005] investigated volcanic ash particles, which are in contact or immersed in a single droplet on a cold plate. The authors observed that "the freezing temperature for the surface mode is approximately 4–5 K higher than that for the bulk-water mode" [Shaw et al., 2005] (figure 2.7).

Durant and Shaw [2005] analyzed evaporating droplets using the setup described in Shaw et al. [2005] and observed "that the formation of ice within a liquid water drop by heterogeneous nucleation occurs at higher temperatures if the IN is in contact with the surface of the drop, than if it is fully immersed within the bulk of the drop". The authors also found that the "higher freezing temperatures occur regardless of whether this contact is from the outside in, or the inside out, and do not depend on any transient contact between the IN and the water drop" [Durant and Shaw, 2005].

Fornea et al. [2009] investigated single particles of Mount St. Helens Volcanic Ash in contact or immersed in a droplet, and single Pahokee Peat soil and carbon lampblack particles in contact with the droplet. The authors "observed an average inside-out contact freezing temperature of $-11.2\,°C \pm 1.0\,°C$ compared to an average immersion freezing temperature of $-18.3\,°C \pm 2.0\,°C$" [Fornea et al., 2009]. The most efficient INP were the Pahokee Peat soil particles with an average contact freezing temperature of $-10.5\,°C \pm 1.8\,°C$ [Fornea et al., 2009]. The Carbon lampblack particles had an average contact freezing temperature of $-25.6\,°C \pm 3.4\,°C$ [Fornea et al., 2009].

In all cases, the comparison between contact and immersion freezing mode has shown, that contact freezing mode is ice active at higher temperatures than immersion mode for the same INP (e.g. Pitter and Pruppacher [1973], Diehl et al. [2002], Shaw et al. [2005]). The cause of this behavior has not been explained by now. One theory, based on classical nucleation theory, is given by Cooper [1974]. He proposed, that

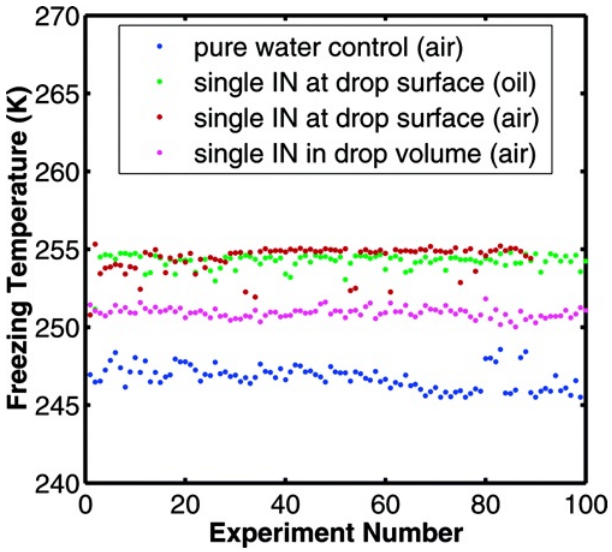

Figure 2.7: "Random freezing temperatures observed for one ice-forming nucleus in three different physical conditions. When the ice-forming nucleus is immersed in the supercooled water droplet (magenta), the mean freezing temperature is approximately 251 K. When the ice-forming nucleus is placed at the surface of the droplet the mean freezing temperature is higher, both when the supercooled droplet is surrounded by oil (green) and by air (red). A control experiment with a pure water droplet (blue) confirms that nucleation by the substrate is negligible when an ice-forming nucleus is present. Note that sudden jumps in nucleation temperature in the control experiment (e.g., at numbers 80–85) likely are due to variations in substrate properties encountered as the droplet migrates slightly throughout the set of experiments." [Shaw et al., 2005]

similar to deposition freezing mode, an ice nucleus grows on a particle from vapor phase (see figure 2.8). Since the ice-water surface energy is 4 to 5 times smaller than for an ice-vapor interface, the radius of a nucleus needed to initialize freezing in water is 4 to 5 times smaller than for vapor [Cooper, 1974]. That would explain, why the activation temperature of the contact mode is lower than for immersion mode. Fukuta [1975] suggested that the "transient high free energy condition, which is considered to appear on the nucleus surface when the air-nucleus surface is brought inside of the supercooled water as the result of the contact process, can explain the effect of contact ice nucleation". Another work of [Djikaev and Ruckenstein, 2008], compares the reversible work needed to nucleate ice at the interface of liquid water and a particle (immersion mode), and at the interface of water vapor, liquid water, and a particle (contact mode) (see figure 2.8). They found, that the formation of an ice nucleus at the triple interface is more energy efficient than at the double interface. But, as already mentioned, until now no ultimate and proven explanation exists.

A general problem with respect to the comparability of results of contact freezing

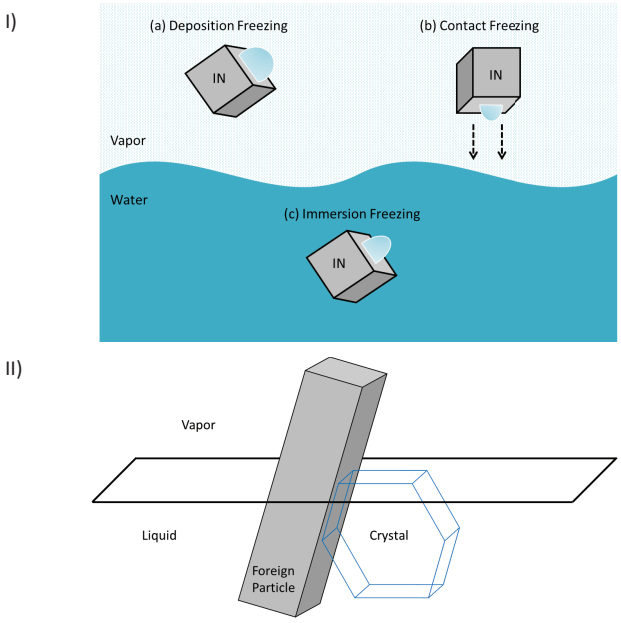

Figure 2.8: I) Illustration of heterogeneous nucleation mechanisms and the critical nucleus size; (a) deposition freezing, (b) contact freezing, (c) immersion freezing [Cooper, 1974] II) Heterogeneous formation of a crystal nucleus on a foreign particle in contact with the liquid-vapor interface [Djikaev and Ruckenstein, 2008]

experiments is that most methods give a frozen fraction or the temperature of freezing on-set, but do not quantify the number of particles colliding with the droplet during the experiments. In some methods the droplet collects hundreds of particles, and in others not even ten. It is absolutely necessary to know the collection efficiency and particle size to compare the results or to be able to implement contact freezing mode into the climate models.

From laboratory experiments, let's have a look at the field and modeling studies on the role of contact freezing in clouds.

Hobbs and Rangno [1985] postulated, that the contact freezing mode could be responsible for rapid glaciation of droplets near the cloud top. They argue, that in this region ambient air mixes into the cloud and causes the evaporation of some cloud droplets [Squires, 1958]. Then, the collision of submicron particles and evaporating droplets driven by thermophoretic forces is possible (Slinn and Hales [1971], Young [1974]). The authors estimate that if some of the aerosol particles act as contact INP and freeze a fraction of $\approx 0.1\%$ of the cloud droplets with a diameter larger than approximately 20 µm, ice multiplication can lead to complete glaciation of a cloud. Under the assumed conditions, the frozen droplets would grow by vapor diffusion, while the smaller supercooled droplets in their vicinity would quickly evaporate, or

be collected by the growing ice particles. This process would produce rapid glaciation of the top of the cloud. (Hobbs and Rangno [1985], Rangno and Hobbs [1991])

Another suggestion of Seifert et al. [2011] is that contact freezing could have been responsible for glaciation of clouds containing volcanic ash particles from the Eyjafjallajökull eruption in April 2010. Ansmann [2005] has also noted, that contact freezing was probably the main reason for ice formation on Saharan dust particles at the edges of an altocumulus in the downdraft regions. In the modeling study of Hoose et al. [2010] it was found, however, that the immersion mode is the dominating freezing mechanism, but for soot, contact freezing is also relevant. On global average, in 23% of all cases the heterogeneous nucleation could be initialized by soot.

On the other hand, Twohy et al. [2010] found, that in orographic wave clouds, condensation and immersion freezing are the probable modes for the ice formation. There are also some modeling studies (e.g., [Philips et al., 2007], they used a simplified parametrization scheme) which do not support the atmospheric relevance of contact freezing. Up to now, it is still unclear, whether or in which extent, the contact freezing mode is relevant for cloud formation, and thus, further research is necessary.

2.4 Aerosols

Atmospheric aerosol particles can act as cloud condensation nuclei (CCN) or as ice nucleating particles (INP).

For aerosol particles, there are three different ways to get into the atmosphere:

- the homogeneous condensation of gases
- the transport of particles from the Earth's surface
- from extraterrestrial sources

In this chapter, I will concentrate on particles coming from the Earth's surface. It can be discerned between continental and maritime aerosol, and between anthropogenic and natural particle sources. An overview of global aerosol concentration is shown in figure 2.9 [Warneck, 2000]. Sea salt and mineral dust are the natural aerosols with the highest mass concentration. Mineral dust is indeed a natural aerosol, but the dispersion into the atmosphere can be induced by wind or by anthropogenic activity like harvesting. Volcanic eruptions temporarily produce a massive amount of particles in the atmosphere locally, as well as forest fires, for instance.

The second-large fraction are secondary aerosols like sulfate aerosols (160 Tg/a natural, 110 Tg/a anthropogenic) and nitrate aerosols (80 Tg/a natural, 50 Tg/a anthropogenic), which are formed by chemical reactions of nitrogen, sulfur dioxide or hydrocarbons. The amount of biological particles in the atmosphere is much lower

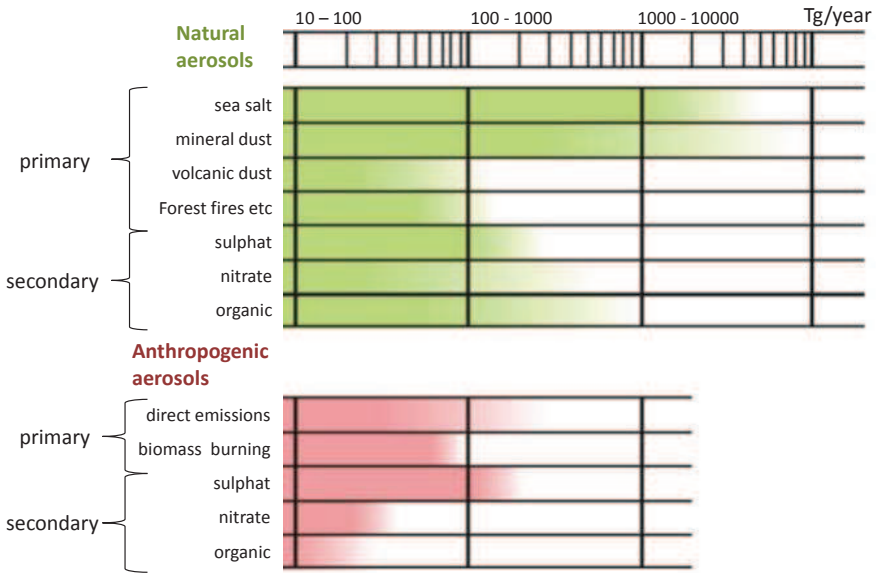

Figure 2.9: Overview of global aerosols (based on Warneck [2000])

than the amount of mineral dust, but the fact, that these particles can be ice active already at slightly subzero temperatures, makes them potentially important. Després et al. [2012] give a mass concentration of about $0.1\,\mu g m^{-3}$ for bacteria and about $0.1\,\mu g m^{-3}$ – $1\,\mu g m^{-3}$ for fungal spores as well as for plant debris (free cellulose).

The influence of the aerosol particles on the radiation budget and cloud formation depends on the location of the aerosols in the atmosphere. Tropospheric aerosols have, depending on their size, a residence time of several days on average (figure 2.10). Aerosols that reach the stratosphere, have a longer residence time in the atmosphere than tropospheric aerosols [Salby, 2012]. The longer residence time of stratospheric aerosol enables the altering of shortwave absorption at the Earth's surface for extended duration [Salby, 2012].

The focus of this work is on natural, continental aerosols like the mineral dust components hematite, kaolinite, illite and feldspar, the biological material cellulose, and a mixture of illite and birch pollen washing water (BPWW). I will compare my results with the results of pure BPWW measured by Manfred Schäfer as part of his diploma thesis [Schäfer, 2014] and Michael Koch as part of his Bachelor's thesis [Koch, 2014], and the results of measurements with SNOMAX®, also done by Schäfer [2014].

In the following, I will discuss the aerosol materials used in this work. The mineral dust components have already been investigated as INPs in several studies, but not all of them were analyzed in the contact freezing mode.

Hung et al. [2003] investigated hematite in the immersion freezing mode, and

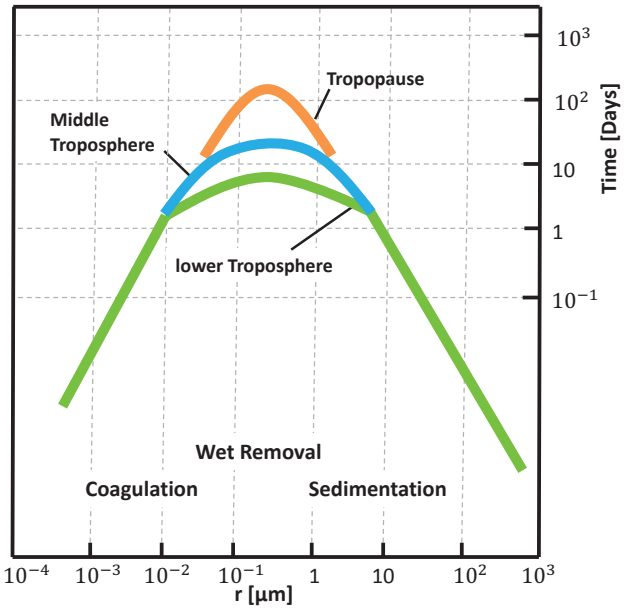

Figure 2.10: Size dependent residence time of aerosols in the atmosphere (based on [Pruppacher and Klett, 2004])

Hiranuma et al. [2014b] found that the surface roughness of hematite particles have an influence on the ice activity in a way that milled hematite was more ice active than cubic hematite in the immersion mode.

The iron oxide (hematite) (Fe_2O_3) (figure 2.12) is a component of several rock materials and often responsible for the reddish color of desert dust. Possible origins of hematite are volcanic formations, or the dehydration of iron hydroxide in hot and dry climate zones. The oxidation of upper layers of the igneous rock deposits in hot climate zones is another possible source.

The hematite particles used for the experiments in the INUIT project were synthesized at IMK-AAF by Sarah Jäger, growing pseudo cubic particles with a side length of 300 nm and 900 nm (figure 3.11a) by hydrolyzing ferric chloride ($FeCl_3$) solutions in NaOH, according to the gel-sol method Kandori et al. [2002] and Sugimoto and Sakata [1992]).

As mentioned in Atkinson et al. [2013], feldspar is a minor component of dust emitted from arid regions. The main finding of Atkinson et al. [2013] was that potassium rich (K-)feldspar is a very efficient INP in the immersion mode. Yakobi-Hancock et al. [2013] found that feldspar is also very ice active in the deposition mode.

With the amount of more than 50 volume percent of the Earth's crust, feldspar is the most frequent mineral group [Okrusch, 2014]. There are three main classes of feldspar

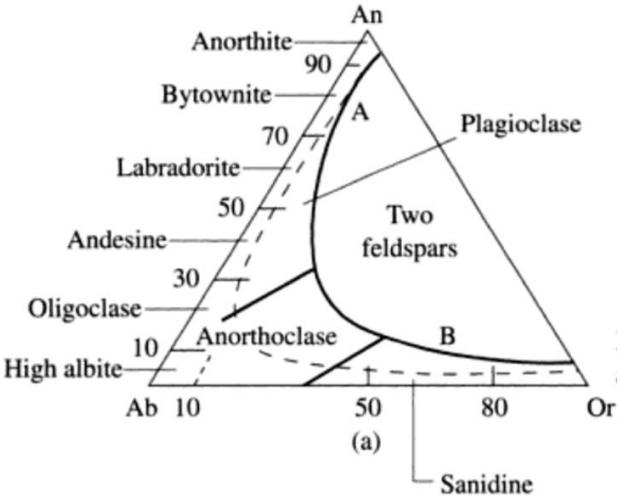

Figure 2.11: Feldspar classification, the edges of the triangle represent pure Albite, Anorthite and Orthoclase, and the numbers describe the percentage of the respective amount [Deer et al., 2001]

(potassium (K)-, sodium (Na)- and calcium (Ca)-rich), and a lot of compositions that can be illustrated on a triangle composition diagram (figure 2.11). On the triangle's edges, the major feldspar components are located. The major feldspars are the sodium feldspar $NaAlSi_3O_8$, which is called Albite (Ab), the calcium feldspar $CaAl_2Si_2O_8$ which is called Anorthite (An), and $KAlSi_3O_8$, the potassium feldspar Orthoclase (Or). The numbers show the percentage of the respective amount of major feldspar components.

Depending on the amount of K, Na and Ca and type of lattice geometry, feldspar has different names like microcline (potassium rich feldspar) or andesine (sodium rich feldspar with calcium content). Both have been investigated in this work.

The feldspars form magma and are present in many types of sedimentary and in metamorphic rocks (rocks that are forming from existing rocks in the Earth's crust due to pressure or temperature increase [Sen, 2014]). The type of feldspar depends on the chemical composition and temperature of magma [Deer et al., 2001].

Studies of Pitter and Pruppacher [1973] (contact and immersion mode), Welti et al. [2009] (deposition and condensation mode), Svensson et al. [2009] (contact mode), Lüönd et al. [2010] (immersion mode), Ladino et al. [2011a] (contact mode), and Murray et al. [2011] (immersion mode), for instance, investigated kaolinite in different heterogeneous freezing modes.

Kaolinite ($Al_2O_7Si_2 \cdot {}_2H_2O$) is a layered silicate and the major component of the rock Kaolin. The silicate layers are fixed by hydrogen bridge bonds OH-O between the OH^- ions of the octahedron and the O^{2-} ions of the tetrahedron in the adjacent

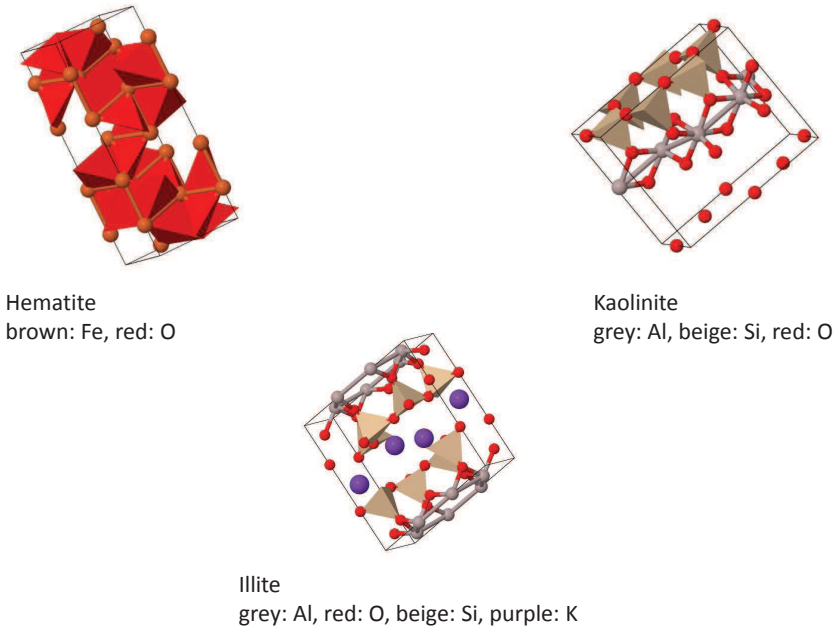

Figure 2.12: Scheme of the crystal lattice of hematite, kaolinite, and illite [Schorn et al., 2014]

silicate layer [Blume et al., 2010] (figure 2.12). In the center of the octahedron and the tetrahedron a Al^{3+} and Si^{4+} ion is located, respectively [Blume et al., 2010]. Kaolin is named after the village Kao-Ling in China, where it was discovered. Kaolinite is a widely distributed clay mineral and is formed from weathering of feldspar rich rocks like granite, rhyolite and arkose, or by reaction with thermal or hydrothermal waters (pH value < 6) [Okrusch, 2014].

Broadley et al. [2012] investigated illite in the immersion mode, and Welti et al. [2009] did measurements in the deposition and condensation mode.

Illite is a layered silicate built of one alumino-octahedron layer and two surrounding silicate-tetrahedron layers [Blume et al., 2010] (figure 2.12). A replacement of $Al_3{}^+$ by $Mg_2{}^+$ and $Fe_2{}^+$ in the octahedron is possible. It is mostly formed from muscovite and feldspar by weathering, or on a hydrothermal environment. In these experiments, the INUIT reference material illite NX nanopowder from Arginotec, composed of 69 % illite, 10 % kaolinite, 3 % quartz, 3 % calcite/carbonate and 14 % feldspar (Orthoclase/Sandinine) [Hiranuma et al., 2014a] have been used.

Pummer et al. [2012] have shown that the material washed out of birch pollen (BPWW) is as ice active as the entire pollen grain in the immersion mode. Augustin et al. [2013] have also investigated BPWW in the immersion mode. “The ice activity of the pollen washing waters could be attributed to extractable compounds with

masses between 100 and 300 kDa, which was determined via size-selective filtration" [Augustin et al., 2013]. Pummer et al. [2012] found that the ice active component of BPWW are macromolecules with no or irrelevant proteinaceous content.

As mentioned in Möhler et al. [2007], it is more likely that biological material is located on mineral dust particles, than that mineral dusts and biological material coexist isolated in the atmosphere. As a model substance possibly relevant for ice formation in the atmosphere, mixture of a mineral dust with BPWW have been investigated.

As a component of plants, cellulose particles (Sigma Aldrich, Cellulose microcrystalline, powder) (figure 3.11f) were investigated as INP in the contact mode. For example Sánchez-Ochoa et al. [2007] found "free cellulose" concentrations in the range of 16.3 ng/m^3 at the ocean background site (Azores) to 181 ng/m^3 at a mid-European background site (K-Puszta, Hungary). Puxbaum and Tenze-Kunit [2003] have found that aerosol particles in a size range of 0.1 µm to 1.6 µm aerodynamic diameter, contained 0.7% "free cellulose".

"Cellulose microfibrils are insoluble cable-like structures that are typically composed of approximately 36 hydrogen-bonded chains containing 500 to 14,000 β-1,4-linked glucose molecules. Cellulose microfibrils comprise the core component of the cell walls that surround each cell. Roughly one-third of the total mass of many plants is cellulose." [Somerville, 2006]

Figure 2.13 [Metzler, 2014] shows the schematic construction of the cell wall and the microfibril structure as well as the cellulose molecules. A single microfiber is built of an inner bundle of microcrystalline cellulose, surrounded by paracrystalline cellulose and an outer layer of hemicellulose, which connects the single microfibers.

Hiranuma et al. [2015] found that cellulose is a good INP in the immersion mode.

Bacteria are very active INPs (e.g., Wolber et al. [1986], Wolber and Warren [1989], Morris et al. [2004], Möhler et al. [2008], Hartmann et al. [2013], Wex et al. [2015]).

The reason for their ice nucleation efficiency is the presence of a protein complex (e.g. Orser et al. [1985]). Garnham et al. [2011] estimated the surface area of an ice nucleation active (INA) protein as 4 nm by 32 nm. As a proxy for ice nucleating bacteria, we chose SNOMAX®, which is a commercial product containing fermented, pelletized, freeze-dried and irradiated Pseudomonas Syringae bacteria produced by the company Johnson Controls Snow, Colorado, USA to perform experiments in the contact freezing mode. The experiments were done by Manfred Schäfer [Schäfer, 2014].

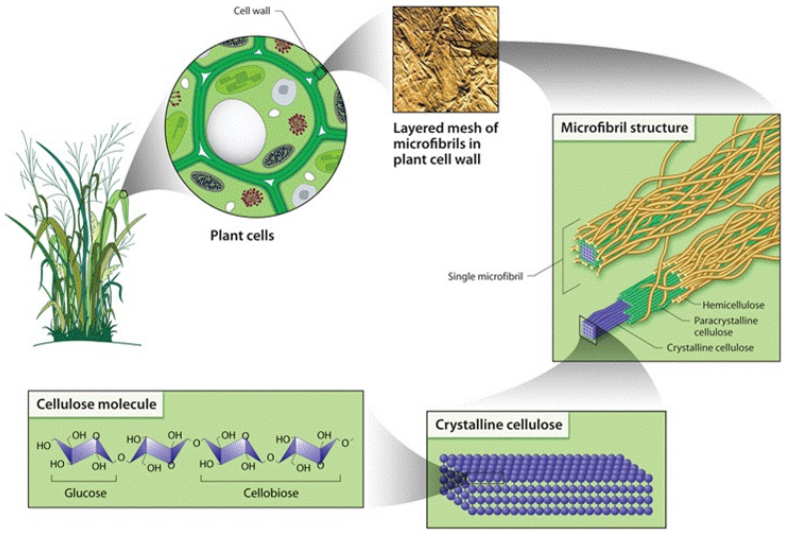

Figure 2.13: Structure of cellulose in plant cells [Metzler, 2014]

3 Experimental details

Most parts of the experimental setup have already been described in the doctoral thesis of Daniel Rzesanke [Rzesanke, 2012], my diploma thesis [Hoffmann, 2012], and the method paper Hoffmann et al. [2013a]. Here I will briefly describe the electrodynamic balance (EDB) and the experimental setup. In the following, the performing of a contact and an immersion freezing experiment, and the verification of the collection efficiency are explained, as well as some details on the aerosol characterization.

3.1 Electrodynamic balance

The centerpiece of this experiment is an electrodynamic balance (EDB), also called "Paul-trap", after the German physicist Wolfang Paul, who received the Nobel price for this invention in 1989. A EDB allows the levitation of charged particles. In this experiment EDB was used to levitate charged droplets of deionized water with a diameter of either 90 µm or 60 µm.

The principle of operation of an electrodynamic balance is described in detail in Davis and Schweiger [2002], and, especially concerning the used experimental setup in the doctoral thesis of Dr. Denis Duft [Duft, 2010] and Dr. Daniel Rzesanke [Rzesanke, 2012]. In the following, the functionality is described briefly.

To levitate a charged particle, a force balance between the gravitation and the drag force of the flow (both act in the vertical direction in this experimental setup), and the particle has to maintained. The gravity and the drag force can be compensated with a capacitor. The force of the electrical field $F_e = qE = q(U/d)$ (q: charge, U: voltage, d distance between the electrodes) must be equal to the weight force of the particle $F_g = mg$ (m: mass of the droplet, g: acceleration of gravity). In this experiment the aerosol flow is passing through the EDB from below, so that the force of the electric field must push the droplet back into the center of the EDB. With the drag force $F_D = 6\pi\eta rv$ (r: droplet radius, η: dynamic viscosity of gas, v: velocity of the gas flow), the balance of forces is described by:

$$F_D - F_e - F_g = 0 \tag{3.1}$$

Let us consider the conditions for lateral stability of a charged particle in the EDB. Let $P_0(x_0, y_0, z_0)$ be the point, where the charged droplet is suspended. To do so, the

forces on $P(0)$ have to be compensated. The electrical field should exert a restoring force on the droplet, and accordingly have a minimum in $P(0)$. Thus a potential $\Phi(x_0, y_0, z_0)$ must satisfy the following relations:

$$\nabla\Phi(x_0, y_0, z_0) = 0 \qquad \text{and} \tag{3.2}$$

$$\Delta\Phi(x_0, y_0, z_0) > 0 \tag{3.3}$$

A further requirement is that the location of the droplet is a charge-free space, so the potential in point P_0 must satisfy the Laplace equation $\Delta\Phi(x_0, y_0, z_0) = 0$. This excludes an electrostatic potential. The remaining solution is a electrodynamic field, which has a sufficiently high frequency to hold the charged droplet stably in $P(0)$ because of its inertia. The droplet will notice only the force of the time-averaged field. The potential to this force is called pseudo-potential Φ_{pseudo}. This kind of electrical field is of the type $E(z,t) = E_0(z)\cos(\omega t)$.

The motion of a droplet with the mass m and charge q in this field is described by the following components:

$$z(t) = \bar{z}(t) + \xi(t) \tag{3.4}$$

$\bar{z}(t)$ is the motion of the droplet, and the time-average over a period $\frac{2\pi}{\omega}$ is given by:

$$\bar{z}(t) = \frac{\omega}{2\pi} \int_{t}^{t+\frac{2\pi}{\omega}} z(\tau)d\tau \tag{3.5}$$

compared to $\bar{z}(t)$, the part of $\xi(t) = \xi_0\cos(\omega t)$, which gives the amplitude of the oscillation of the droplet in the alternating field is comparatively small.

The resulting equation of motion of the droplet in the field $E(z,t)$ is given by:

$$m\ddot{z} = qE(z,t) = qE_0(z)\cos(\omega t) \tag{3.6}$$

From the series expansion

$$m\ddot{z} = m\ddot{\bar{z}} + m\ddot{\xi} = qE(\bar{z},t) + q\xi\frac{\partial E(\bar{z},t)}{\partial\bar{z}} \tag{3.7}$$

results for small amplitudes $\xi(t)$:

$$m\ddot{\xi} = qE(\bar{z},t) \tag{3.8}$$

The oscillation is directly proportional to the strength of the electric field. Integrating the field in equation (3.6) twice yields:

$$\xi(t) = -\frac{q}{m\omega^2}E_0(\bar{z})\cos(\omega t) \tag{3.9}$$

Now it is possible to calculate the time-averaged force acting on the droplet from equation (3.7):

$$\overline{m\ddot{\bar{z}}} = \overline{qE(\bar{z},t)} + \overline{q\xi\frac{\partial E(\bar{z},t)}{\partial \bar{z}}} \tag{3.10}$$

$\overline{qE(\bar{z}(t))}$ describes the average force, which is following from the fast oscillation, so that this part is zero. This yields:

$$\overline{m\ddot{\bar{z}}} = q\frac{\partial E_0(\bar{z})}{\partial \bar{z}}\xi_0\overline{\cos^2(\omega t)} \tag{3.11}$$

With $\overline{\cos^2(\omega t)} = \frac{1}{2}$, the time-average force acting on the droplet in the alternating field can be written as:

$$\bar{F}(\bar{z}) = \frac{1}{2}\frac{q^2}{m\omega^2}E_0(\bar{z})\frac{\partial E_0(\bar{z})}{\partial \bar{z}} \tag{3.12}$$

Since the force depends quadratically on the charge, the polarity of the droplet does not matter. Furthermore, the negative sign in the equation shows that the force is acting always in the direction of the decreasing field strength. With the pseudo potential Φ_{pseudo}, the average force is:

$$\bar{F}(\bar{z}) = -q \cdot \nabla\Phi_{\text{pseudo}}(\bar{z}) \tag{3.13}$$

with $\Phi_{\text{pseudo}}(\bar{z}) = \frac{q}{4m\omega^2}E_0^2(\bar{z})$.

The droplet can be hold stably in the minimum if the pseudo potential satisfies the properties described at the beginning of this section (eq. 3.2 and 3.3).

For example, a quadrupole field has the described properties and the potential is given as:

$$\Phi = \Phi_0(\alpha x^2 + \beta y^2 + \gamma z^2) \tag{3.14}$$

Furthermore, the potential of the quadrupole field must satisfy the Laplace equation $\Delta\Phi = 0$. Therefor:

$$2\Phi_0(\alpha + \beta + \gamma) = 0 \tag{3.15}$$

and since $\Phi_0 \neq 0$, $\alpha + \beta + \gamma$ must be zero.

One solution is $\beta = \alpha$ and $\gamma = -2\alpha$. This implies the potential

$$\Phi = \Phi_0 \cdot \alpha(x^2 + y^2 - 2z^2). \tag{3.16}$$

A conversion into cylindrical coordinates with $r^2 = x^2 + y^2$ and $\alpha = \frac{1}{r_0^2}$ simplifies the equation of the potential to:

$$\Phi = \frac{\Phi_0}{r_0^2}(r^2 - 2z^2) \tag{3.17}$$

This potential describes the equipotential surfaces of a rotation symmetric object, made of three hyperbolic parts. The axial ratio is given by $r_0 = \sqrt{2}z_0$.

3.2 Experimental setup

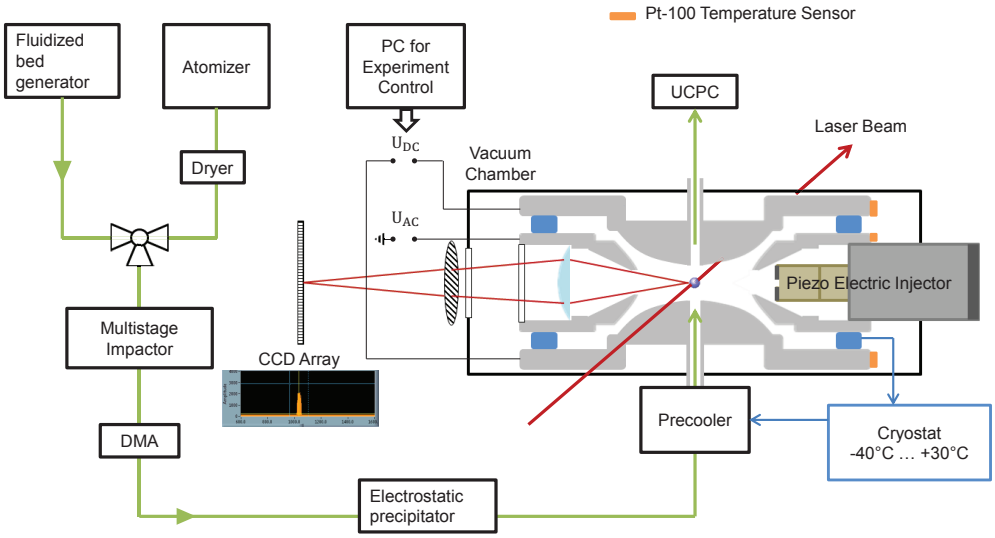

Figure 3.1: Schematic sketch of the experimental setup

Figure 3.1 shows a schematic sketch of the entire experimental setup. The green arrow shows the aerosol path through the different components of the setup. The generation, size selection, and counting is described more in detail in section 3.6. The EDB described in section 3.1 is located in a vacuum chamber for electrical and thermal isolation. A profile of the vacuum chamber and the electrodes of the EDB inside the vacuum chamber are shown on the right hand side in 3.1. The chamber is evacuated using a membrane pump and a turbo pump (MVP 015 and TMH 071P, Pfeiffer Vacuum). The electrostatic precipitator is needed to perform immersion freezing experiments, to sample TEM grids, or to do experiments to verify the collision rate. It consists of a metal tube and an inner electrode with a high voltage supply. The electrostatic field accelerates the incoming, mobility selected particles to the inner electrode, so that the entering flow is particle-free. Furthermore, the inner electrode is magnetic so that TEM grids can be installed to sample the particles and analyze them under an electron scanning microscope.

Figure 3.2 shows the external vacuum chamber [9] with the periphery devices. [10] shows the connection to the vacuum pump. The optical access to the internal part of the EDB is provided through five ports covered with glass windows or lenses. One port in the vacuum chamber is connected to the center electrode by a vacuum-tight tube [7]. This allows us to put a piezo electric injector close to the center of the EDB and inject droplets of deionized water (NANOpurer® Infinity Base Unit, Barnstead-Thermolyne Corporation). The laser light (HeNe laser, model 1136P, JDS Uniphase Corporation, wave length $\lambda = 632.8\,\text{nm}$) [1] is polarized vertically and directed to the

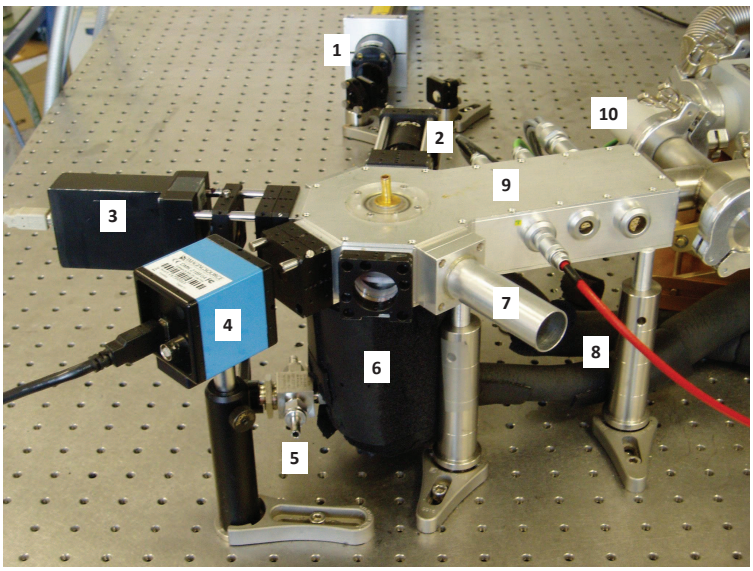

Figure 3.2: View of the external vacuum chamber and the periphery devices (numbered components are described in text)

center of the EDB by a system of mirrors [2]. To observe the light scattered by the levitated droplet, a CCD-array (Spectronics Devices) [3] and a camera (model DMK 21BF04, ImagingSource) [4] are used. The camera detects the intensity distribution of the scattered light of the droplet within the scattering angle of (45±9.4)°, which enables us to calculate the droplet diameter by using the theory of Mie [Bohren and Huffman, 1983]. The CCD linear array is used to detect the droplet's vertical position inside the EDB and the freezing initiation. Before the very first experiment, it is necessary to find the geometrical center of the EDB; that means the position where the droplet is levitated stably. When this position is found, the scattered light reaches a certain area of the CCD array. A LabView program reads the signal of the CCD array and the center position can be marked. Since the droplet evaporates slightly during its time in the EDB, the DC voltage must be re-adjusted constantly. The so-called height control is a unit which reads the scattered light position on the CCD array and changes the DC voltage accordingly, so that the scattered light always hits the CCD array in a pre-defined center position. A polarization filter is located in front of the CCD array and decreases the signal. If the droplet freezes, the polarization state of the scattered light is changed and the signal of the CCD array increases. By setting an intensity threshold, the freezing can be detected.

The aerosol flow (inlet: [5]) is cooled down to EDB temperature in the precooler [6]. A cryostat (Julabo FP 50, model HE) pumps the cooling liquid in the precooler first [8]. A Pt-100 temperature sensor is located on each electrode (figure 3.1). A temperature monitor (model 218, LakeShore) reads out the sensors. The temperature in the EDB's center is measured and verified that the temperature sensor on the bottom electrode yields the temperature of the EDB center within 0.08 °C accuracy.

3.3 Gas velocity in the EDB

To calculate the collision rate, the velocity of the aerosol flow through the EDB has to be known. Two cylindrical tubes at the bottom and top electrode ensured laminar flow conditions. The flow was simulated at a temperature of 20 °C [Duft, 2012]. The velocity profile is shown in figure 3.3. In the center, the flow velocity reached a maximum of 0.575 m/s at a flow rate ω of 300 ml/min.

Since the EDB was cooled down to subzero temperatures, the velocity changed because of the compressibility of the gas. Using the ideal gas law and the isobaric condition of the system, the velocity has to be corrected by:

$$\omega = \frac{V_0}{t} \tag{3.18}$$

$$\frac{V_0}{T_0} = \frac{V}{T} \tag{3.19}$$

$$\Rightarrow \quad V = V_0 \frac{T}{T_0} \tag{3.20}$$

$$\Rightarrow \quad \omega = \frac{V}{t} = \frac{V_0}{t}\frac{T}{T_0} \tag{3.21}$$

with the temperature $T_0 = 20\,°\mathrm{C}$ and volume V_0, which is the gas volume at 20 °C. T is the temperature of the current experiment and volume V, the gas volume at this temperature.

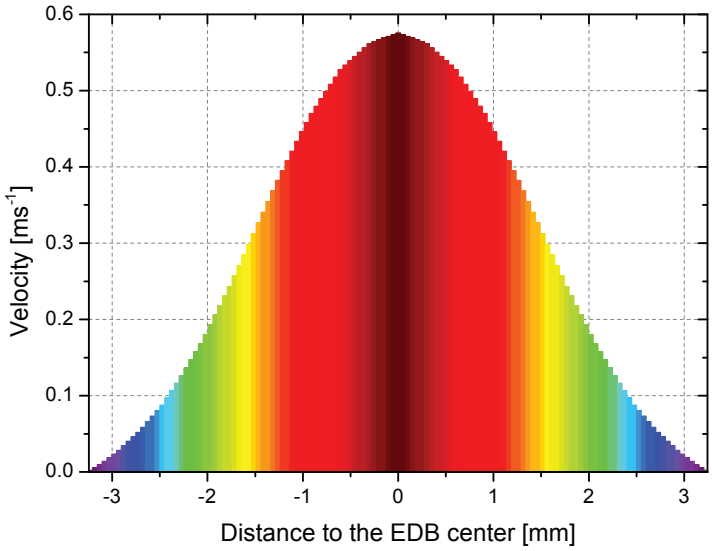

Figure 3.3: Velocity profile of the aerosol flow through the EDB

3.4 Droplet generation and calculation of droplet size

The droplets were produced by a piezo electric injector (GeSIM model SPIP: A010-006, or GeSIM model PicPIP: A010-206, with cylindrical housing respectively)(figure 3.4). By applying a pulse (SPIP: amplitude: 60 V to 65 V, length: 100 ms to 110 ms, and PicPIP: amplitude: 48 V to 60 V, length: 45 ms to 55 ms) to the piezo crystal, the water reservoir attached to it became deformed, and a single water droplet with a diameter of about 90 µm for SPIP and about 60 µm for PicPIP was ejected out of the tip. Since the injector is located in one of the EDB ports, and the EDB is cooled down to temperatures between −9 °C and −34 °C, the water reservoir has to be heated up to about 30 °C by a Pt-100 element. The droplet passes through an electrode, where a voltage of about 500 V is applied and reaches the EDB center. The droplets get charged by passing through the electrode due to electrostatic induction. A single droplet is carrying a charge of about 0.6 pC to 1.5 pC , depending on the droplet diameter and the temperature of the EDB and heating element on top of the water reservoir. For each experiment, the parameters are constant. The droplet diameter is monitored by taking a picture of the droplet's scattering pattern at injection and ejection for at least every 10th droplet.

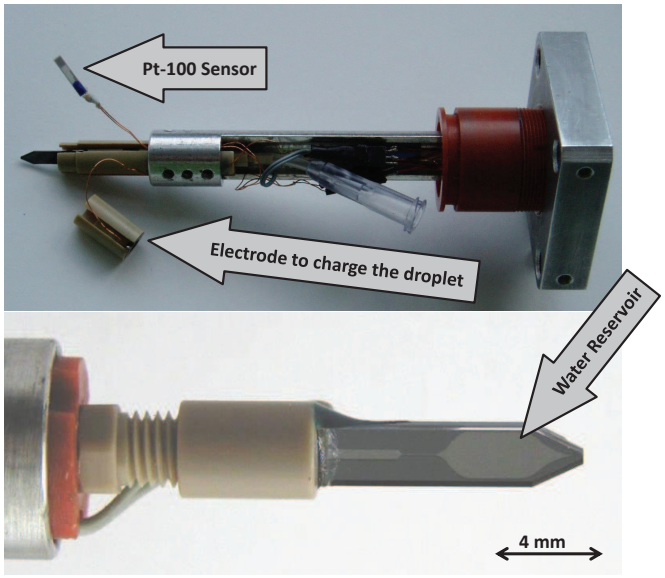

Figure 3.4: Piezo Electric Injector mounted in a holder to install it airtight into the injector port of the EDB housing

The Mie theory of light scattering by spherical particles from 1908, named after the German physicist Gustav Mie, is used to calculate the droplet diameter from the intensity distribution of the scattered laser light. The Mie theory gives a numerical solution of the Maxwell equations for scattered electromagnetic waves on spherical

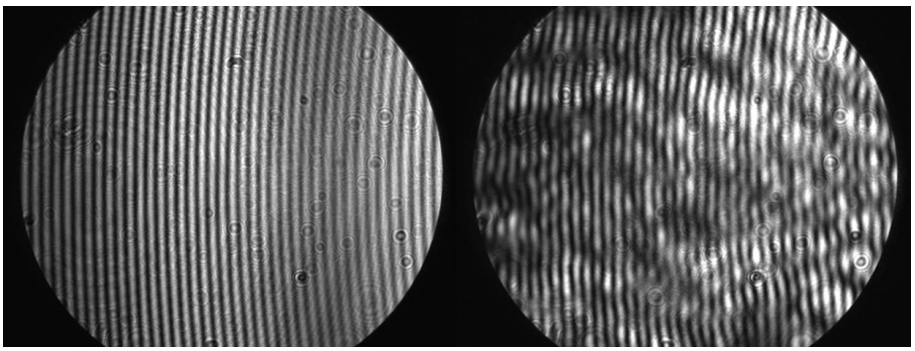

Figure 3.5: Scattering pattern of a liquid droplet (left panel) and a frozen droplet (right panel)

objects of any size. Detailed mathematical derivations are given in Bohren and Huffman [1983] or Davis and Schweiger [2002], for example.

In this experiment the far-field of the scattered light is observed by a camera (model DMK 21BF04, ImagingSource). The observation angle is defined by the aperture installed inside the port located at 45 °. The observation angle is 18.76 °, calculated from the geometry of the EDB port. To calculate the diameter, it is necessary to know the refraction index in, and around the spherical object. Both refraction indices are constant during each experiment. The value of the size parameter $x = \frac{2\pi r}{\lambda} \approx 450$ (r: droplet radius, λ: wave length) shows that the Mie theory should be used to evaluate the diameter of the droplet. For example, in the limiting case $x < 1$ the Mie-theory can be approximated by the Rayleigh scattering, or for $x \gg 10$ (for example $x > 1000$), the geometrical optic can be used.

The method of size determination applied to levitated particles or droplets was described for example in Taflin et al. [1988] or Steiner et al. [1999]. The striped pattern shown in figure 3.5 is the intensity distribution of the scattered light. The horizontal cross section of the 2D scattering pattern yields scattering phase functions. The size of the droplet can be calculated by comparing the observed phase function with the one calculated with Mie theory, for given scattering geometry and using the size parameter as free fitting parameters. The crystalline fractures in the frozen droplet scatter the laser light in all directions immediately and the calculation via Mie-striped-pattern becomes unreliable.

3.5 A relationship between the droplet temperature and humidity in the EDB

The droplet injector is located in the port of the center electrode of the EDB (see figure 3.1 [7]). The droplets are injected into the much colder environment of the

EDB center. The time, required for the droplet to cool down to the temperature of the center of EDB has to be considered in the evaluation of the freezing experiments. In the following calculation, the time between the droplets leaving the injector and reaching the EDB center is neglected, even if in this short time of about 1 ms the droplet will already start to cool down.

The cooling of a droplet is described following Baehr and Stephan [2013]:

Assuming that the density ρ of the droplet is constant, and the thermal conductivity λ and heat capacity c_p show no temperature dependency, the heat equation simplifies to:

$$\frac{\partial \theta}{\partial t} = a\nabla^2\theta + \frac{\dot{W}}{c_p\rho} \tag{3.22}$$

The constant $a = \frac{\lambda}{c_p\rho}$ describes the thermal diffusivity. Since we have no heat source, the heat equation can be written in spherical coordinate system as:

$$\frac{\partial \theta}{\partial t} = a\frac{\partial^2\theta}{\partial x^2} \tag{3.23}$$

The time depended temperature radial distribution $\theta = \theta(r,t)$ of a sphere with one dimensional thermal flow is described as:

$$\frac{\partial \theta}{\partial t} = a\left(\frac{\partial^2\theta}{\partial r^2} + \frac{2}{r}\frac{\partial\theta}{\partial r}\right) \tag{3.24}$$

The sphere has the temperature θ_0 at time $t = 0$. θ_e is the temperature of the environment.

To simplify the equation, we introduce a dimensionless parameter $r^+ := r/r_{1/2}$ with $r_{1/2}$ the half radius, $t^+ := at/r_{1/2}^2$ and $\theta^+ := \frac{\theta-\theta_e}{\theta_0-\theta e}$. Now equation 3.24 can be written as:

$$\frac{\partial \theta^+}{\partial t^+} = \frac{\partial^2\theta^+}{\partial {r^+}^2}\frac{2}{r^+}\frac{\partial\theta^+}{\partial r^+} \tag{3.25}$$

The boundary conditions are $\frac{\partial\theta^+}{\partial r^+} = 0$ for $r^+ = 0$ and $-\frac{\partial\theta^+}{\partial r^+} = \mathrm{Bi}\theta^+$ for $r^+ = 1$, with the Biot number $\mathrm{Bi} = \alpha r_{1/2}/\lambda_{\mathrm{sphere}}$ (α: heat transfer coefficient, ratio of the required amount of heat and the temperature difference between surface and environment).

The dimensionless temperature distribution for a sphere has the form:

$$\theta^+ = f_2(r^+, t^+, \mathrm{Bi}) \tag{3.26}$$

For $\theta_e < \theta_0$, which describes a cooling process (see figure 3.6), it follows from equation 3.25:

$$\theta(x,t) = \theta_e + (\theta_0 - \theta_e)\theta^+(r^+, t^+) \tag{3.27}$$

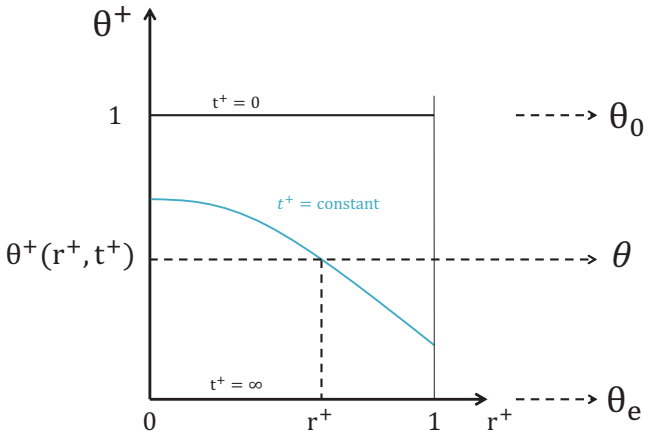

Figure 3.6: temperature relationship $\theta^+ = (\theta - \theta_e)/(\theta_0 - \theta_e)$ at the cooling process, adapted from Baehr and Stephan [2013]

The partial differential equation 3.25, can be solved by separating the variables $\theta^+(r^+, t^+) = F(r^+) \cdot G(t^+)$. Solving the differential equation, the temperature distribution inside the sphere can be found by:

$$\theta^+(r^+, t^+) = \sum_{i=1}^{\infty} c_i \frac{\sin(\mu_i r^+)}{\mu_i r^+} \exp(-\mu_i^2 t^+) \tag{3.28}$$

μ_i are the eigenvalues of the differential equation resulting from the separation of variables, and the eigenvalues are the solutions of the transcendental equation: $\mu \cdot \cot \mu = 1 - Bi$. The coefficient c_i is given by

$$c_i = 2 \frac{\sin \mu_i - \mu_i \cos \mu_i}{\mu_i - \sin \mu_i \cdot \cos \mu_i} \tag{3.29}$$

Since the thermal conductivity of water is high in contrast to the surrounding air, the temperature inside the droplet T_d can be assumed to be the same everywhere. The heat flow $\dot{Q}$ is given by:

$$\dot{Q} = \alpha A \Delta T \tag{3.30}$$

A gives the surface area (for a spherical droplet: $A = \pi d^2$), and ΔT is the temperature difference between the environment and the droplet. The heat transfer coefficient α depends on the thermal conductivity of the environment (air) and the flow conditions. In the experimental setup, the droplet is suspended in a flow coming from below.

The heat exchange with the gas flow depends on the flow regime (convective or conductive). This can be described by the Nusselt number $\mathrm{Nu} = \frac{\alpha \cdot d}{\lambda_e}$. For a single

Table 3.1: Material properties used for the calculation of the droplet cooling

temp. [°C]	matter	density ρ [kg m^{-3}]	kin. viscosity ν [m^2 s^{-1}]	thermal conductivity λ [W K^{-1}m^{-1}]	Pr
-20	Air	1.377	117.7E-7	2.28E-2	0.7143
-40	Air	1.496	101.3E-7	2.12E-2	0.7181
+30	Water	995.65	0.801E-6		
+40	Water	992.22	0.658E-6		

sphere in a flow, Whitaker [1972] gives the following Nusselt number:

$$(Nu - 2) = \left(0.4\,\mathrm{Re}^{1/2} + 0.06\,\mathrm{Re}^{2/3}\right)\mathrm{Pr}^{0.4}\left(\frac{\mu_e}{\mu_0}\right)^{1/4} \tag{3.31}$$

with the Reynolds number Re, the Prandtl number Pr and the ratio of the viscosity of environment and sphere μ_e/μ_0. The Reynolds number is an indicator whether a flow is laminar or turbulent. For a flow in a tube, the Reynolds number can be calculated by $\mathrm{Re} = \frac{v \cdot d_i}{\nu_{\mathrm{air}}}$ with the flow velocity v, the inner diameter of the tube d_i, and ν_{air} the kinetic viscosity of the environment. A $\mathrm{Re} < 2000$ corresponds to a laminar flow condition, and $\mathrm{Re} > 4000$ to a turbulent flow. It can be readily shown, that the flow in the EDB is laminar. For $-20\,°\mathrm{C}$ and $-40\,°\mathrm{C}$:

$$\mathrm{Re}(-20\,°\mathrm{C}) = \frac{0.4965\,\mathrm{m/s} \cdot 0.0044\,\mathrm{m}}{1.18 \cdot 10^{-5}\,\mathrm{m^2/s}} = 186 \tag{3.32}$$

$$\mathrm{Re}(-40\,°\mathrm{C}) = \frac{0.4573\,\mathrm{m/s} \cdot 0.0044\,\mathrm{m}}{1.01 \cdot 10^{-5}\,\mathrm{m^2/s}} = 199 \tag{3.33}$$

The material properties used in this and the following calculations are from Baehr and Stephan [2013] (see table 3.1)

The Prandtl number defines the ratio of the kinetic viscosity ν to the thermal diffusivity a. The following experimental conditions have been calculated:

- Scenario 1: injection temperature droplet: $40\,°\mathrm{C}$, EDB temperature $-40\,°\mathrm{C}$:
  $\mathrm{Nu} = 4.49\,\mathrm{W/(Km)} \Rightarrow \alpha = 2118\,\mathrm{W/(Km)}$
- Scenario 2: injection temperature droplet: $30\,°\mathrm{C}$, EDB temperature $-40\,°\mathrm{C}$:
  $\mathrm{Nu} = 4.62\,\mathrm{W/(Km)} \Rightarrow \alpha = 2179\,\mathrm{W/(Km)}$
- Scenario 3: injection temperature droplet: $40\,°\mathrm{C}$, EDB temperature $-20\,°\mathrm{C}$:
  $\mathrm{Nu} = 4.45\,\mathrm{W/(Km)} \Rightarrow \alpha = 2255\,\mathrm{W/(Km)}$

Analogous to the Nusselt number, the Biot number Bi gives the ratio of heat transfer resistance inside of the sphere (here the droplet) and its surface. The value of Bi

determines whether the temperature field inside the droplet varies in space. For small Biot number, the temperature variability inside the droplet is small. For the calculated conditions, Bi is between 0.08 and 0.09. Assuming that the density ρ_{sphere} and the heat capacity c_p is constant with temperature, it yields:

$$\frac{dU}{dt} = \dot{Q} = V\rho_{\text{sphere}}c_p\frac{d\theta}{dt} \tag{3.34}$$

$\dot{Q} = \alpha A\Delta T$, follows the differential equation:

$$\frac{d\theta}{dt} = \frac{\alpha \cdot A}{c_p\rho V} \tag{3.35}$$

For $\theta(t=0) = \theta_0$, the differential equation 3.35 has the following solution:

$$\theta^+ = \frac{\theta - \theta_e}{\theta_0 - \theta e} = \exp\left(-\frac{\alpha A}{c_p\rho V}t\right) \tag{3.36}$$

Now the heat transfer coefficient, the material constants, and the geometry of the body are combined in the characteristic cooling time $t_c = \frac{c_p\rho V}{\alpha A}$.

The time a droplet with an injection temperature of 30 °C and 40 °C, would need to cool down to a EDB temperature of −20 °C and −40 °C, are shown in figure 3.7. It is easy to see, that during 0.2 s the droplet reach the EDB temperature, independent – within the usual experimental conditions – of the injection temperature and the EDB temperature. For comparison, the broken lines in figure 3.7 show the cooling of the droplet only due to natural convection. This case is described in the doctoral thesis of Peter Stöckel [Stöckel, 2001].

We saw that the droplet reaches the center point temperature of EDB in about 0.2 s. Furthermore, the EDB software needs about 0.5 s to recognize the levitated droplet. To exclude the droplets frozen before trapping, we neglected the droplets frozen during the first second of the experiment.

Since the freezing probability has a steep temperature dependency, the temperature on the droplet surface is important to know, and will be discussed in the following.

To prevent ice growth in the precooler and on the electrodes, the dew and frost point temperature of the gas flow has to be lower than the temperature of the coldest electrode. This also means that the droplet evaporates during its residence time (30 s at most) in the EDB. The following description of the droplet evaporation in a EDB follows discussions given in Stöckel [2001].

If the evaporating droplet is colder than the environment, the heat flow $\dot{Q}$ is directed towards the droplet. The energy balance can be described by:

$$-nc_p\dot{T}_d + \dot{Q} = -\Delta h_e\dot{n} \tag{3.37}$$

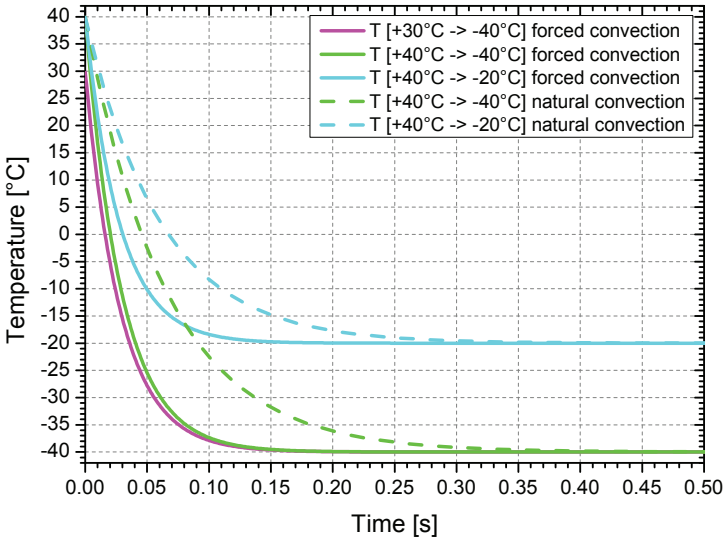

Figure 3.7: Cooling of a droplet (d = 90 µm) injected into the cold environment of the EDB. Red, green and blue line for a droplet injected into the EDB with the flow of 300 ml/min, broken lines: only natural convection

n is the amount of substance, Δh_e is the molar enthalpy of evaporation and T_d is the inner droplet temperature.

As we saw above, the temperature inside the droplet can be assumed the same in every point of the droplet volume. After about 0.2 s the droplet reaches the temperature of the EDB, and the droplet temperature stays constant, so $\dot{T} = 0$. In a steady state $\dot{Q}$ is given by (e.g. Pruppacher and Klett [2004], Rogers and Yau [1996]):

$$\dot{Q} = 4\pi r_{\text{inject}} \lambda_{\text{air}} \Delta T \tag{3.38}$$

Taking in account, that the mean free path of the gas molecules (m.f.p $\approx$ 66 nm) is a thousand times smaller than the droplet radius r (so the Knudsen number Kn =mean free path of surrounding gas/ radius droplet $\ll 1$), which corresponds to the continuum-regime [Shaw and Lamb, 1999], and the neglection of convection [Pruppacher and Klett, 2004], and a small temperature differences between droplet and its environment, the time-depended change of the droplet radius r in a steady state ($\dot{T} = 0$) is given by:

$$\dot{r} = -\chi \cdot r \tag{3.39}$$

where χ is the evaporation rate, which can be measured in the experiment, and r describes the droplet radius.

The integration of eq. 3.39 gives the decrease of droplet radius with time [Rogers and Yau, 1996]:

$$r(t)^2 = r_0^2 - 2\chi t \tag{3.40}$$

To measure the reduction of size during the residence time, a picture is taken of at least every 10th droplet at injection and ejection. By integration of eq. 3.39, the evaporation rate can be calculated from two measurable quantities, the injection radius r_{inject} and the ejection radius r_{eject} of the droplet:

$$\chi = \frac{r_{\text{inject}}^2 - r_{\text{eject}}^2}{2 \cdot t} \tag{3.41}$$

The volume reduction during the residence time is given by:

$$\dot{V} = 4\pi r_{\text{inject}}^2 \dot{r} \tag{3.42}$$

The change of the amount of water in a spherical droplet is given by:

$$\dot{n} = \frac{\rho_w}{M_w}\dot{V} = \frac{\rho_w}{M_w} 4\pi r_{\text{inject}}^2 \dot{r} = -\frac{\rho_w}{M_w} 4\pi r_{\text{inject}} \chi \tag{3.43}$$

with ρ_w the density of water.

To calculate the temperature differences between trap and droplet surface, insert eq. 3.43 into eq. 3.37:

$$\Delta T = -\frac{\rho_w \Delta h_e \chi}{\lambda_{\text{air}} M_w} \tag{3.44}$$

The following parametrization have been used in the calculations of ΔT:

- Calculation of the density of water [Hare and Sorensen, 1987]:

  $$\rho_w = a_0 + a_1 T + a2T^2 + a_3 T^3 + a_4 T^4 + a_5 T^5 + a_6 T^6 \ \ [\text{kg/m}^3], \tag{3.45}$$

  (with $a_0 = 0.99986$, $a_1 = 6.69 \cdot 10^{-5}$, $a_2 = -8.486 \cdot 10^{-6}$, $a_3 = 1.518 \cdot 10^{-7}$, $a_4 = -6.9484 \cdot 10^{-9}$, $a_5 = -3.6449 \cdot 10^{-10}$, $a_6 = -7.497 \cdot 10^{-12}$)

- Calculation of the molar enthalpy of evaporation [Pruppacher and Klett, 2004] ($-44\,^\circ\text{C} \leq T \leq -20\,^\circ\text{C}$):

  $$\Delta h_e = b_0 + b_1 T + b_2 T^2 + b_3 T^3 + b_4 T^4 + b_5 T^5 \ \ [\text{J/mol}], \tag{3.46}$$

  (with $b_0 = 45.054$, $b_1 = -0.04336$, $b_2 = 6.97903 \cdot 10^{-5}$, $b_3 = -2.02811 \cdot 10^{-6}$, $b_4 = 2.34709 \cdot 10^{-8}$, $b_5 = -1.12869 \cdot 10^{-10}$)

- Calculation of the thermal conductivity [Vargaftik, 1983]:

  $$\lambda_w = c_0 + c_1 \cdot T + c_2 \cdot T^2 \ \ [\text{W/(Km)}] \tag{3.47}$$

  (with $c_0 = -4.6654 \cdot 10^{-4}$, $c_1 = 9.8521 \cdot 10^{-5}$, $c_2 = -3.27381 \cdot 10^{-8}$)

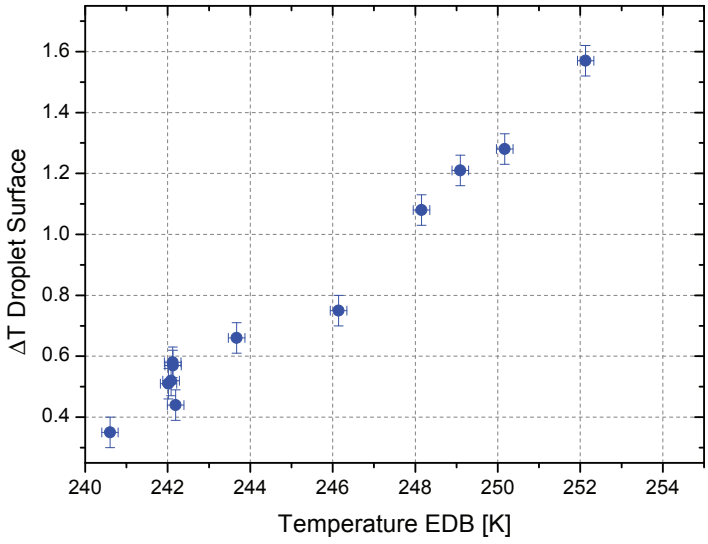

Figure 3.8: ΔT as a function of T of an experiment with feldspar microcline

3.6 Particle generation, mobility size selection and counting

Depending on the aerosol material, the particles are generated from a dry powder by a fluidized bed generator (FBG) or from a suspension by an atomizer. Both are operated with synthetic air.

For the experiments with hematite, a FBG (TSI, model 3400A) was used to generate the particles. The other mineral dusts were generated by a selfmade FBG consisting of a glass tube with a gas permeable membrane in the lower part of the tube. Under the membrane, glass spheres were confined to laminarize the ascending flow of synthetic air. The dust powder (depending on the material, mixed with glass or bronze beads) was placed on the membrane, and the synthetic air flow blew up the particles, providing the fluidized bed conditions. After the FBG the particles passed through a multiple orifice, rotating multistage impactor (type LPI-ROT 25/0018, 1995, Hauke GesmbH & Co KG, Gmunden, Austria) for eliminating large, agglomerated particles.

For cellulose a different aerosol generator was necessary. These particles are very light and “fluffy”, so that the FBG could not be used, because it blew up all the material in the system in a few minutes and the particles were too large for the experiment. The solution was found in form of a flask, which contains cellulose and bronze beads and was set on a magnetic stirrer, with a flow of 1 l/min synthetic air

above the material. The advantage of this method is that only the smallest particles have been carried away by the air flow, the larger particles remaining in the flask.

The BPWW, SNOMAX® and hematite were generated from a suspension by an atomizer (modified TSI Aerosol Generator). After the atomizer, the particles path through a diffusion dryer to evaporate the droplets.

After the generation, the particles have been size selected by an electrostatic classifier (model 3080, TSI [TSI, 2001]) in combination with a Long Differential Mobility Analyzer (Long DMA, model 3081) (figure 3.10).

At the entrance of the electrostatic classifier, a cyclone impactor was installed to deposit the particles larger than the cut-off diameter d_{50} (50% of the particles deposited) given by TSI [2001] as

$$d_{50} = \sqrt{\frac{9\pi\mu(\mathrm{Stk})W^3}{4\rho_p CQ}} \tag{3.48}$$

Stk gives the Stokes number, which is a dimensionless parameter that characterizes the inertia of a particle and its motion in a fluid, and is given with Stk = 0.23 by TSI [2001]. W is the nozzle diameter (W = 0.071 cm), Q the volume flow rate, ρ_p the particle density and C the Cunningham slip correction with:

$$C(d_p) = 1 + \mathrm{Kn}(\alpha + \beta \exp(-\gamma/\,\mathrm{Kn})) \tag{3.49}$$

$\alpha = 1.142$, $\beta = 0.558$ and $\gamma = 0.999$ [Allen and Raabe, 1985]. The Cunningham slip correction factor is necessary for describing the motion of small particles (diameter less than 1000 nm). In that size range, the assumption of the Stokes law, that the relative gas velocity to the particle motion is zero, is not valid. Gas molecules are able to move around the particle, which is called "slip", so the settling velocity is faster than predicted by Stokes law.

Hinds [1999] gives the following approximation for d_{50}, which works well for the conventional impactor and is accurate within 2% for $d_{50} > 0.2\,\mu$m:

$$d_{50}[\mu\mathrm{m}] = d_{50}\sqrt{C(d_{50})} - 0.078 \tag{3.50}$$

For the aerosol materials used, d_{50} is about 1 µm.

After the impactor, the aerosol flow passed the bipolar space-charge cloud of the radioactive isotope krypton 85 (^{85}Kr, β^--radiation, 687 keV, 99.6% and γ-radiation, 514 keV, 0.4%). The ions collide with the particles and after very short time, the particles are charged according to a known bipolar charge-distribution. The calculation of the particle charge is based on a model developed by Wiedensohler et al. [1986] which is an approximation of the Fuchs diffusion theory [Fuchs, 1963] [TSI, 2001]. Figure 3.9 shows the fraction of particles in air carrying between –6 and +6 elementary charges. The calculation bases on Wiedensohler and Fissan [1988]

and Kim et al. [2005]. The equation for the calculation of the fraction of particles carrying between 3 and 6 charges is based on a derivation by Gunn and Woessner [1956].

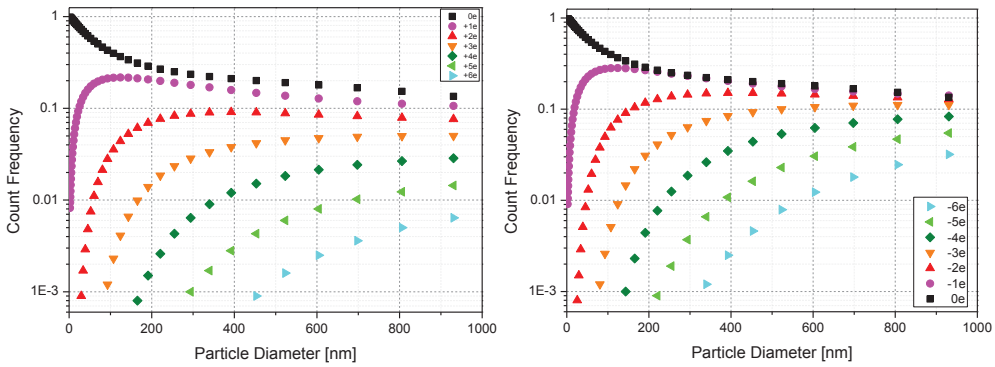

Figure 3.9: Amount of positive (left) and negative (right) charged particles as a function of the particle's diameter based on the calculation of Wiedensohler and Fissan [1988] with the mean free path taken from Kim et al. [2005]

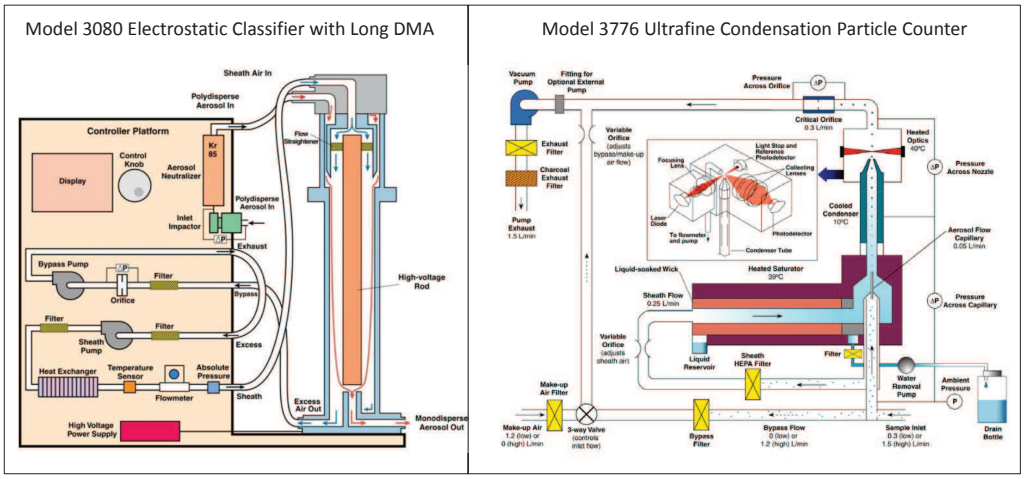

Figure 3.10: Schematic diagram of the Differential Mobility Analyzer (left panel) [TSI, 2001], and Condensation Particle Counter (right panel) [TSI, 2007]

Since larger particles with multiple charges have the same electrical mobility as smaller particles carrying a single elementary charge, larger, multi-charged particles reach the exit slit of the DMA. For instance, single charged particles with a mobility diameter of 320 nm have the same electrical mobility as double charged particles with a mobility diameter of 550 nm, or triple charged particles with a mobility diameter of 750 nm. Of course, an amount of larger particles influences the collision rate, and with that the freezing probability. Chapter 4 discusses this subject in detail for each aerosol material.

The flow containing size selected particle passes through the pre-cooler, and reaches the EDB. Some of the particles collide with a levitated droplet (usually between 1 and 3 particles in 30 s). After the EDB an Ultrafine Condensation Particle Counter (UCPC model 3776, TSI) (figure 3.10) counts the particle concentration. In the UCPC, the incoming aerosol flow gets splitted up into 0.05 l/min for analyzing, and 0.25 l/min as sheath flow. In the sheath flow circuit the particles are filtered out of the flow, and pass through a butanol-filled heated saturator (39 °C). The analyzing flow passes through a capillary, so that a stream of single particles exits the capillary. The aerosols and butanol vapor pass through the cooled condenser, and the particles grow to a detectable size before they reach the optical counting unit.

Beside the particle concentration, also a size spectrum of the aerosol particles can be recorded. The UCPC must be connected to the electrostatic classifier, and the complete voltage range of the DMA is scanned. For each voltage, the particle concentration is measured by the UCPC.

To get a precise information about the amount of single and multiple charged particles for each aerosol material and each mobility diameter which have been used, filter samples were prepared. Depending on the aerosol material, a 47 mm Nuclepore® filter (Whatman Nuclepore Track-Etched-Membranes, 0.2 µm pore size) or a TEM grid (carbon film on 200 mesh Ni grids) is used for particle sampling. The filters were analyzed by SEM, and the images were analyzed using the open source program ImageJ. The images show the topviw of the particles lying on the filter. Using ImageJ, the number of pixels of each particle could be analyzed and, assuming that the particles had a spherical shape, the area equivalent diameter was calculated.

3.7 Aerosol material used in this work

Hematite

The hematite particles used for the experiments in the INUIT project were synthesized at IMK-AAF by Sarah Jäger, by growing pseudo cubic particles with a side length of 300 nm and 900 nm (figure 3.11a). The particles were synthesized by hydrolyzing ferric chloride ($FeCl_3$) solutions in NaOH, according to the gel-sol method Kandori et al. [2002] and Sugimoto and Sakata [1992]).

The particles were available as a suspension in deionized water (NANOpurer® Infinity Base Unit, Barnstead-Thermolyne Corporation), or as freeze dried powder. Both samples have been used in the experiments. The suspension was generated with an TSI atomizer (Aerosol Generator 3076, TSI), operated with synthetic air, and the dry powder was generated using a fluidized bed generator (model 3400A, TSI). To investigate the possible influence of a particle surface morphology, we have milled dry hematite particles by stirring a mixture of hematite particles and bronze beads.

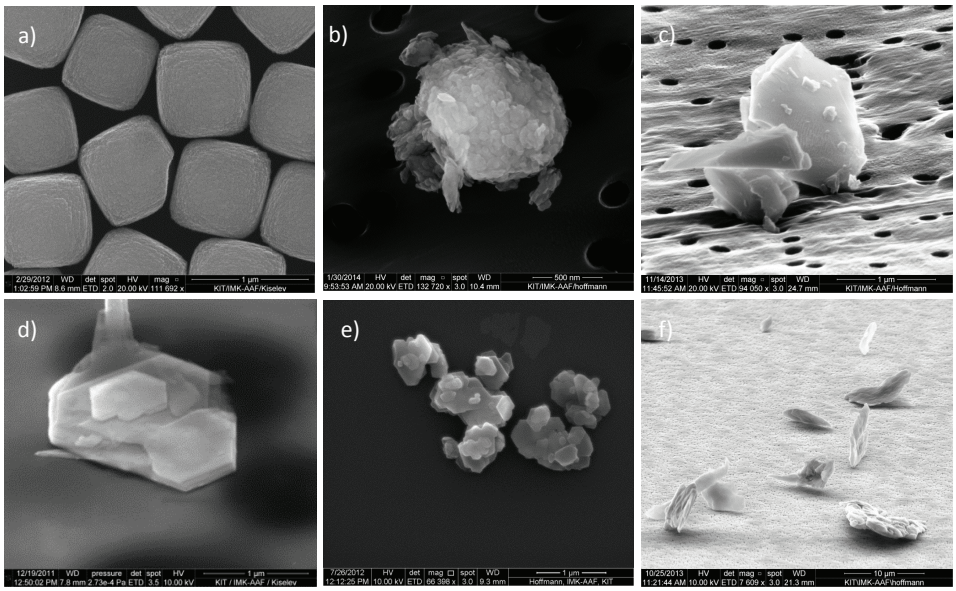

Figure 3.11: ESEM images of a) pseudo cubic hematite; b) illite; c) feldspar; d) kaolinite Fluka; e) kaolinite KGa-1b; f) microcrystalline cellulose

The milled particles were size selected with a mobility diameter of 620 nm, so that the particles are still much larger than the 300 nm particles, but small enough to ensure that no unmilled 970 nm particles were entering the aerosol flow. For the particles with a mobility diameter of 300 nm and 970 nm generated in the atomizer, the particle concentration was about $400\,\mathrm{cm}^{-3}$ and $280\,\mathrm{cm}^{-3}$, respectively. The particle concentration for the milled hematite particles generated by the TSI fluidized bed generator with a mobility diameter of 620 nm was chosen between $200\,\mathrm{cm}^{-3}$ and $600\,\mathrm{cm}^{-3}$. For the generation of the 970 nm particles using the TSI fluidized bed generator, the particle concentration was about $150\,\mathrm{cm}^{-3}$. The used particle density is $\rho_{\mathrm{hematite}} = 5200\,\mathrm{kg/m}^3$ [Terzaghi et al., 1996] and the Brunauer-Emmett-Teller (BET) surface area for cubic and milled hematite is $2.2\,\mathrm{m}^2\mathrm{g}^{-1}$ and $3.7\,\mathrm{m}^2\mathrm{g}^{-1}$, respectively [Hiranuma et al., 2014b].

Feldspar

To analyze the ice nucleation activity of feldspar in different freezing modes at IMK-AAF, we obtained the K-feldspar from Dr. Benjamin J. Murray (University of Leeds), and Dr. Martin Ebert (INUIT partner from the Technical University of Darmstadt). Most feldspar particles are agglomerates of crystalline fragments of different sizes (cf. figure 3.11c).

The particle number concentration was about $70\,\mathrm{cm}^{-3}$ for a mobility diameter of 550 nm and about $90\,\mathrm{cm}^{-3}$ for a mobility diameter of 320 nm in case of K-feldspar generated by an atomizer. For the generation with a fluidized bed generator (FBG) (selfmade one, described in section 3.6), the particle concentration was about $120\,\mathrm{cm}^{-3}$ for a mobility diameter of 550 nm and about $90\,\mathrm{cm}^{-3}$ for a mobility diameter of 320 nm. The Na/Ca-feldspar was only generated by an atomizer and the particle concentration was about $70\,\mathrm{cm}^{-3}$ for a mobility diameter of 550 nm and about $200\,\mathrm{cm}^{-3}$ for a mobility diameter of 320 nm. The density of feldspar was assumed to be $\rho_{\mathrm{feldspar}} = 2550\,\mathrm{kg/m}^3$ (according to [Okrusch, 2014] who gives a density of $2500\,\mathrm{kg/m}^3$ to $2600\,\mathrm{kg/m}^3$ for feldspar). The BET surface area is $1.8\,\mathrm{m}^2\mathrm{g}^{-1}$ for the K-feldspar and $1.9\,\mathrm{m}^2\mathrm{g}^{-1}$ for Na/Ca-feldspar (cf. table D.1).

Kaolinite

In my diploma thesis I have already investigated Kaolinite natural (Fluka, from the company Sigma Aldrich) (figure 3.11d). In this work, the results of kaolinite Fluka will be compared with kaolinite KGa-1b from the Clay Mineral Society (Purdue University, West Lafayette, Indiana, USA) (figure 3.11e). This kaolinite is highly pure. According to CMS Source Clay Physical/Chemical Data and as confirmed by our own microprobe energy-dispersive X-ray (EDX) analysis, KGa-1b consists of more than 95w% kaolinite, although anatase (TiO_2), iron oxides, quartz, and micas are observed in trace amounts (Robert J. Pruett and Harold L. Webb [1993], Hoffmann et al. [2013a]). Kaolinite Fluka contains 82w% kaolinite, 7w% feldspar, 5w% quartz and 1w% anatase (XRD measurements by Dr. Martin Ebert, INUIT partner from University of Darmstadt). The particles have been generated with a FBG, and the mobility diameters 320 nm and 550 nm were selected. The particle concentration was about $50\,\mathrm{cm}^{-3}$ for each kaolinite type and size. The bulk material density of kaolinite was assumed to be $\rho_{\mathrm{kaolinite}} = 2500\,\mathrm{kg/m}^3$, according to [Okrusch, 2014], who provides the values between $2100\,\mathrm{kg/m}^3$ and $2600\,\mathrm{kg/m}^3$. The BET surface area is $8.6\,\mathrm{m}^2\mathrm{g}^{-1}$ for kaolinite Fluka and $12.2\,\mathrm{m}^2\mathrm{g}^{-1}$ for kaolinite KGa-1b (cf. table D.1).

Illite

The illite particles are almost spherical agglomerates of very small platelets (figure 3.11b). The particles used in this experiments have been generated by a FBG and had a mobility diameter of 150 nm, 320 nm, 550 nm and 750 nm. The particle concentration was about $100\,\mathrm{cm}^{-3}$ for a mobility diameter of 750 nm and several hundreds per cubic centimeter for the other particle sizes. The bulk particle density is $\rho_{\mathrm{illite}} = 2650\,\mathrm{kg/m}^3$, according to [Vinx, 2015] who provides a density between $2600\,\mathrm{kg/m}^3$ and $2900\,\mathrm{kg/m}^3$. The BET surface area is $124\,\mathrm{m}^2\mathrm{g}^{-1}$ (cf. table D.1).

Birch Pollen Washing Water

Manfred Schäfer and Michael Koch analyzed birch pollen (Birch, European White, Betula Pendula, non-defetted, Greer Labs) washing water (BPWW) in the contact mode as part of their diploma thesis [Schäfer, 2014] and Bachelor's thesis [Koch, 2014], respectively.

The BPWW has been prepared by washing of 3 g of birch pollen in 100 ml of deionized water (NANOpure® Infinity Base Unit, Barnstead-Thermolyne Corporation). After mixing with a magnetic stirrer, the suspension was filtered by a filter with a cut-off at 8 µm – 10 µm (Schleicher and Schuell, type 589.5, 185 mm). The pollen grains have sizes of about 20 µm – 30 µm, so they are too large to penetrate the filter, and only the washed-out components are present. The BPWW is generated with an atomizer and dried in the diffusion dryer. The dried residuals are size selected with a mobility diameter of 550 nm and 760 nm. The particle concentration was about $500\,\mathrm{cm}^{-3}$. The effective density of the BPWW particles is $\rho_{\mathrm{BPWW}} = 1560\,\mathrm{kg/m}^3$ as measured by Manfred Schäfer [Schäfer, 2014].

Illite Mixed with Birch Pollen Washing Water

As a model substance possibly relevant for ice formation in the atmosphere, the mixture of a mineral dust with BPWW was investigated. As mineral dust, illite NX was chosen because of the almost spherical shape of the particles. For one sample 50 g of illite NX have been mixed with BPWW prepared with 1.5 g, 2.2 g, 3 g or 6 g of birch pollen washed in 100 ml of deionized water, respectively. To show that the amount of washed out material increases with mass of pollen grains, the 100 ml of BPWW was dried out and weighted. The results are shown in table 3.2.

Table 3.2: Amount of residuals of BPWW

Concentration [g/100ml]	amount of residuals [g]
1.5	0.47±0.01
2.2	0.54±0.01
3	0.68±0.01
6	1.36±0.01

The mixtures were kept in the fridge over night. The next day, it was transferred into a Petri dish and dried in a vacuum chamber, and after that in a clean room box (Mobile Cleanroom Box MRB 01, Colandis). The dry mixture (figure 3.12) was crushed to a fine powder in a mortal and air dispersed with a FBG.

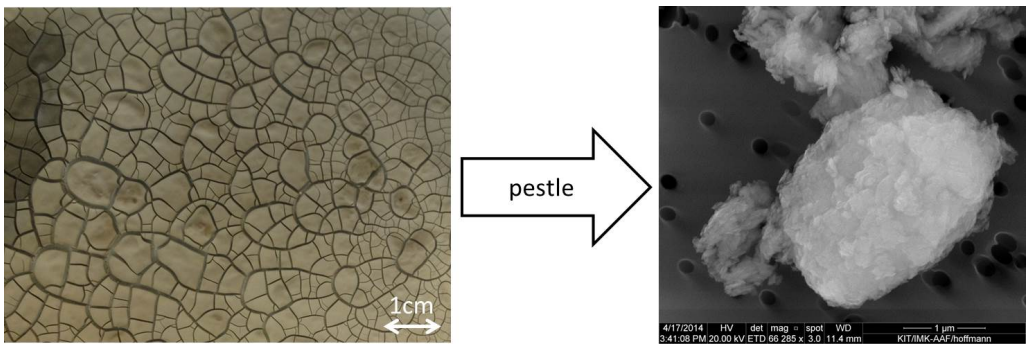

Figure 3.12: Dried illite NX mixed with BPWW in a petri dish (left panel), and the same material after pestling (collected on a Nuclepore® filter) (right panel)

The particles had a mobility diameter of 750 nm and the particle concentration was between 40 cm^{-3} and 250 cm^{-3}. The effective densities are shown in figure 5.16, and the BET surface areas are shown in table D.1.

Microcrystalline Cellulose

Figure 2.13 [Metzler, 2014] shows the schematic construction of the cell wall and the microfibril structure as well as the cellulose molecules. A single microfiber is built of an inner bundle of microcrystalline cellulose, surrounded by paracrystalline cellulose and an outer layer of hemicellulose which connects the single microfibers.

The microcystalline cellulose, contains particles with lengths up to several micrometers, which are too large for size selection with the DMA used in the experiment. To produce submicron particles, the cellulose was milled with bronze beads on a magnetic stirrer for two days. Since these particles are very light and fluffy, a special aerosol generator has been used to generate the aerosol. The method is described in section 3.6. The set mobility diameter was 320 nm and 800 nm and the particle concentration was about 50 cm^{-3}. The density of cellulose is 1460 kg/m^3 [Sun, 2005].

SNOMAX®

SNOMAX® is a commercial product containing fermented, pelletized, freeze-dried and irradiated Pseudomonas Syringae bacteria (Johnson Controls Snow, Colorado, USA). The experiments reported here are done by Manfred Schäfer as part of his diploma thesis Schäfer [2014]. 0.75 g SNOMAX® has been suspended in 1 l deionized water. To generate particles, we used an atomizer. We selected the mobility diameters 320 nm and 550 nm, and the particle concentration was about

600 cm^{-3} and 400 cm^{-3}, respectively. The effective density of SNOMAX® was found to be 1400 kg/m^3 [Schmidt, 2013]. Wex et al. [2015] provide a density between 1200 kg/m^3 and 1500 kg/m^3.

3.7.1 Aerosol particles characterization methods

A very helpful instrument for characterizing the aerosol particles is a Scanning Electron Microscope (SEM). The microscope is an Environmental SEM (ESEM) (FEI Quanta 650 FEG) with an Everhart-Thornley-Detector (ETD) for detecting secondary electrons. The energy dispersive X-ray (EDX) spectra are detected using a Bruker Quantax 400. With this instrument it was possible to analyze the chemical composition of single particles. This technique is suitable for analyzing minerals or metals, but it is not suitable for the identification of a small amount of biological material on mineral dust. A high vacuum coating system (Leica EM MED020) is used for coating of non-conductive material with platinum to dispose of the excess electrons. Because of the coating, EDX spectra shown in this work can have a platinum peak at 2.1 keV.

For each particle type and size, filter samples have been prepared to get information about the size distribution and the chemical composition of the aerosol. Furthermore, the residuals of droplets ejected onto a Si-wafer for verification of the collision rate have been analyzed by SEM.

As already mentioned, the detection of a small amount of biological material on a mineral dust particle is not possible using SEM. Because of that, we tried to obtain additional information using a fluorescence microscope. The analyzes of the illite/BPWW-mixture samples were performed by Artiom Skripka (research assistant, IMK-AAF, KIT), and supervised by Dr. Masanari Takamiya and Maryam Rastegar (Institute of Toxicology and Genetics (ITG), KIT). The study was conducted with the Confocal microscope Leica TCS SP5. We prepared samples with a suspension of illite, illite mixed with BPWW, and pure BPWW on a microscope slide (Superfrost Plus Microscope Slides, Thermo Scientific) and dried them in the cleanroom box (Mobile Cleanroom Box MRB 01, Colandis). After drying, an oil film (Type F Immersion liquid, Leica) and a glass cover slide were placed on top of the sample. The oil prevents chromatic aberrations. The same oil is also used between the sample and the microscope objective. The excitation wavelengths 405 nm, 458 nm and 496 nm have been used. Pure illite shows fluorescence at excitation with a wavelength of 405 nm, but not for longer wavelength. The biological material located on illite shows an additional a fluorescence signal for the excitation wavelength of 458 nm and 496 nm, so it was possible to distinguish the fluorescence signal of illite and BPWW (cf. figure 5.17). Unfortunately, the resolution was not high enough to see the location of BPWW on the surface of single illite particles.

Some aerosol particles have been characterized by an Aerosol Particle Mass Analyzer (APM) (model 3601, Kanomax). This instrument allows to classify incoming particles according to their charge to mass ratio. The sample flow rate passing through the APM is 0.3 l/min and the measurable particle mass range is between 0.001 fg and 1000 fg [Kan, 2013]. The classifier consists of two cylindrical rotating electrodes. Only particles with mass m satisfying the following equation would pass through the APM:

$$m\omega^2 r = NeE_{\mathrm{APM}} \tag{3.51}$$

where ω is the rotation frequency of the APM, r the particle location, N the number of elementary charge e, and E_{APM} is the electric field strength.

By changing the voltage and therefor E_{APM}, and keeping ω and r constant, the ratio Ne/m defines the selection conditions. Using this method, it is possible to get a mass distribution of particles with a certain electrical mobility. In the size range of the experiments ($200\,\mathrm{nm} \leq d_m \leq 700\,\mathrm{nm}$), the multi charged particles with the same Ne/m ratio can be identified easily, and they do not distort the results. The method is described in detail in [Ehara et al., 1996]. This method was used in attempt to detect the differences in mass of pure illite and illite mixed with BPWW (cf. section 5.17).

The effective surface area of bulk powder samples of kaolinite, illite and feldspars have been measured with Brunauer-Emmett-Teller (BET) method (courtesy of Tanja Kisely (Institute for Nuclear Waste Disposal (INE), KIT). By using the Langmuir absorption equation, which relates the absorption of nitrogen molecules on a surface to the gas pressure, and the size of the gas molecules, the surface per gram of the sample material can be calculated. The method is described in detail in Brunauer et al. [Brunauer et al., 1938].

3.8 Experimental routine

In this section, the contact freezing experiments and the immersion freezing experiments are described. Before starting of a heterogeneous freezing experiments, a short particle-free experiment without aerosols is performed to check whether the experimental setup is clean and the water is not contaminated. The system is considered clean if the droplet is not freezing homogeneously above $-33\,^{\circ}\mathrm{C}$.

The contact and immersion freezing experiments are shown in figure 3.13. The first droplet was injected as soon as a stable particle concentration was reached. The residence time for the levitated droplet was 30 s. If the droplet freezes during these 30 s, the freezing time was recorded, and the droplet was ejected by varying the AC and DC. Then a new droplet was injected and the routine starts again.

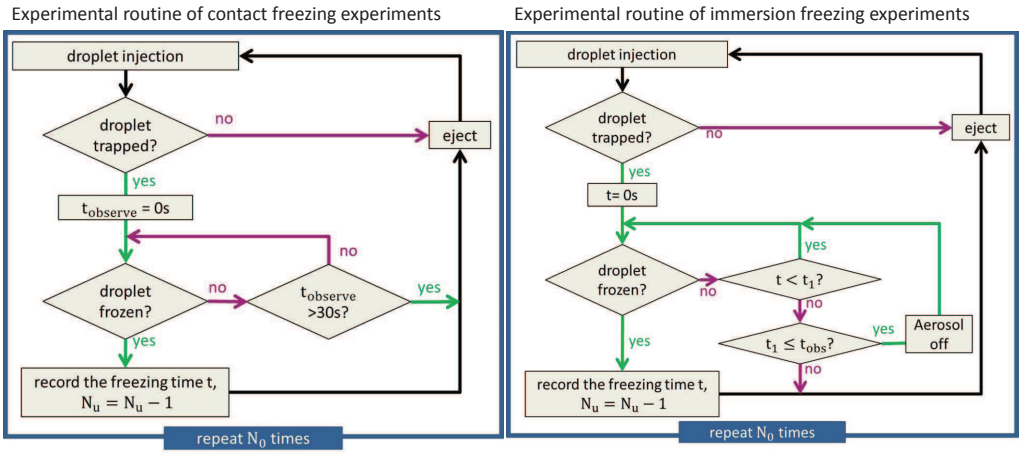

Figure 3.13: Experimental routine of the contact and immersion freezing experiments

To study the immersion freezing, the droplet was exposed to the aerosol flow briefly, allowing for collection of several particles. The aerosol flow was then switched off by applying the voltage to the electrostatic precipitator. A droplet was injected and, depending on the particle concentration, the aerosols were in the flow long enough that the droplet can collect two particles at least. If the droplet froze during this time, the freeze time was recorded, the droplet was ejected and a new droplet was injected. If the droplet did not freeze during this time, the particles were removed from the flow by the electrostatic precipitator, and now the freezing could only be initiated by the particles, the droplet had already collected, and so only due to immersion mode.

For experiments at temperatures higher than $-15\,°C$ the aerosol flow had to be humidified. Without humidification, the droplet would evaporate too fast to levitated it stably for 30 s. A particle-free flow with a certain relative humidity is mixed to the aerosol flow, so that the dew and frost point of the aerosol flow is lower than the coldest electrode of the EDB to prevent ice growth.

4 Evaluation of experimental results

4.1 Possible freezing scenarios in the experiment

To perform contact freezing experiments the droplet remains in the EDB for 30 s at longest. During this time, some of the aerosol particles collide with the droplet. The following passage (shown as indented text) is citing closely the discussion from [Hoffmann et al., 2013a]:

> A supercooled droplet suspended in a flow of aerosol particles may freeze along different pathways, either via contact freezing or immersion freezing due to the previously collected particles (figure 4.1). The freezing may occur on the first contact with an ice nucleating particle (INP). Alternatively, the droplet may collect one or more INP without freezing and then freeze at the n-th contact with an INP. Finally, the droplet can collect one or more INP and freeze along the immersion freezing pathway. In the following we show how the different freezing mechanisms can be handled separately.
>
> In a system of N_0 identical water droplets supercooled to a constant temperature T and subjected to a constant rate of contacts with aerosol particles that are taken up by the droplets, freezing is a random process described by a rate equation:
>
> $$\frac{dN_u}{dt} = -J_{\mathrm{tot}}(t) \cdot N_u \tag{4.1}$$
>
> where N_u is the number of unfrozen droplets and $J_{\mathrm{tot}}(t)$ is the total rate of freezing events.
>
> To account for the different freezing mechanisms figure 4.1 and assuming that droplets freeze independently, we separate the total rate of freezing into two parts – the rate of immersion freezing $J_i(t)$ and the rate of contact freezing J_c:
>
> $$J_{\mathrm{tot}} = J_i + J_c \tag{4.2}$$
>
> According to the classical nucleation theory for heterogeneous nucleation [Pruppacher and Klett, 2004], the total rate of immersion freezing would be a product of a nucleation rate coefficient j_i, the surface of a single immersed ice nucleating particle S_{INP}, and the number of particles in the droplet n_{INP}. Assuming that all particles are identical, and taking into account that the number of particles

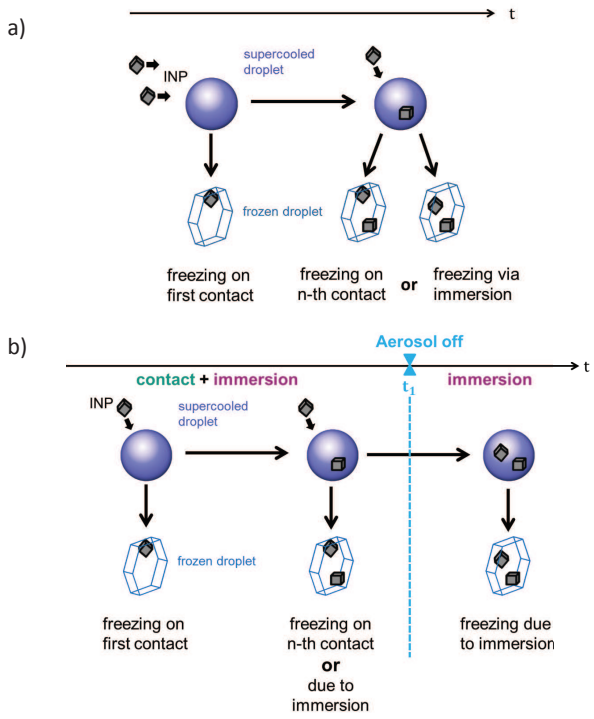

Figure 4.1: Sketch of possible freezing scenarios in a) contact and b) immersion freezing experiments

collected by the droplet n_{INP} after time t is the product of the collection rate n_c and time t, we obtain

$$J_i = S_{\mathrm{INP}} \cdot j_i \cdot n_c \cdot t. \tag{4.3}$$

The rate of contact freezing events is given by the collection rate n_c times the probability of droplet freezing upon a single contact (contact freezing probability) e_c:

$$J_c = n_c \cdot e_c. \tag{4.4}$$

Combining equations 4.2, 4.3, and 4.4, substituting into eq. 4.1 and integrating yields

$$\int_{N_0}^{N_u} \frac{dN_u^{'}}{N_u^{'}} = -\int_0^t n_c \left(S_{\mathrm{INP}} j_i t^{'} + e_c \right) dt^{'}, \tag{4.5}$$

$$\ln\left(\frac{N_u}{N_0}\right) = -\frac{1}{2} S_{\mathrm{INP}} n_c j_i t^2 - n_c e_c t. \tag{4.6}$$

Equation 4.6 includes a quadratic time-dependent term describing the immersion freezing and the linear time-dependent term describing the contact freezing. A direct implication of such a functional form is obvious: if we assume the rate

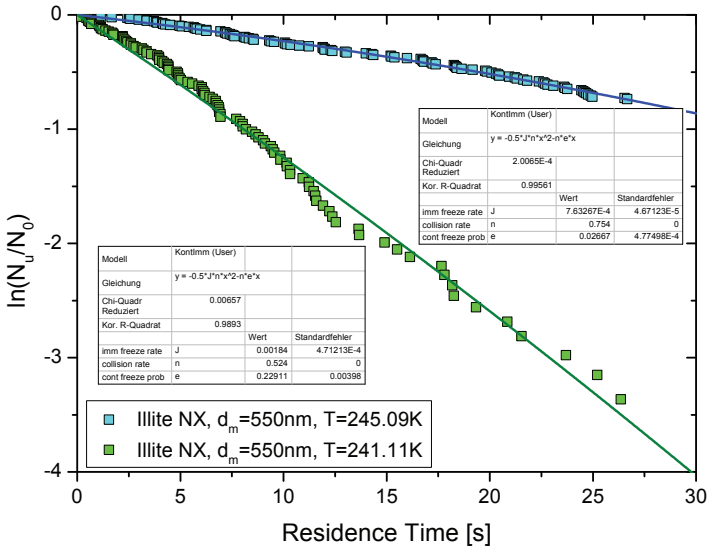

Figure 4.2: Experimental results of contact freezing experiments with illite NX (mobility diameter 550 nm) at two different temperatures

of contact freezing events J_c being very small, the quadratic term (immersion freezing) will dominate the form of the function $\ln(N_u/N_0)$ plotted against time, which will have a square law shape; vice versa, if contact freezing dominates, the equation simplifies to

$$\ln\left(\frac{N_u}{N_0}\right) = -n_c \cdot e_c \cdot t \tag{4.7}$$

which yields a linear dependence of $\ln(N_u/N_0)$ on time.

Figure 4.2 shows typical diagrams with the residence time of the droplet on the x-axis and the $\ln(N_u/N_0)$ on the y-axis – in the following, this kind of curves are called "freezing curve".

The freezing curves are fitted using eq. 4.6. Because of the linearity of the freezing curve, the contact mode dominates in these experiments.

To perform immersion freezing experiments, the droplet can collect particles and freeze due to contact mode while $t < t_1$. For $t > t_1$, the particles are separated from the flow using the electrostatic precipitator. For $t < t_1$ the freezing curve can be fitted using equation 4.6, and for $t > t_1$, the function is given by:

$$\ln\left(\frac{N_u}{N_0}\right) = -n_c \cdot t_1 \cdot (e_c + j_i \cdot t - \frac{1}{2} \cdot j_i \cdot t_1) \tag{4.8}$$

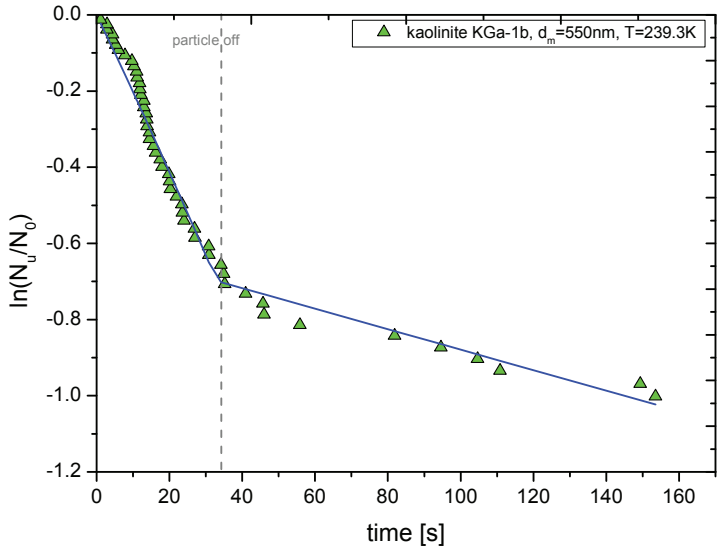

Figure 4.3: Experimental results of immersion freezing experiment with kaolinite KGa-1b (mobility diameter 550 nm). Gray dashed line: time when particles are switched off, blue solid line: combination of equations 4.6 and 4.8

Applying the combination of equations 4.6 and 4.8 one is able to obtain the e_c and j_i from a single experiment as shown in figure 4.3.

To demonstrate the influence of different immersion freezing rates and contact freezing probabilities on the shape of the freezing curve, some experiments were simulated numerically.

In the simulation, a particle collides with a droplet and either initializes freezing due to the contact mode or immersion mode, or the droplet does not freeze et all. When the droplet freezes, the freezing time and the freezing mode are recorded and a new droplet is analyzed. If the droplet did not freeze, another particle can collide and initialize freezing.

For the simulation an experiment of 150 droplets and a collision rate of $0.524\,\mathrm{s}^{-1}$, a typical value for experiments with illite NX were chosen. The chosen contact freezing probabilities were 0.1 (figure 4.4), 0.23 (figure 4.5), 0.36 (figure 4.6), and 0.9 (figure 4.7). The individual freezing events are plotted in the left panel for each freezing mode separately. Right panels in the figures 4.4–4.7 show the simulated freezing curves. The solid lines show the fits according to equation 4.6 (black) or 4.7 (magenta). The gray dashed lines show the variability of the $\ln(N_u/N_0)$ curve (cf. section 4.4).

For each contact freezing probability, three different immersion freezing rates are assumed to see the influence on the shape of the freezing curve. For a small contact freezing probability of 0.1, even the immersion freezing rate in the range of 10^{-3} shows a significant change in the shape of the freezing curve (figure 4.4a), thus the higher the immersion freezing rate the larger the change in shape. The influence of an immersion freezing rate in the range of 10^{-3} is lower for higher contact freezing probabilities of 0.23, 0.36 or 0.9. Here, less than 5% of the droplets are frozen in immersion mode, which is an amount we can not identify in our experiments. For more than 5%, the influence on the shape of the freezing curve is strong enough to be identified.

If the immersion freezing rate is very high, so that immersion freezing could occure before a new particle collided with the droplet, the influence of immersion freezing can not be seen in the shape of the freezing curve anymore. The freezing curve has a linear shape although most freezing events are initiated by immersion freezing (figure 4.8). This case is discussed in section 5.7.

Let's now look for the probability, that a particle can penetrate the droplet surface on a collision. For liquids the surface energy density is equal to the surface tension so σ can be given in $\mathrm{J/m^2}$ or N/m. Vargaftik et al. [1983] give a interpolating equation for the surface tension of water between 0 °C and 374 °C as:

$$\sigma = B\left(\frac{T_c - T}{T_c}\right)^{\mu}\left(1 + b\left(\frac{T_c - T}{T_c}\right)\right) \tag{4.9}$$

where the critical temperature $T_c = 647.15\,\mathrm{K}$, $B = 235.8 \cdot 10^{-3}\,\mathrm{N/m}$, $b = -0.625$, and $\mu = 1.256$. Although the temperature range given in this paper is only for temperatures above 0 °C, the surface tension to the temperatures of −30 °C was extrapolated. Figure 4.9 compares the surface energy of water at the projection area of a spherical particle with the kinetic energy of a colliding particle. To penetrate the droplet surface, the kinetic energy of a particle have to be larger than the surface tension multiplied with the projection area of the particle. As maximum and minimum values for the kinetic energy of colliding particles, the kinetic energy of a hematite particle and a polystyrene particle are calculated, respectively. The kinetic energy $E_{\mathrm{kin}} = \frac{1}{2} m_p v^2$ of the particles are not higher than the surface energy of water at the projection area of the particle until the particle reach a diameter of 200 µm for hematite and 1000 µm for polystyrene. This plot shows that it is unlikely that a colliding particle penetrate the droplet surface.

Is a particle already located on the droplet, it could be possible, that the particle sinks into the droplet. Oettel and Dietrich [2008] reports a vertical shift Δh for particles located on a liquid surface. Since the particle diameters is much smaller than the droplet diameter, the droplet surface can be assumed as flat suface. For a hematite particle with a diameter of 1 µm located on top of a droplet, the weight force would be $2.7 \cdot 10^{-14}\,\mathrm{N}$ and $\Delta h \approx 6.2 \cdot 10^{-8}\,\mu\mathrm{m}$ (using a contact angle between water and hematite of 47° [Shang et al., 2008]). Δh is nine orders of magnitude smaller

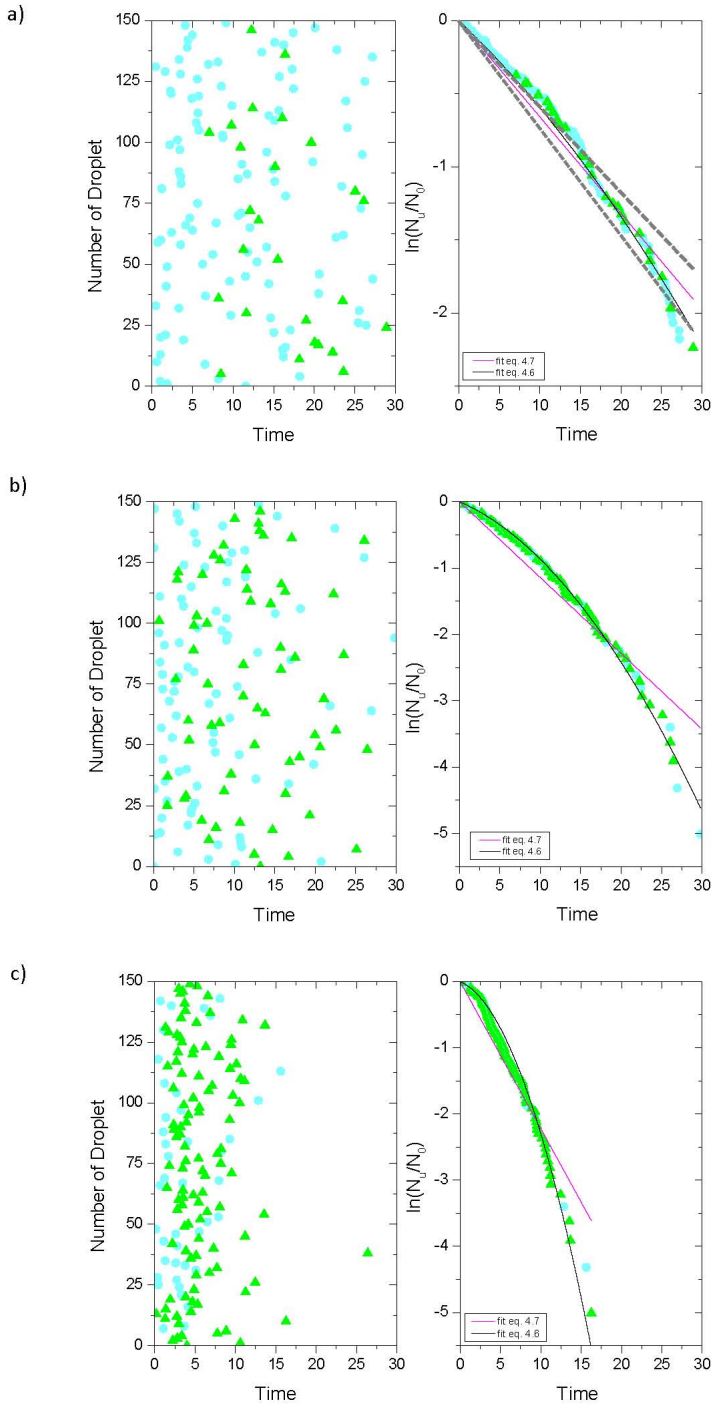

Figure 4.4: Simulation of an experiment with 150 droplets, a collision rate of $0.524\,\mathrm{s}^{-1}$, a contact freezing probability of 0.1, and an assumed immersion freezing rate per particle of a) $0.001\,\mathrm{m}^{-2}\mathrm{s}^{-1}$, b) $0.01\,\mathrm{m}^{-2}\mathrm{s}^{-1}$, and c) $0.1\,\mathrm{m}^{-2}\mathrm{s}^{-1}$, Freezing event due to contact mode (blue dots) or immersion mode (green triangles), gray dashed line: 10 %, variability of the slope

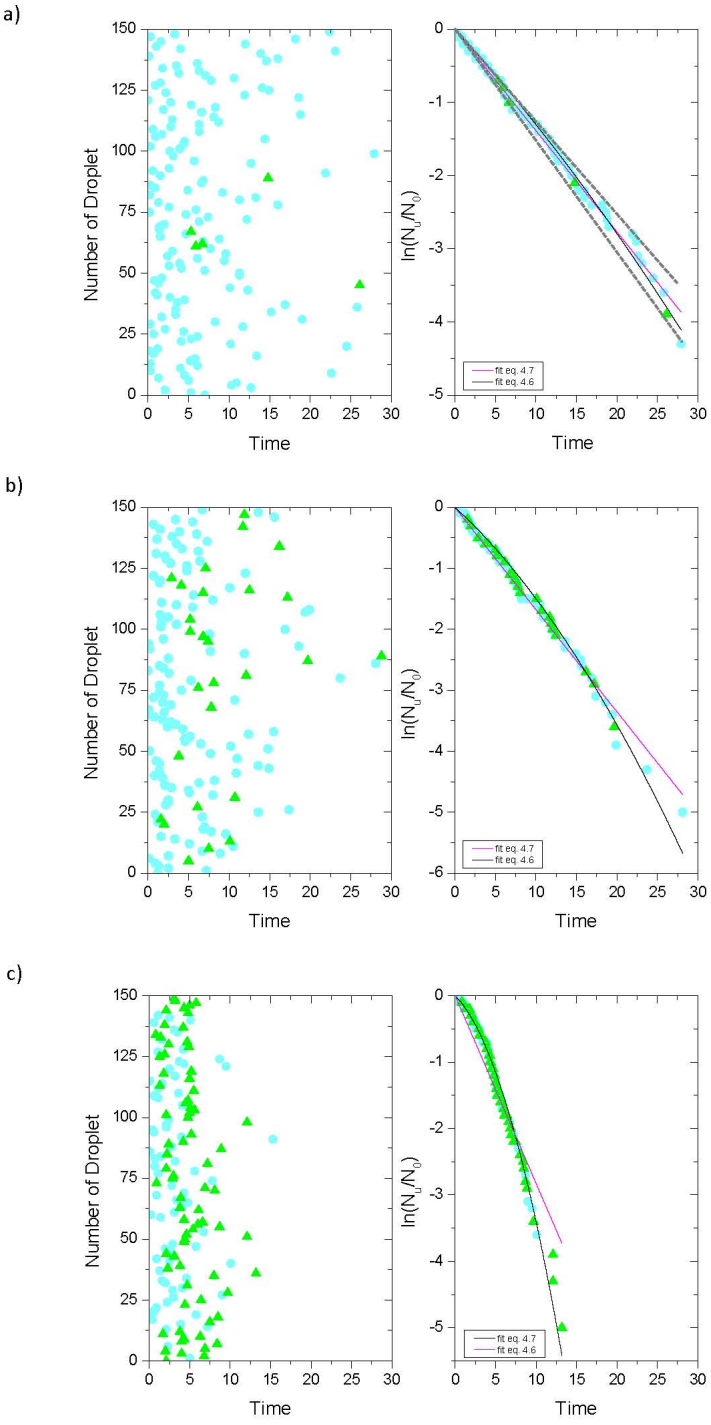

Figure 4.5: Simulation of an experiment with 150 droplets, a collision rate of $0.524\,\mathrm{s}^{-1}$, a contact freezing probability of 0.23, and an assumed immersion freezing rate per particle of a) $0.001\,\mathrm{m}^{-2}\mathrm{s}^{-1}$, b) $0.01\,\mathrm{m}^{-2}\mathrm{s}^{-1}$, and c) $0.1\,\mathrm{m}^{-2}\mathrm{s}^{-1}$, Freezing event due to contact mode (blue dots) or immersion mode (green triangles)

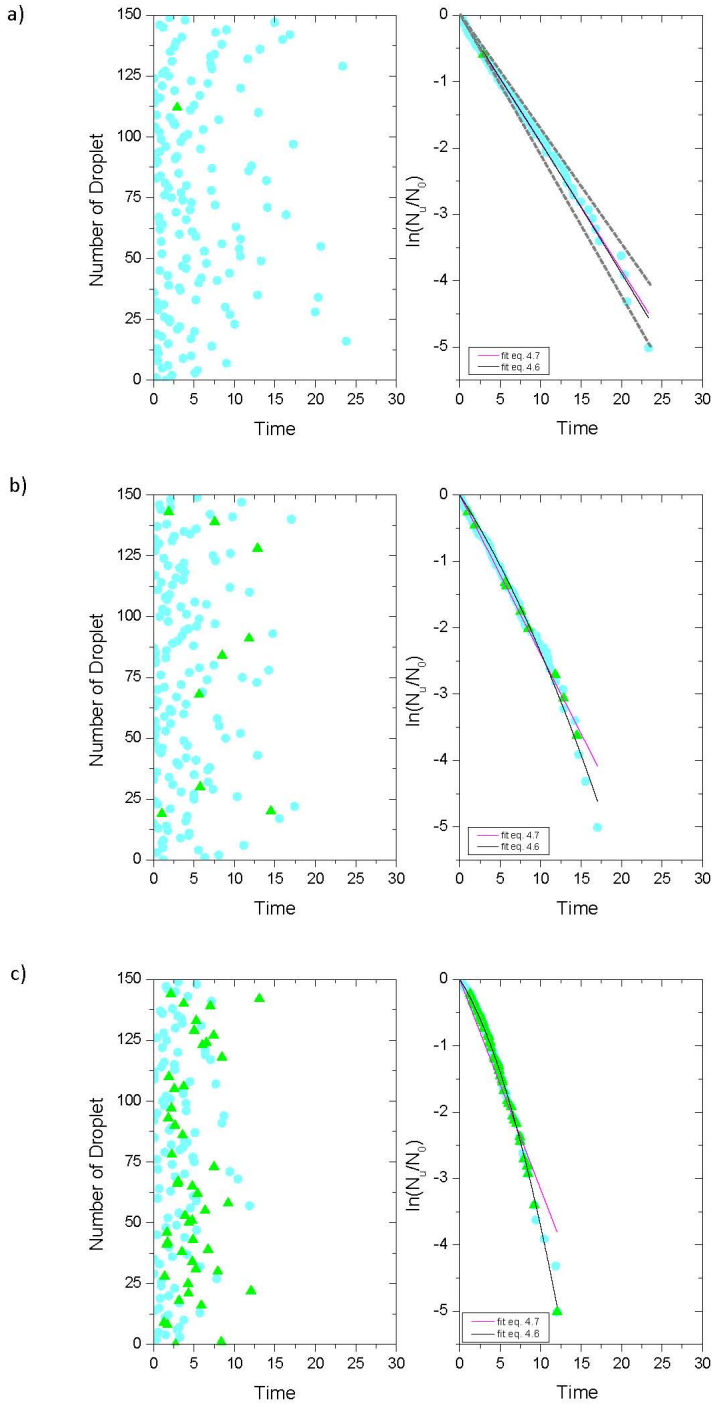

Figure 4.6: Simulation of an experiment with 150 droplets, a collision rate of $0.524\,\mathrm{s}^{-1}$, a contact freezing probability of 0.36, and an assumed immersion freezing rate per particle of a) $0.001\,\mathrm{m}^{-2}\mathrm{s}^{-1}$, b) $0.01\,\mathrm{m}^{-2}\mathrm{s}^{-1}$, and c) $0.1\,\mathrm{m}^{-2}\mathrm{s}^{-1}$, Freezing event due to contact mode (blue dots) or immersion mode (green triangles), gray dashed line: 10% variability of the slope

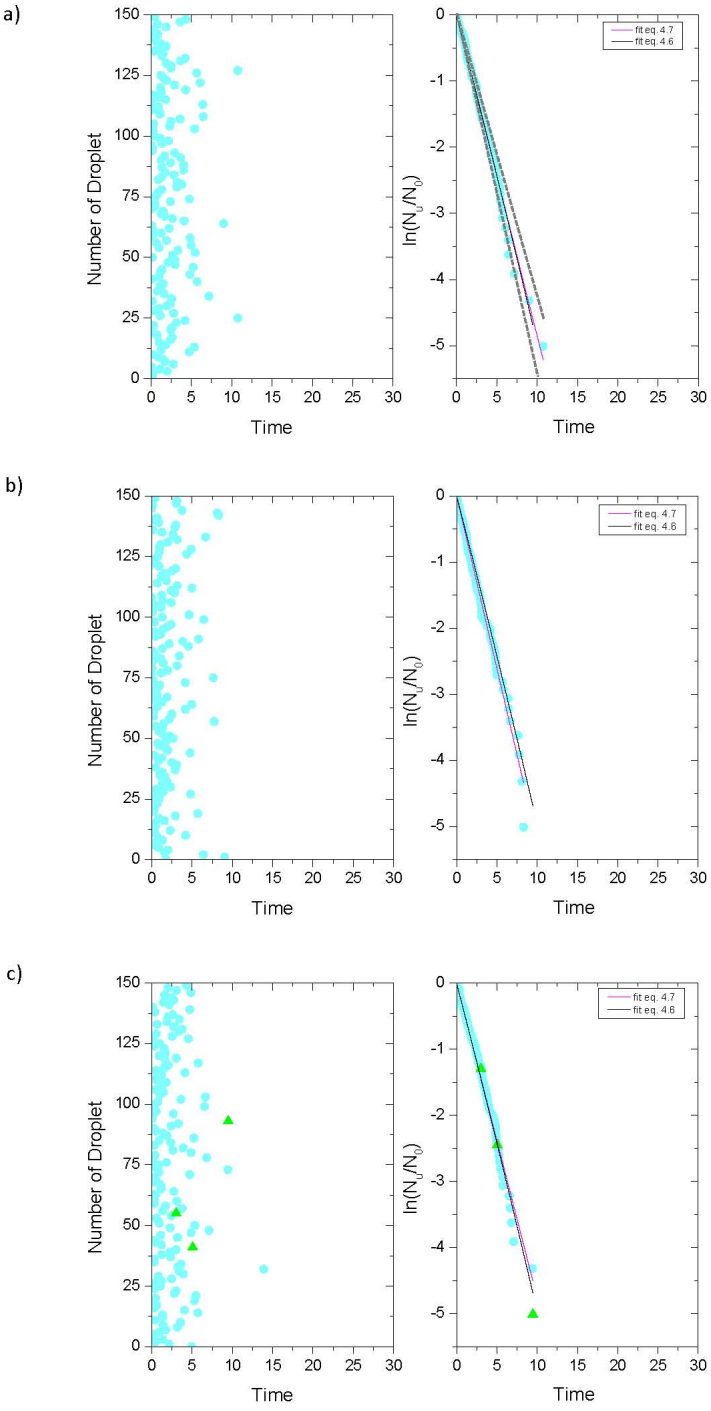

Figure 4.7: Simulation of an experiment with 150 droplets, a collision rate of $0.524\,\mathrm{s}^{-1}$, a contact freezing probability of 0.9, and an assumed immersion freezing rate per particle of a) $0.001\,\mathrm{m}^{-2}\mathrm{s}^{-1}$, b) $0.01\,\mathrm{m}^{-2}\mathrm{s}^{-1}$, and c) $0.1\,\mathrm{m}^{-2}\mathrm{s}^{-1}$, Freezing event due to contact mode (blue dots) or immersion mode (green triangles), gray dashed line: 10% variability of the slope

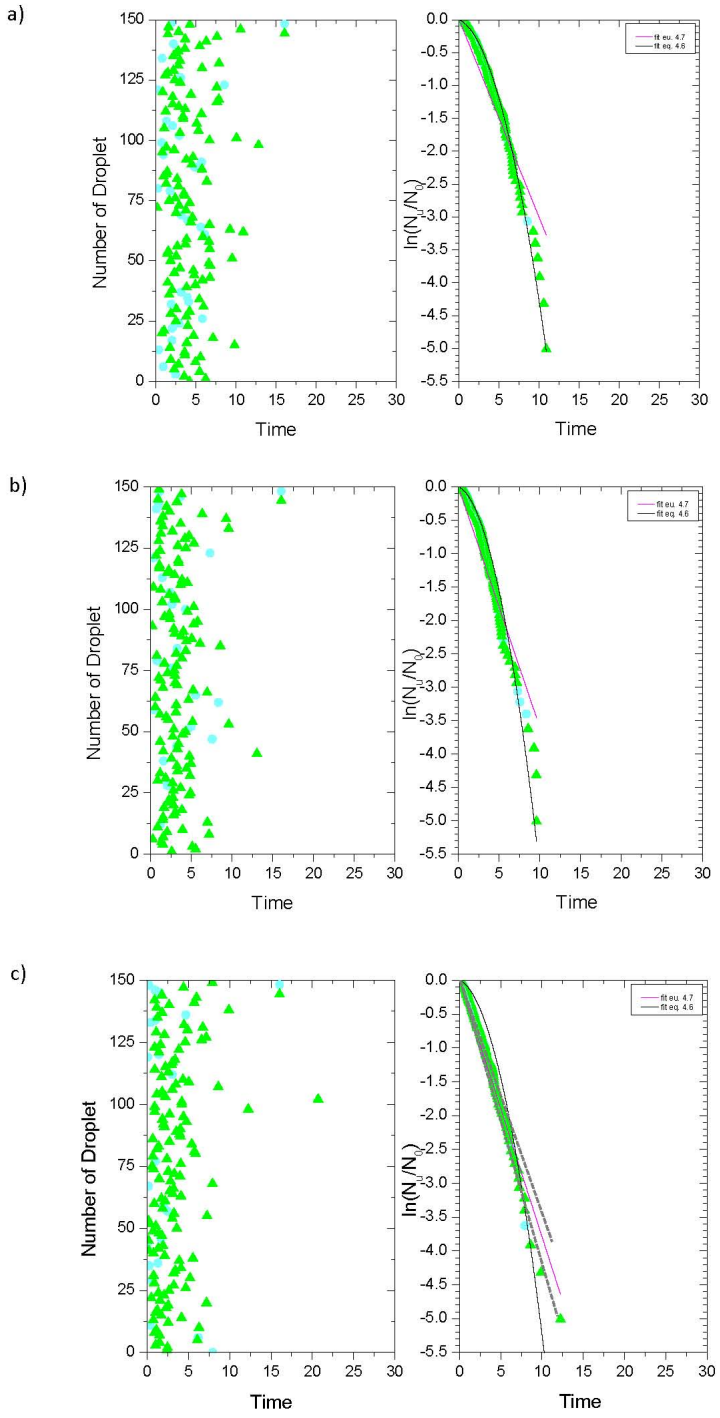

Figure 4.8: Simulation of an experiment with 150 droplets, a collision rate of $0.524\,\mathrm{s}^{-1}$, a contact freezing probability of 0.1, and an assumed immersion freezing rate per particle of a) $0.3\,\mathrm{m}^{-2}\mathrm{s}^{-1}$, b) $0.5\,\mathrm{m}^{-2}\mathrm{s}^{-1}$, and c) $0.7\,\mathrm{m}^{-2}\mathrm{s}^{-1}$, Freezing event due to contact mode (blue dots) or immersion mode (green triangles), gray dashed line: 10% variability of the slope

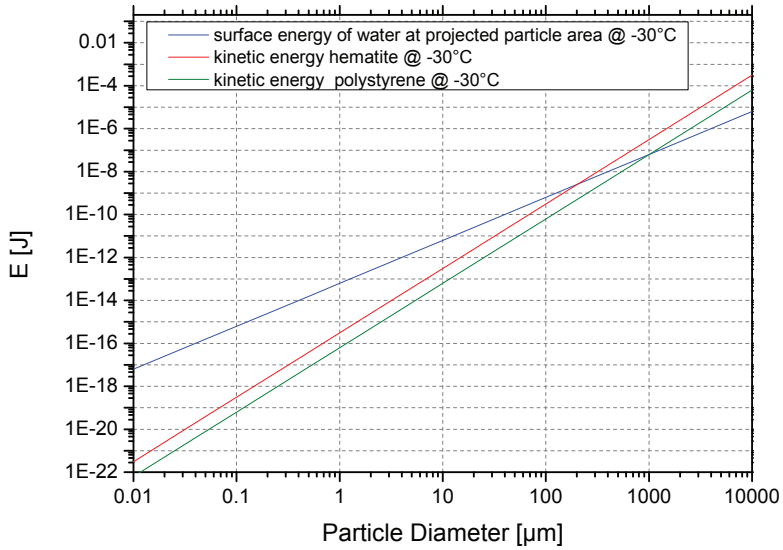

Figure 4.9: Surface energy of water at projected particle area (blue line) compared to the kinetic energy of a colliding hematite (red line) and polystyrene (green line) particle

than the droplet radius, which shows that it is unlikly that a particle penetrates the droplet surface during the experiment.

We do not know, at what time after the collision of a particle the freezing starts. So it is possible that water vapor of the evaporating droplet condense on the particle, or in some cases even freeze as discussed above. The current setup is not suitable to find out more about that and further research is necessary. In section 6.1 a possible setup will be discussed.

4.2 Calculation of the freezing probability and the particle's trajectories

To calculate the freezing probability on a single contact, for each experiment about 150 droplets are investigated and in the end a curve with the freeze time on the x-axis and the number of unfrozen droplets N_u divided by the number of all investigated droplets N_0 on the y-axis results – the so called "freezing curves". Since the contact freezing is described by equation 4.7, for the probability of freezing on a single contact follows:

$$e_c = \frac{m_{\mathrm{exp}}}{n_c} \tag{4.10}$$

Here is m_{exp} the slope of the linear fit to $\ln(N_u/N_0)$ as a function of t.

Equation 4.10 shows, the n_c is needed to calculate e_c. This value can not be measured directly in the experiment, and has to be calculated.

Let us have a look on the electrostatic forces first. The calculation is based on Kraemer and Johnstone [1955]. Considering the drag force and static Coulomb interaction, the collection efficiency η of charged particles of radius r_p and charge q_p in a laminar gas flow of velocity v_0 around a spherical, oppositely charged object with a radius r_d and charge q_d can be calculated by:

$$\eta = \frac{C(r_p) q_p q_d}{6\pi^2 \epsilon_0 \mu r_p r_d^2 v_0} \tag{4.11}$$

ϵ_0 describes the electrical permittivity, μ the dynamic viscosity of the carrier gas, and $C(r_p)$ the Cunningham slip correction factor [Allen and Raabe, 1985].

For the EDB experiments it is necessary to consider the induced dipole interaction between droplet and particle, which is especially strong at small distances. The force exerted by the spherical, charged droplet onto the aerosol particle is given by:

$$\mathbf{F} = -\left(\frac{\epsilon_{\mathrm{r}} - 1}{\epsilon_{\mathrm{r}} + 2}\right) \frac{d_{\mathrm{p}}^3 q_{\mathrm{d}}^2}{16\pi\epsilon_0 r_{\mathrm{dp}}^5} \cdot \mathbf{e}_{\mathrm{dp}} + \frac{q_{\mathrm{d}} q_{\mathrm{p}}}{4\pi\epsilon_0 r_{\mathrm{dp}}^2} \cdot \mathbf{e}_{\mathrm{dp}} + \frac{6\pi\mu r_{\mathrm{p}}}{C(r_p)} \cdot \mathbf{w} \tag{4.12}$$

The first term describes the force between the droplet charge (assumed being a point charge) and the image charge induced by the charged droplet on the particle at a distance r_{dp}. This force has a large effect at short distances. The second term describes the Coulomb attraction between the droplet charge and the particle charge. The third term describes the drag force on the particle moving relatively to the carrier gas with the relative velocity $\mathbf{w} = \mathbf{u} - \mathbf{v}$ with the velocity of the carrier gas ($\mathbf{u}$) and the particle ($\mathbf{v}$), respectively. In Kraemer and Johnstone [1955] two additional terms are considered, one term describing the repulsion of the surrounding aerosol particles, and one describing the image charge of the particle in the droplet. Since

most particles are single charged, and the droplet charge is much stronger, this effect can be neglected.

The thermophoretic force results from the temperature gradient between droplet surface and the surrounding gas [Davis and Schweiger, 2002]. Since the momentum of the gas molecules on the warmer side of the particle is higher than the momentum of the molecules on the colder side (droplet surface is colder than EDB), the thermophoresis causes a motion from the warmer to the colder region. Grover et al. [1977] give the thermophoretic force F_{th} as

$$F_{\mathrm{th}} = -\frac{12\pi r_p \eta_{\mathrm{air}}(k_{\mathrm{air}} + 2.5 k_p \,\mathrm{Kn}_p)}{5(1+3Kn_p)(k_p + 2k_{\mathrm{air}} + 5k_p \,\mathrm{Kn}_p)p} k_{\mathrm{air}} \nabla T \tag{4.13}$$

r_p is the radius of the particle, and k_{air} and k_p the thermal conductivity of air and the aerosol particle, respectively. p is the air pressure, η_{air} is the dynamic viscosity of air and Kn_p is the Knudsen number of the aerosol particle in laminar flow condition. ∇T describes the local temperature gradient around the droplet at a large distance from the aerosol particle.

Diffusiophoretic force is caused by the water vapor concentration gradient in the surrounding gas [Davis and Schweiger, 2002]. According to Grover et al. [1977], the diffusiophoretic force F_{dif} is given by

$$F_{\mathrm{dif}} = -6\pi r_p \eta_{\mathrm{air}}(1 + \sigma_{va} x_a) \frac{D_v M_{\mathrm{air}}}{M_w \rho_{\mathrm{air}}} \nabla \rho_v \tag{4.14}$$

Schmitt [1961] gives an empirical value of -0.26 for σ_{va}, so that $(1 + \sigma_{va}) = 0.74$ for $x_v \ll x_a$. Water vapor and air are considered ideal gases, and x_v and x_a are the partial pressures of water vapor and dry air. D_v describes the diffusivity of water vapor in air, ρ_{air} is the density of air, and M_{air} and M_w are the molar weight of air and water, respectively. $\nabla \rho_v$ describes the local gradient of the water vapor density ρ_v.

The modeling software COMSOL Multiphysics® has been used to simulate the corresponding temperature field around the droplet considering a flow from below [Duft, 2013]. With this information the corresponding relative humidity to each location around the droplet can be calculated (figure 5.3), and the influence of the thermophoresis and diffusiophoresis on the particle's trajectory can be taken into account to calculate the collision rate.

Figure 4.11 shows the thermophoretic force, diffusiophoretic force, coulomb attraction force, and the induced dipole interaction between droplet and aerosol particle for a hematite particle with a diameter of 970 nm and a kaolinite particle with a diameter of 550 nm, respectively. The assumed EDB temperature T_∞ was 240 K, the dew point temperature of the gas T_{dew} was $-40\,^{\circ}\mathrm{C}$, and the temperature at the droplet's surface T_d was 239.5 K. The electrostatic forces are two to three orders of magnitude stronger than the phoretic forces, where the diffusiophoreses works in the direction

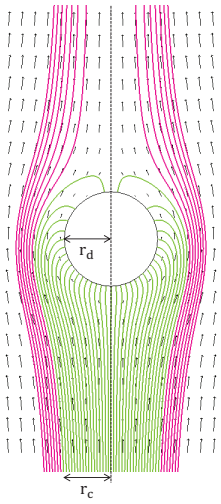

Figure 4.10: Trajectories of the particles around the droplet in the EDB. The black arrows represent the stationary flow field around the droplet. Trajectories which lead to a collision (green) and do not lead to a collision (red trajectories)

away from the droplet and thus against the other three forces. But the net force acting on the particle accelerates it toward the droplet.

Figure 4.12 shows the influence of the phoretic forces on the collection efficiency for a kaolinite particle with a diameter of 550 nm. Panel 4.12a) shows the collection efficiency for $T_\infty = 240\,\mathrm{K}$, $T_{\mathrm{dew}} = -37\,^\circ\mathrm{C}$, and $T_d = 239.5\,\mathrm{K}$ calculated with and without phoretic forces. The phoretic forces cause a change in the third decimal place of the collection efficiency, which changes the fourth decimal place of the collision rate, so the influence is not negligible but very small. Panel 4.12b) shows the collection efficiency for $T_\infty = 255\,\mathrm{K}$, $T_{\mathrm{dew}} = -37\,^\circ\mathrm{C}$, and $T_d = 250\,\mathrm{K}$, which is an unrealistic high difference between the surface temperature and the EDB temperature. Even in this case the change in phoretic forces change the collection efficiency in the second decimal place, which causes a change in the third decimal place of the collision rate.

The equation of motion resulting from all these forces leads to the trajectories of the particles. The differential equations can be solved numerically by using the Runge Kutta 4th order method (described in e.g. Hairer et al. [2009]).

The particle trajectories are shown in figure 4.10. The calculation started at a distance of 19 times of the droplet radius r_d. The black arrows indicate the stationary flow field around the droplet. The green trajectories show the trajectories of particles, which are collected by the droplet. The boundary trajectory is being used to calculate the collision rate. The distance between the center line and the start of the boundary

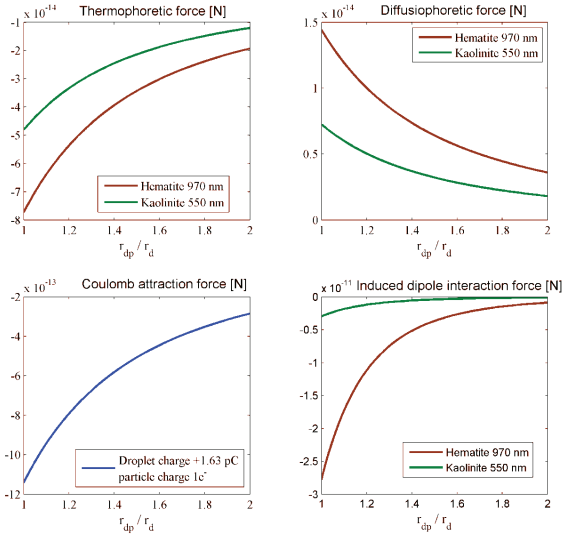

Figure 4.11: a) Comparison of phoretic and electrostatic forces between a droplet and a particle in air. $r_d = 90\,\mu\text{m}$ gives the diameter of the droplet and r_{dp} the distance between the droplet center and the aerosol particle. The particle diameter is 970 nm for hematite and 550 nm for kaolinite. The diffusiophoretic force is directed away form the droplet, the other forces are directed towards the droplet. $T_\infty = 240\,\text{K}$, $T_d = 239.5\,\text{K}$, $\varepsilon_r = 2$, $k_p = 0.5$ and $T_{dew} = -40\,°\text{C}$ (adapted from Discussion of [Hoffmann et al., 2013a])

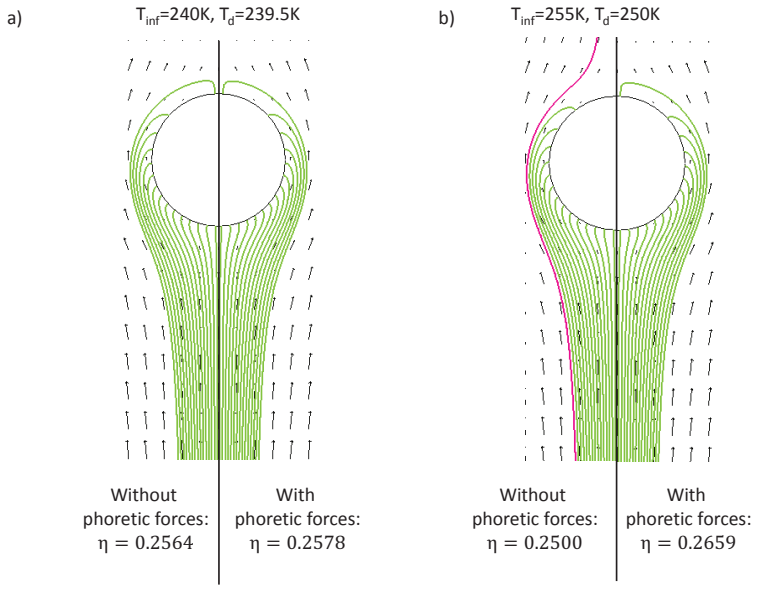

Figure 4.12: Comparison of collection efficiency η with and without phoretic forces

trajectory defines the collision distance r_c. The collection efficiency η, is given by

$$\eta = \frac{\pi r_c^2}{\pi (r_d + r_p)^2} \tag{4.15}$$

with the particle radius r_p. Knowing the number concentration of the aerosol particles as well as the volume flow rate v_s of aerosol through the EDB, the collision rate can be calculated by:

$$n_c = \pi r_d^2 \cdot N_c \cdot v_s \cdot \eta, \tag{4.16}$$

Figure 4.13 shows the collection efficiency as a function of particle size and charge. The charge of a particle has a significant influence on the collection efficiency for particles sizes measured in these experiments.

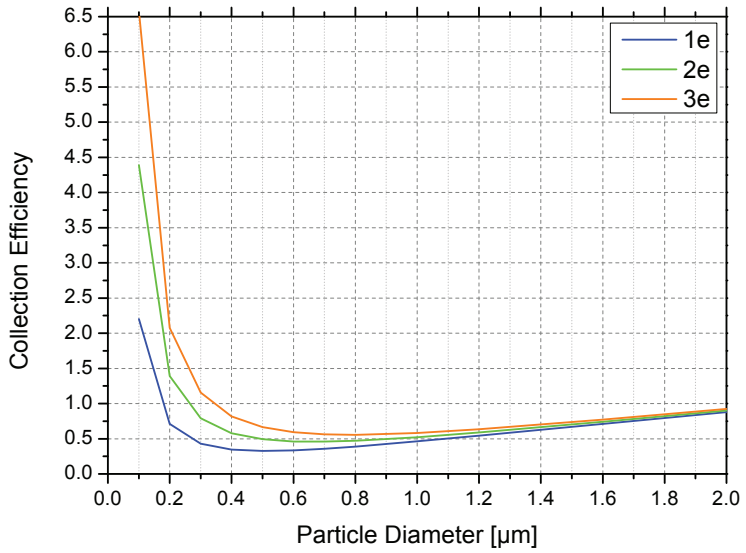

Figure 4.13: Collection efficiency as function of particle size and charge

4.3 Experimental verification of the collection efficiency

To verify the calculated collection efficiency, droplets are ejected onto a silicon wafer (2 mm×2 mm) (figure 4.14) and the residuals are analyzed by SEM. The droplet can collect particles for a certain period of time, and then the particles are separated out by an electrostatic precipitator. Next, a metal rod with the silicon wafer glued to its

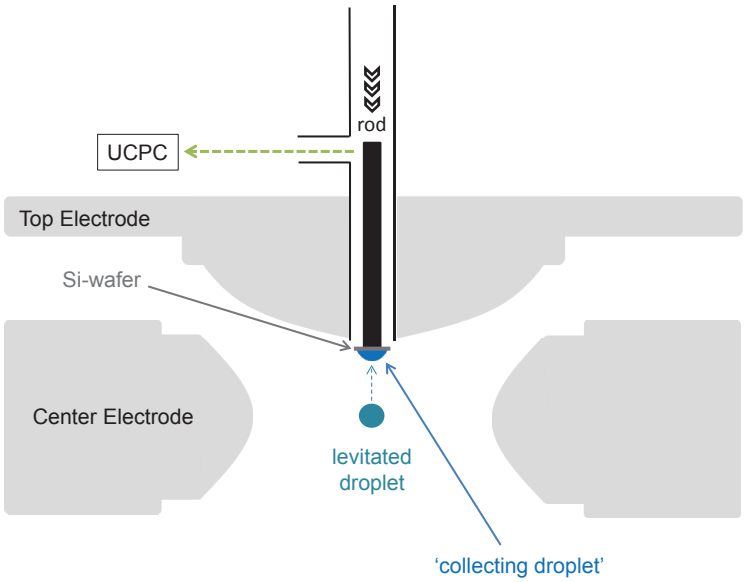

Figure 4.14: Schematic diagram of the ejection of a levitated droplet onto a Si-wafer

top is lowered to the center of the EDB. Once the wafer is in position, the automatic height control is switched off and the droplet is moved in the direction of the wafer by changing the DC voltage. When the droplet touches the silicon wafer, the wafer is removed, and the droplet evaporates. If the droplet is frozen, it is necessary to place a liquid "collecting droplet" onto the Si-wafer before ejecting it, to prevent the frozen droplet from bouncing off the wafer.

4.4 Uncertainty analysis

The experiment has a number of error sources that are discussed in this section. Many of the sources have already been discussed in my diploma thesis [Hoffmann, 2012] but there have been some improvements in the mean time.

Temperature measurements in the EDB

The Pt-100 class B sensors being used have an uncertainty of $0.3°C + 0.005 \cdot T_{EDB}[°C]$ according to DIN EN 60751. In the temperature range of the experiments an uncertainty of $\pm 0.5\,°C$ exist. To reduce this uncertainty, we calibrated the sensors. Therefor a calibrated sensor and the new sensors have been plunged into a cryostat bath, stucking between two copper blocks. In total, an uncertainty of $0.2\,°C$ of the measured temperature is realistic.

Velocity of the aerosol flow

As described in section 3.3, the linear velocity of the gas flow depends on the temperature. The uncertainty of the temperature causes a small uncertainty in the gas velocity. Since it is not possible to measure the velocity directly in the experiment, it has to be simulated as described in section 3.3. The uncertainty of the flow rate, the pump of the UCPC is generating is given as $0.3 \pm 0.015\,\mathrm{l/min}$ [TSI, 2007]. This cause an uncertainty of 0.005% of the gas velocity. In total, I assume an uncertainty of 1% for the gas velocity.

Droplet size and charge

The uncertainty of the droplet size is mostly caused by the calculation of the observation angle (see section 3.4). The uncertainty of the temperature dependent refraction index of air and water is negligible. The diameter of the aperture used to determine the observation angle is analyzed under a microscope, and the reading error causes an uncertainty of the observation angle of $0.22\,^{\circ}$. The resulting uncertainty of the droplet diameter is 4%.

The droplet charge is calculated through a balance of forces shown in equation 3.1. For the calculation, the applied voltage on the bottom and top electrodes and the velocity of the gas flow is relevant. The variation of the voltage is in the range of $\pm 1\,\mathrm{V}$. The error for the droplet charge is in total about 5%.

Particle size, charge and number concentration

It is difficult to estimate an error for the particle size, because of the aspherical shape of some of the aerosol materials. To get more information about the particle size, a filter sample is prepared for each aerosol material and each mobility diameter being used for experiments. The area equivalent diameter of the particles are analyzed by SEM to get information about the size distribution and amount of multiple charged particles, as described in section 3.6.

The size distributions of the aerosols are shown in figure 4.15 and appendix D.1. The "worst" aerosol material to size select in this work were the cellulose particles, because of their very irregular shapes (figure 3.11). The "best" material to size select was hematite, because these particles are grown monodisperse in the first place, and only agglomerates carrying multiple charges cause an uncertainty. Illite NX is also easy to size select, but feldspar particles are much more aspherical. The size dependence of the collection efficiency (figure 4.13), introduces an uncertainty in the calculated collection efficiency. This affects also the accuracy of the collision rate, and thus the calculated freezing probability.

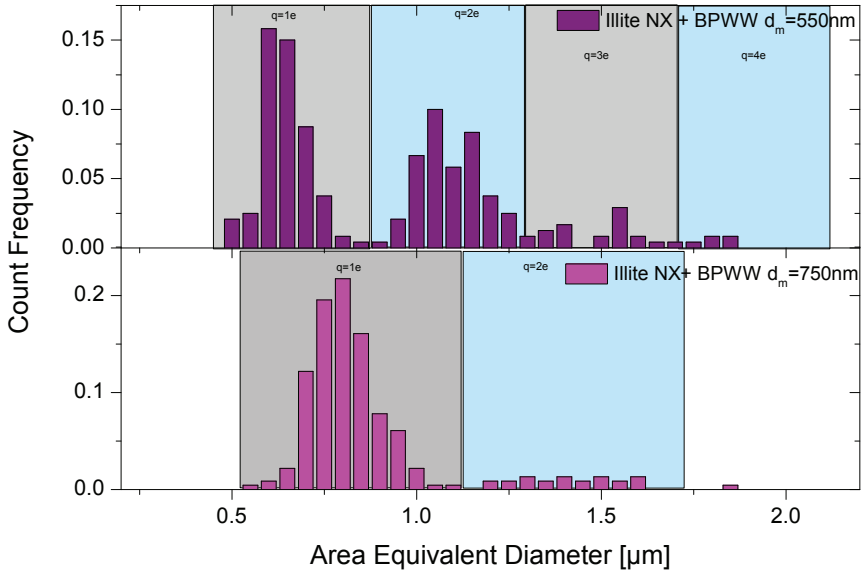

Figure 4.15: Size distribution of illite mixed with BPWW with a mobility diameter of 550 nm and 750 nm, respectively. The colored areas give the number of elementary charges

The particle charge is distributed according to the Fuchs distribution [Fuchs, 1963] (explained in detail in section 3.6). To calculate the freezing probability, only single charged particles are considered. The fraction of freezing events caused by multiple charged larger particles are subtract out using equation 4.17.

If multiple charged particles are present in the size distribution of the particles, the collision rate of the multiple charged particles has to be considered in the calculation of freezing probability for the size of single charged particles $e_{c_{1e}}$:

$$e_{c_{1e}} = \frac{m_{\text{exp}} - (n_{c_{2e}} \cdot e_{c_{2e}} + n_{c_{3e}} \cdot e_{c_{3e}} + ...)}{n_{c_{1e}}} \tag{4.17}$$

The freezing probability for the size of multiple charged particles can be taken from previous experiments. In these experiments usually double charged particles have to be considered, in exceptional cases triple charged particles. Figure 4.15 shows exemplary size distributions of illite mixed with BPWW. For the size distribution of the other aerosol material see appendix D.1.

The particle number concentration is analyzed by an UCPC from TSI [TSI, 2007]. The vendor gives an accuracy of $\Delta N_p = \pm 10\%$. During an experiment, the concentration of particles generated by a fluidized bed generator can variate a lot. Because of that, the experiment is split into several sections where the particle concentration is stable, so that no additional uncertainty for the particle concentration has to be considered.

Slope of the freezing curve

Running an experiment multiple times with identical parameters can result in different slopes of the freezing curves. The simulation freezing curves with 100 frozen droplets gives a variance of the slope of about 10%. Smaller numbers of investigated droplets would increase the variation.

Entire error of the freezing probability

To estimate the entire error of the freezing probability, error of the collection efficiency, the particle concentration, and the uncertainty of the slope of the freezing curve have to be considered. As a upper estimation, the maximal error of the experimental collection efficiency of 0.3 shown in figure 5.5 have been used. The error can be calculated by:

$$\Delta e_c \leq \sqrt{(\Delta\eta)^2 + (\Delta N_p)^2 + (\Delta m)^2} = \sqrt{0.3^2 + 0.1^2 + 0.1^2} = 0.33 \tag{4.18}$$

Considering all the error sources mentioned above, the sensitivity analysis gives an uncertainty for the freezing probability of 35% in total.

5 Results and discussion

In this chapter the possibility of deposition freezing in the experiment and the verification of the collection efficiency are discussed. Furthermore, the results of the contact and immersion freezing experiments are presented and compared with results of other research groups.

5.1 Possibility of deposition freezing in the experiment

Since the droplet evaporates during the experiment time of 30 s, a water-saturated area around the droplet exists, and so does a supersaturated area with respect to ice. It is also possible that an aerosol particle on its way through the supersaturated area around the droplet act as INP in the deposition mode and have an ice nucleus on its surface at the moment of contact (figure 5.1). Such a particle would initialize freezing immediately with $e_c = 1$.

The feasibility of this scenario can be evaluated by comparing the contact freezing results with some deposition freezing results obtained by other research groups.

As an example, the results of the experiments with the Zurich Ice Nucleation Chamber (ZINC) (Welti et al. [2009], Stetzer et al. [2008]) are easy to compare, because they also used size selected aerosol particles to perform their experiments. Welti et al. [2009] used e.g. illite NX and kaolinite Fluka particles, and give the activated fraction (fraction of particles which was activated to ice) for a certain particle size, temperature, and relative humidity over ice (RH_{ice}). The nucleation rate coefficient for deposition freezing j_{dep} can be calculated from:

$$1 - f_{ice} = 1 - \frac{N_f}{N_0} = \exp(-j_{dep} \cdot S_{INP} \cdot t_{exp}). \tag{5.1}$$

The probability of deposition freezing in the EDB experiment P_{EDB}^{dep} is described by:

$$P_{EDB}^{dep} = -(\exp(-j_{dep} \cdot S_{INP} \cdot t_{EDB}) - 1) \tag{5.2}$$

Figure 5.2 shows the results for experiments with illite NX and kaolinite Fluka from Welti et al. [2009], and K-feldspar from Zimmermann et al. [2008].

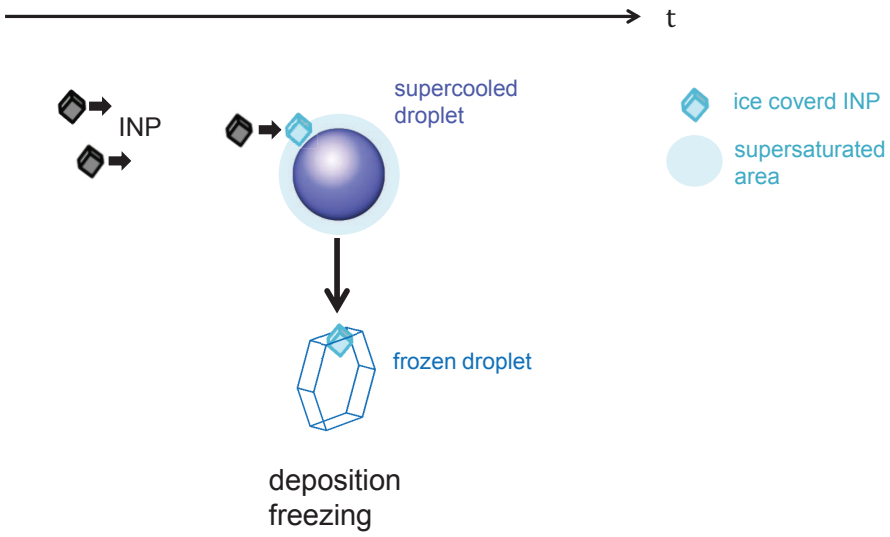

Figure 5.1: Sketch of deposition-facilitated freezing

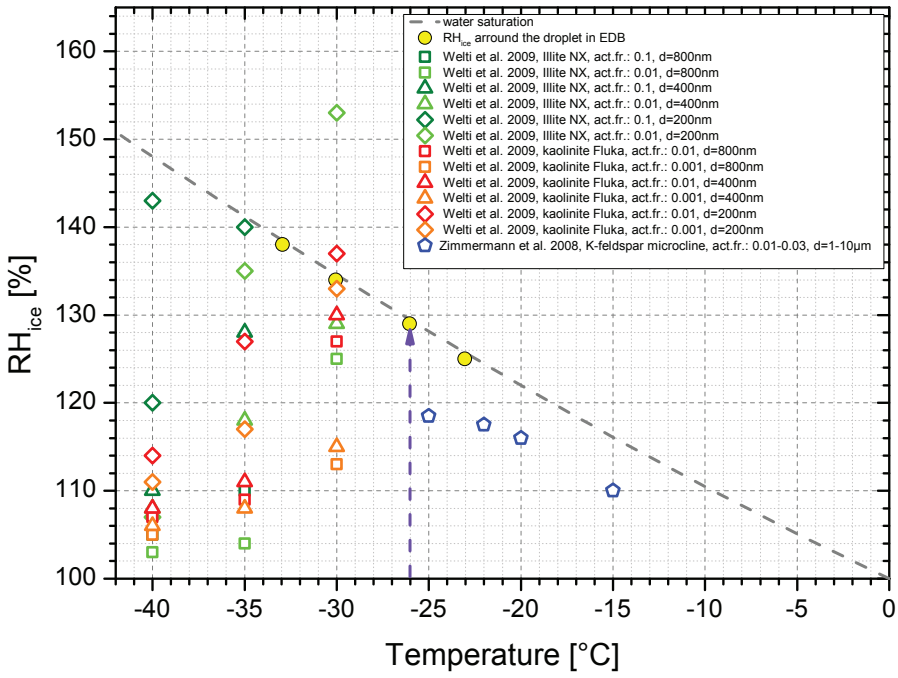

Figure 5.2: Comparison of deposition freezing results of Welti et al. [2009] and Zimmermann et al. [2008], and the condition in the EDB. The purple dashed line shows the phase trajectory of a particle on its way to the droplet, corresponding to one of the trajectories in figure 5.3.

The gray dashed line in figure 5.2 represents the water saturation as a function of temperature, the condition directly above the droplet surface.

The time of particle residence within the ice-supersaturated environment is needed to calculate the probability of deposition ice nucleation and thus the probability of "deposition-nucleation-induced" contact freezing (see eq. 5.2). The residence time of the particles in the ZINC experiments is 12 s. Figure 5.3 shows the trajectories of particles around a levitated droplet (calculated for $T_\infty = 243\,\mathrm{K}$, $T_d = 242\,\mathrm{K}$, $T_\mathrm{dew} = 236\,\mathrm{K}$, $q_\mathrm{d} = 1.5\,\mathrm{pC}$, and $d_p = 550\,\mathrm{nm}$). The color code gives the relative humidity with respect to ice along the trajectories (cf. section 4.2). As a minimum particle velocity we assumed the minimum gas velocity in these experiments, which is about 0.47 m/s. The maximum path of a particle in the supersaturated area is assumed as 200 µm. This gives a maximum residence time in the supersaturated area in the range of about 0.5 ms – unless the particles would deposit onto the droplet surface without initializing freezing. In that case the particles have a residence time up to 30 s. Then however, the largest of the two heterogeneous freezing rate coefficients, immersion and deposition, have to be used to estimate the probability of ice nucleation after waiting the time t. The maximum $\mathrm{RH_{ice}}$ on droplet surface is 138 %.

Welti et al. [2009] gives an activation fraction of 1 % for illite particles with a diameter of 800 nm at a temperature of −30 °C and $\mathrm{RH_{ice}} = 125\,\%$. At this temperature we measured a freezing probability of 10% for 550 nm particles and 20% for 750 nm particles. The nucleation rate coefficient j_dep calculated from the data of Welti et al. [2009] is $4.2 \cdot 10^8\,\mathrm{m^{-2}s^{-1}}$. $P_\mathrm{EDB}^\mathrm{dep}$ would be $4.5 \cdot 10^{-5}\,\%$ after 0.5 ms and 2.5 % after 30 s. For kaolinite Fluka, the situation is similar to illite.

In the experiments of Zimmermann et al. [2007] the observation time was between 5 and 10 min. The K-feldspar particles in the experiments of Zimmermann et al. [2008] were not size selected, but the particles were not larger than 10 µm. For these relatively large particles the activated fraction was between 1% and 3% at the given temperature and $\mathrm{RH_{ice}}$. The lowest temperature they measured was −25 °C.

K-feldspar can be activated already at −15 °C for particles with a diameter between 1 µm and 10 µm [Zimmermann et al., 2008]. The activated fraction is between 1% and 3% at a temperature between −15 °C and −25 °C and a given $\mathrm{RH_{ice}}$. At −22 °C the contact freezing probability measured in this work is already 10% for particles with a mobility diameter of 550 nm. This shows that for K-feldspar the freezing is probably not initialized due to deposition mode.

For the activation temperature of K-feldspar given by Zimmermann et al. [2008], and assuming a particle diameter of 10 µm, an activation fraction of 3% and a time of 5 min, j_dep was found to be equal to $3.2 \cdot 10^5\,\mathrm{m^{-2}s^{-1}}$. The probability of deposition freezing in EDB measurements is 0.3% for a residence time of 30 s. This shows that deposition freezing is unlikely in the measurements of this work.

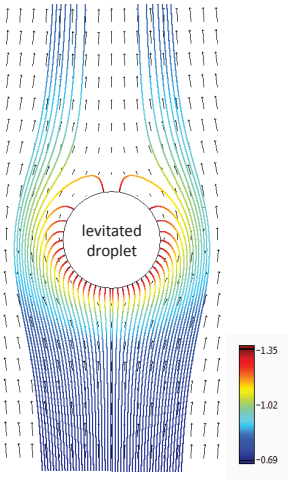

Figure 5.3: Calculated trajectories of the particles around a levitated droplet in the EDB. The black arrows represent the stationary flow field around the droplet. Color code shows the relative humidity with respect to ice (RH_{ice}) along the particle's trajectories around a levitated droplet (courtesy of Duft [2013]). Calculated for $T_\infty = 243\,\mathrm{K}$, $T_d = 242\,\mathrm{K}$, $T_{\mathrm{dew}} = 236\,\mathrm{K}$, $q_\mathrm{d} = 1.5\,\mathrm{pC}$, and $d_p = 550\,\mathrm{nm}$.

5.2 Experimental verification of collection efficiency

Figure 5.4 shows two examples of ejected droplets. On the left, the droplet has collected hematite particles of 900 nm. The blue circle marks the boundary of evaporated droplet on the Si-wafer. Hematite particles are very easy to identify under the microscope because of their high contrast and cubic shape. It is more difficult to count clay mineral particles on the Si-wafer. To make it a bit easier, we mixed polystyrene latex particles (PSL) ($d_m = 200\,\mathrm{nm}$) into the deionized water and injected this suspension into the EDB to collect the mineral particles. The picture on the right in figure 5.4 shows collected illite NX particles ($d_m = 750\,\mathrm{nm}$) and the PSL particles left on the Si-wafer after evaporation of the droplet.

Figure 5.5 shows the comparison of calculated and observed collection efficiency. For the spherical PSL particles and the almost spherical hematite particles the experimental collection efficiency is a little too low, and, in contrast, for the mineral dust particles, it is a bit too high. The details of the single experiments are shown in table 5.1. The spherical, monodisperse PSL particles and the cubic hematite particles, produce better results than the non-spherical mineral dust particles with a significant number of larger, double-charged particles. The error of the theoretical collection efficiency was calculated considering the errors of the droplet diameter, gas velocity, droplet charge and temperature described in section 4.4, and the error of the experimental collection efficiency is given by the standard deviation.

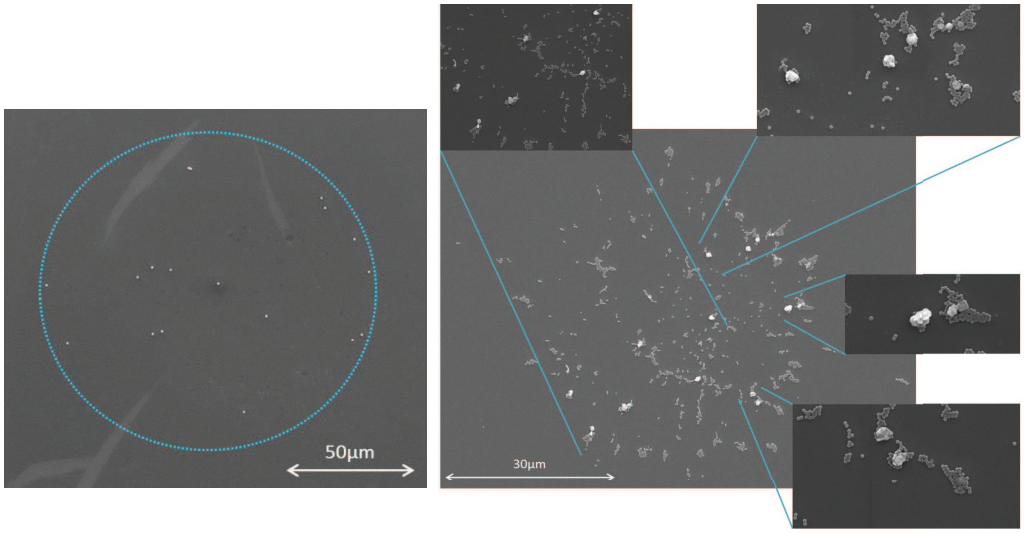

Figure 5.4: Hematite particles (side length: 800 nm) left on the substrate after evaporation of the droplet (blue dotted line marks the boundary) (left) Illite NX particles (d_m = 750 nm) in a PSL (d_m = 200 nm) suspension (right). Images obtained with SEM.

Table 5.1: Comparison of theoretical and experimental collection efficiency for PSL microspheres, hematite, illite NX and kaolinite mobility selected by DMA

Aerosol material	Mobility diameter DMA [nm]	Droplet diameter [µm]	Number of investigated droplets	Calculated collection efficiency	Experimental collection efficiency
PSL	440	85.7±1.7	7	0.32±0.04	0.17±0.16
PSL	720	85.7±1.7	6	0.31±0.04	0.18±0.10
PSL	720	71.7±1.4	10	0.54±0.08	0.44±0.21
PSL	720	69.0±1.4	8	0.54±0.08	0.45±0.15
hematite	970	80.6±1.6	13	0.80±0.11	0.81±0.15
illite NX	750	81.9±1.6	8	0.53±0.07	0.64±0.15
kaol. KGa-1b	550	77.1±1.5	4	0.57±0.08	0.76±0.24

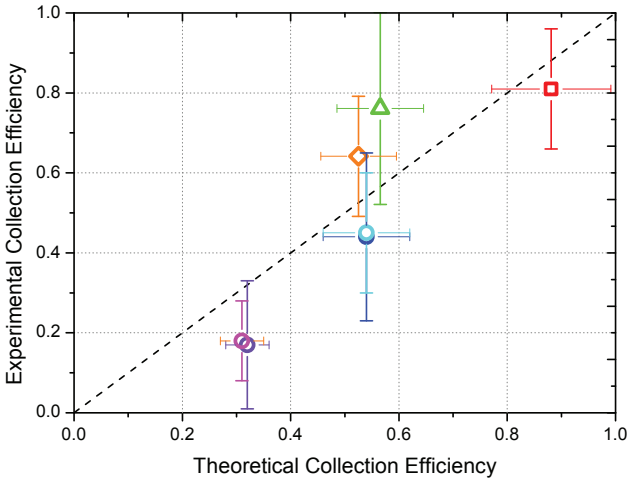

Figure 5.5: Collection efficiency of Hematite $d_m = 970\,\text{nm}$ (red), Kaolinite KGa-1b $d_m = 550\,\text{nm}$ (green), Illite NX $d_m = 750\,\text{nm}$ (orange), PSL $d_m = 720\,\text{nm}$ (magenta, dark and light blue) and PSL $d_m = 440\,\text{nm}$ (purple) (compare table 5.1)

5.3 Measurements of the contact freezing probabilities

The contact freezing probability e_c for all investigated aerosol materials have been found to show a temperature, size and material dependency. The accuracy of e_c determination is limited by two factors: 1) the temperature range below the homogeneous freezing limit is not accessible (in this experiment at about $-35\,°C$), and 2) the sufficient number of freezing events (at least 100 freezing events). The stability of aerosol generation limits the number of droplets to approximately 400, so at least 25% of the investigated droplets have to freeze to get a representative result. The number of freezing events is constrained by the ice activity and the number concentration of the particles. For some types of aerosol it was possible to generate several hundred particles per cubic centimeter, whereas for other materials it was possible to generate only $30\,cm^{-3}$ – $40\,cm^{-3}$, so that the droplet experienced only one collision during its 30 s residence time in the EDB on average.

5.3.1 Mineral dust particles

The results of contact freezing experiments with mineral dust are summarized in figure 5.7 and 5.8. In all panels of figure 5.7 and 5.8 feldspar is shown for reference.

Figure 5.7a shows the comparison of two different types of kaolinite and feldspar microcline ([Hoffmann, 2012], Hoffmann et al. [2013a]). The e_c measured for both kaolinites is a function of size and temperature. Kaolinite Fluka is more ice active than kaolinite KGa-1b. The particles of both kaolinite have different shapes, kaolinite Fluka is not as pure as KGa-1b and have additional components like feldspar. Additionally, kaolinite Fluka have a broader size distribution (figure D.3). It is not clear yet, why kaolinite Fluka is more ice active than KGa-1b, but one or a combination of all mentioned factors could have been the reason for this behavior.

The feldspar particles are much more ice active than both kaolinite types. Feldspar also shows a size and temperature dependency, but the temperature dependency is not linear, as in case of kaolinites. Because of the high ice activity, the 550 nm particles already reach a freezing probability of one at a temperature of about $-26\,°C$. The e_c of the 550 nm particles reaching values slightly above one, could be an artifact caused by the aspheric shape of the particles or due to an uncertainty of the evaluation of multiple charges. The smaller particles reach a plateau at a temperature of about $-29\,°C$ at a freezing probability of about 70%, which means that only 70% of the particles have been able to initialize freezing, which is an unusual behavior for a mineral dust particle. This behavior has been observed in the experiments with SNOMAX® particles. Not every particle carries an ice active protein complex (cf. section 5.3.2), but for the surface of a mineral the explanation is not clear.

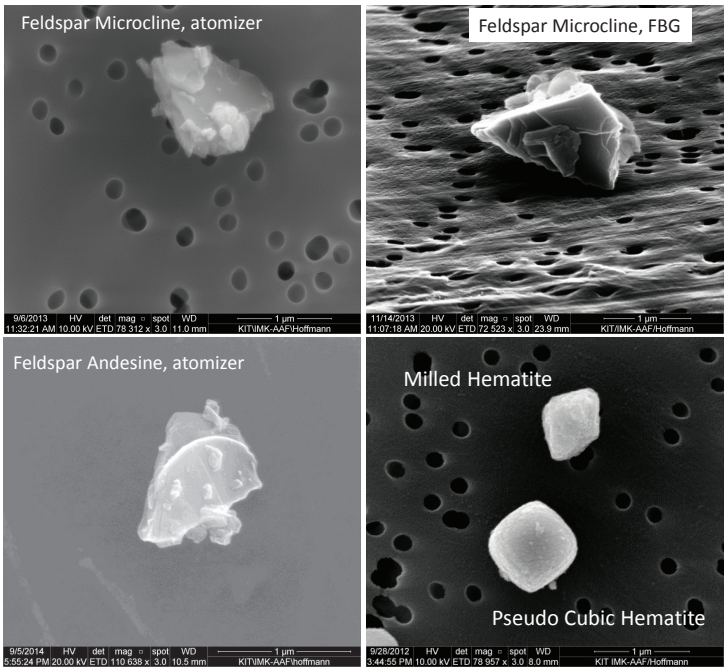

Figure 5.6: SEM images of Potassium rich feldspar (microcline) generated with an atomizer and a fluidized bed generator; sodium rich feldspar with calcium content (andesine) generated with an atomizer; pseudo cubic and milled hematite

Figure 5.7b) shows the results of illite NX and hematite compared with the feldspar results. Because of the almost spherical shape of the illite particles (figure 5.9) it is possible to select the mobility sizes of these particles with a quite narrow distribution. The investigation of 4 different mobility diameters (150 nm, 320 nm, 550 nm, and 750 nm) was possible [Hoffmann et al., 2013b]. The sizes have been chosen in such a way, that the correction of double and triple charged particles was possible. All particle sizes show a linear temperature dependency.

The hematite particles with the pseudo cubic shape (figure 5.6) had a mobility diameter of 300 nm and 970 nm, respectively [Hoffmann et al., 2013a]. To investigate the influence of the particle surface, a 970 nm sample was milled with bronze beads, and a mobility diameter of 620 nm was selected (figure 5.6). Hematite is an inefficient ice nucleating particle (INP), it initializes freezing only at temperatures close to the homogeneous freezing limit. We saw a difference of e_c of the cubic hematite particles of two different sizes, but the freezing probability of the milled hematite shows no significant increase in the ice activity, as seen by Hiranuma et al. [2014b] for the immersion mode. The authors saw an increase in the INAS density of about an order of magnitude. In difference to the contact freezing experiments, Hiranuma et al. [2014b] investigated the entire size range of the milled particles. As mentioned before, only a narrow temperature range close to the homogeneous freezing limit

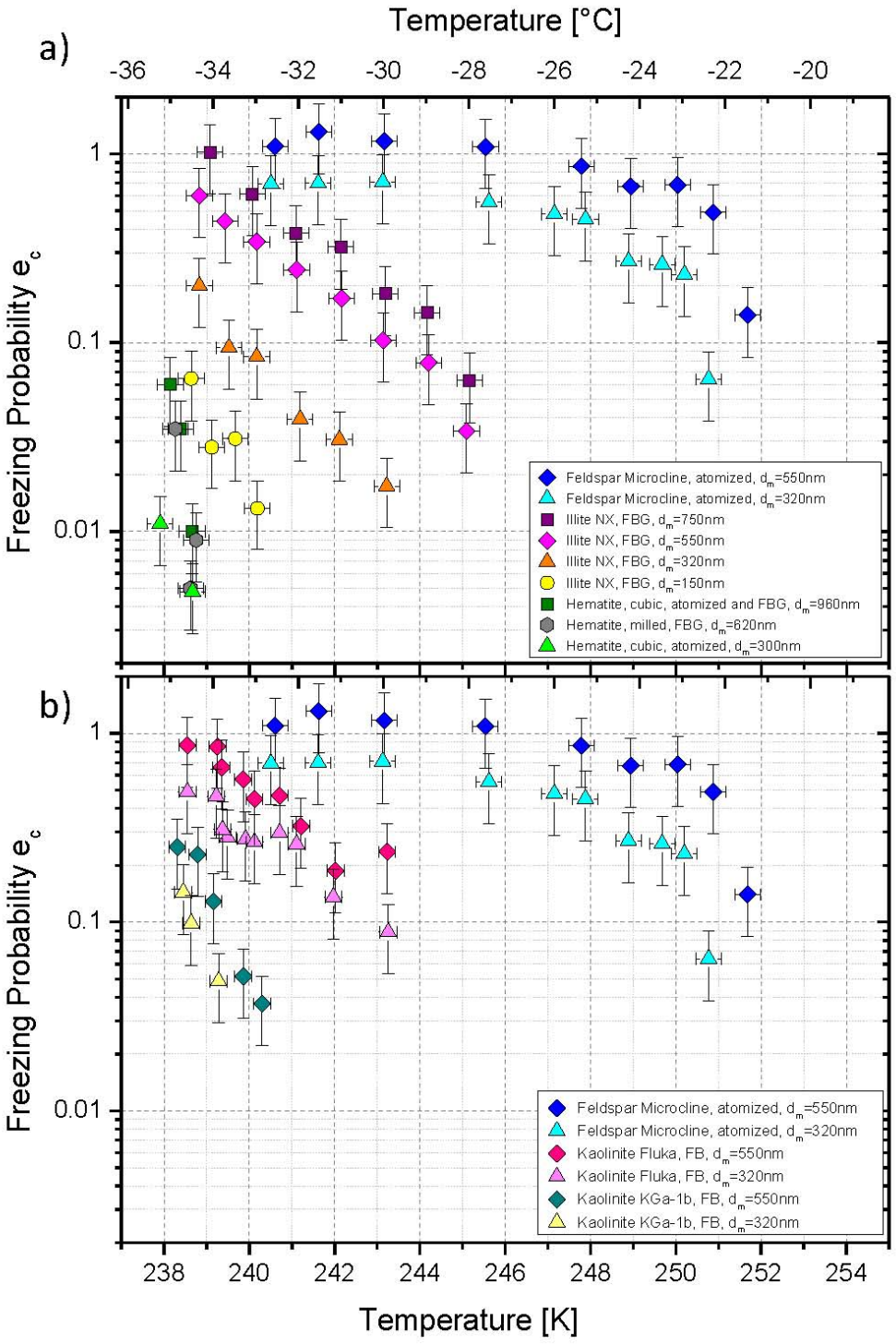

Figure 5.7: Overview of contact freezing experiments with mineral dust particles. a) feldspar microcline compared with illite NX and hematite, b) feldspar microcline compared with two different types of kaolinite (Fluka and KGa-1b)

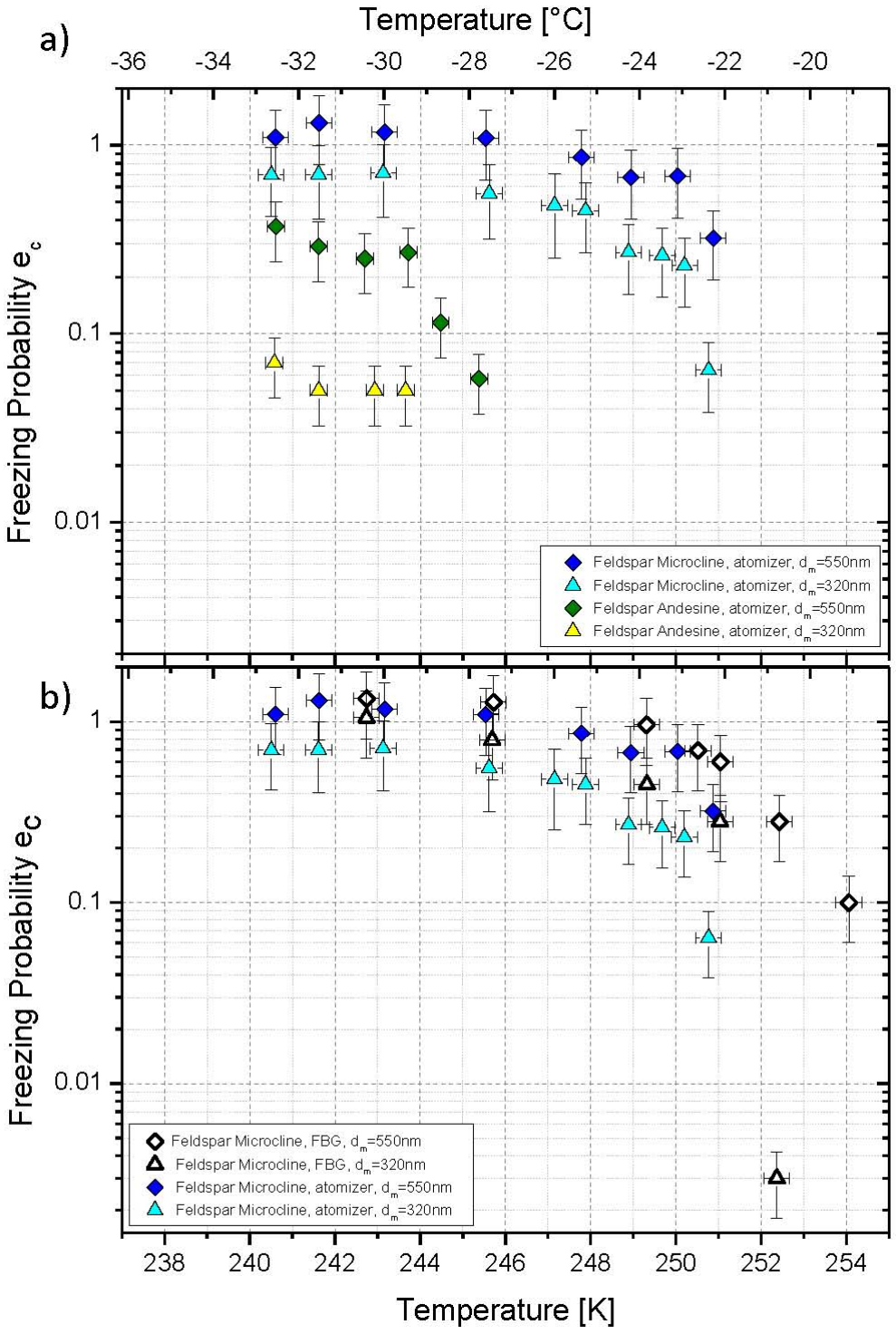

Figure 5.8: Overview of contact freezing experiments with mineral dust particles. a) Comparison of two different types of feldspar, b) Comparison of feldspar microcline generated with an atomizer and a fluidized bed generator (FBG)

could be investigated in the contact freezing experiments, and that makes it difficult to identify an influence of the freshly introduced surfaces anyway. Hiranuma et al. [2014b] gives a BET surface area of $2.2\,\mathrm{m}^{-2}\mathrm{g}^{-1}$ for cubic hematite, and $3.7\,\mathrm{m}^{-2}\mathrm{g}^{-1}$ for milled hematite, so the BET surface area of milled hematite is larger, but has no effect on e_c.

Figure 5.8a) shows the results of two different feldspars. One is potassium rich (K-)feldspar (microcline) and the other one is a sodium rich feldspar with calcium content (andesine). The mobility diameters 550 nm and 320 nm were measured. Andesine is much less ice active than microcline. Andesine feldspars seem to have two different ice active regimes. For particles with a mobility diameter of 550 nm a change in the slope of the temperature dependency at −31 °C is present. For lower temperatures the slope is less steep. For the particles with a mobility diameter of 320 nm it was not possible to investigate temperatures higher than −31 °C, because of the experimental limitations explained at the beginning of this chapter. The shape of the temperature dependency looks similar to the shape for the larger particles, just at lower values. Na/Ca-feldspar is less ice active than K-feldspar, but the e_c of both feldspars show no linear temperature dependency, like the other mineral dusts.

Visually, there is no difference in the shape of the particles of both feldspars (figure 5.6). K-feldspar being more ice active than Na/Ca-feldspar must be connected to the different chemical compositions.

To verify, whether there is an influence in case the particles are generated from a suspension or from a powder, experiments with both generation techniques were done for K-feldspar (figure 5.8b). It seems that the dry generated particles are slightly more ice active than the particles from a suspension. The size distribution of the particles generated with a FBG is a bit broader than the size distribution of the particles generated with an atomizer (figure 5.19), but that was taken into account in the calculation of the freezing probability. Being able to do measurements at higher temperatures with the dry particles is caused by the fact, that the particle concentration was higher when using a FBG. Visually there is no differences between both generation methods (figure 5.6). To check for an wash-out effect, further measurements with particles which are suspended for longer times (several weeks) are necessary.

Out of the investigated materials, the potassium rich feldspar is the most ice active one.

5.3.2 Biological ice nucleating particles

As biological materials we chose to investigate birch pollen washing water (BPWW), SNOMAX® and cellulose. The measurements with SNOMAX® and BPWW were done as part of the diploma work of Manfred Schäfer [Schäfer, 2014], and BPWW was done as part of the Bachelor's thesis by Michael Koch [Koch, 2014].

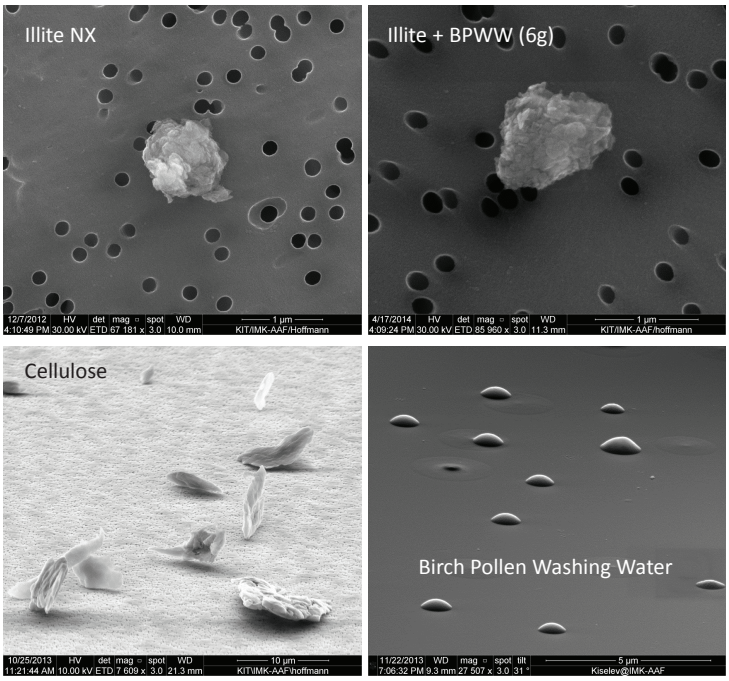

Figure 5.9: SEM images of illite NX, illite NX mixed with BPWW, cellulose, BPWW

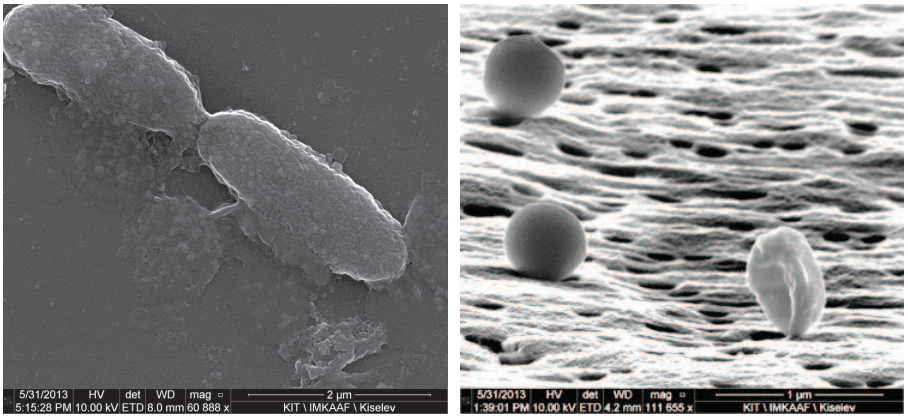

Figure 5.10: SEM images of SNOMAX® dried suspension with entire bacteria (left panel), size selected SNOMAX® particles with a mobility diameter of 550 nm (right panel) (courtesy of Dr. Alexei Kiselev)

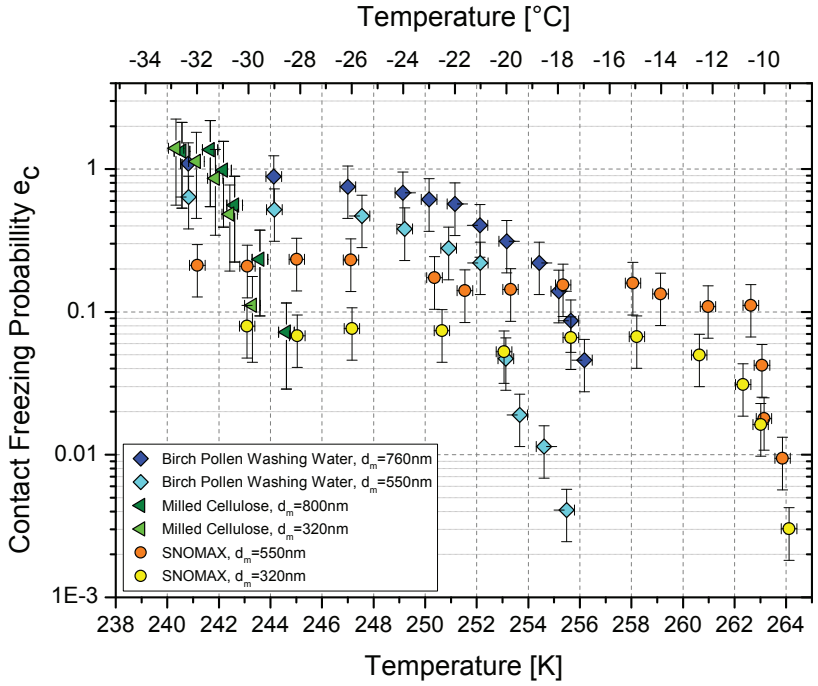

Figure 5.11: Overview of contact freezing experiments with BPWW, SNOMAX® and cellulose

For the pure BPWW the temperature dependency of the contact freezing probability is less steep for temperatures between −20 °C and −34 °C than for temperatures between −17.5 °C and −20 °C (figure 5.11), but we found no plateau like the one described in Augustin et al. [2013] for the immersion freezing mode. The authors report a plateau on the frozen fraction curve at a temperature of about −24 °C for particles with a mobility diameter of 800 nm. The different ice activity could be explained by two different components which cause the freezing. Another interesting founding was, that the particles are not really solid, they are viscose as shown in figure 5.9. Since the aerosol flow passes through a precooler before reaching the EDB, it is possible that the particles have a glassy state when they reach the levitated droplet, but we can not verify that with the current experimental setup. The freezing of BPWW particles colliding with droplets is addressed further in section 5.4.

For the experiments with SNOMAX®, we investigated agglomerates of bacteria fragments, not the entire bacteria. Entire SNOMAX® particles have a length of about 2 µm (figure 5.10), so these particles are too large for size selecting with the DMA we used in our experiments. The SNOMAX® suspension was shaken and generated with an atomizer. The atomizer produces small droplets (d ≈ 4 µm) carrying SNOMAX® fragments and water. The droplets were dried in a diffusion dryer, and the residuals are agglomerates of bacteria fragments. The freezing probability of SNOMAX® particles (figure 5.10) reach a plateau at about −15 °C at values below one (figure

5.11). Since e_c reaches a plateau, every colliding INA protein initiates freezing, which means that for particles of both sizes not every bacteria fragment carries an ice nucleation active (INA) protein complex. Only about 7 % of the 320 nm particles and 20 % of the 550 nm particles carry the ice nucleating component. In the following section, the results of measurement at a temperature of −21 °C and seven different values of mobility diameter are discussed and parametrized.

Cellulose is a less efficient ice nucleating particle compared to BPWW and SNOMAX®. Freezing events could only be measured at temperatures below −28 °C, but than the slope of the temperature dependency is quite steep (figure 5.11). Since the particles are very aspherical (figure 5.9), which causes a broad size distribution (appendix D.5), the calculation of the collection efficiency is subject to larger uncertainties. Considering the broader size distribution of cellulose particles, the error of e_c increase from 35% to 55%. For temperatures below −31 °C the freezing probability is higher than one, which apparently is not physically correct and an artifact caused by the aspherical particle shape.

5.3.3 Surface proportionality of contact freezing efficiency

In the contact freezing mode, the freezing is induced by the contact of an INP with a supercooled droplet. Before, it was not known whether the freezing starts at the point of a contact, or a part of the particle surface is involved. To verify this, measurements at a certain temperature and different particle sizes have been done.

As it was shown in Hoffmann et al. [2013b], there is a clear proportionality of the freezing probability and the particle surface at a temperature of 239.15 K and 240.15 K. Figure 5.12 shows the freezing probability of illite NX at a temperature of 239.15 K, 240.15 K, 241.15 K, and 242.15 K for particles with a mobility diameter of 150 nm, 320 nm, 550 nm, and 750 nm, the freezing probability of kaolinite KGa-1b at 239.15 K for particles with a mobility diameter of 200 nm, 400 nm, 600 nm, and 800 nm, and the freezing probability of BPWW at a temperature of 244.15 K and 249.15 K and particles with a mobility diameter of 200 nm, 320 nm, 440 nm, 550 nm, 650 nm, and 760 nm, respectively. The BPWW data was measured as part of Manfred Schäfer's diploma thesis [Schäfer, 2014]. As minerals only illite and kaolinite KGa-1b have been used, because of their almost spherical shape and the narrow size distribution.

Due to the spherical shape, the linear relationship between e_c and the particle surface S_p could be demonstrated for illite NX and kaolinite KGa-1b. For other mineral dust particles, the size distribution was too broad to see a clear relationship. However, the fact that all values measured so far fall on one line if presented in form of INAS density, implies that this properties is universal for all aerosol particles investigated in this work.

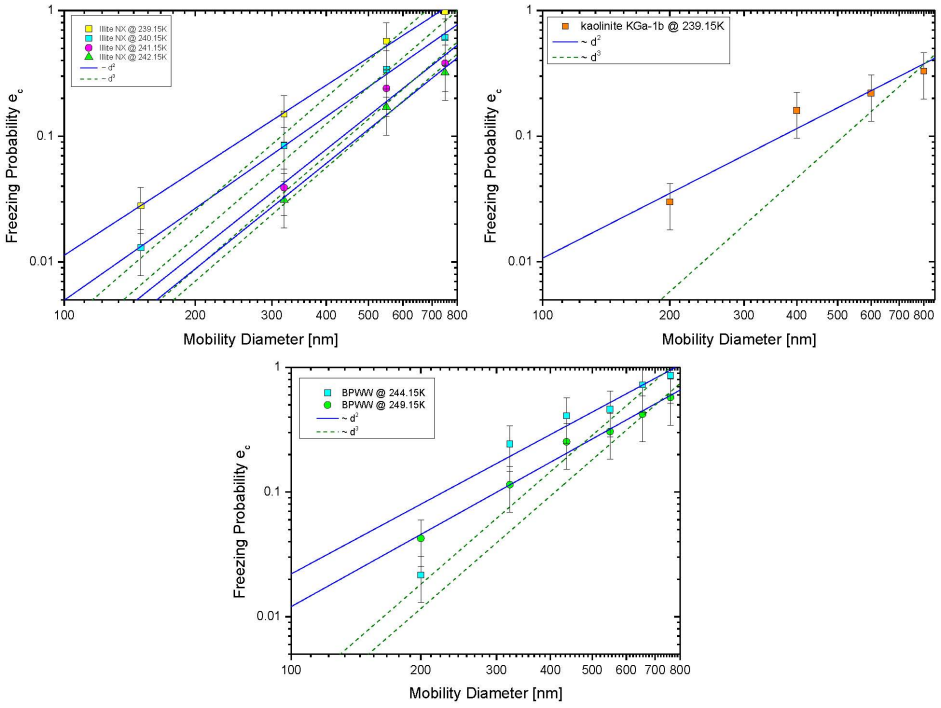

Figure 5.12: Relationship between the freezing probability of illite NX, kaolinite KGa-1b and BPWW to the particle surface area

All these results show a proportionality of the freezing probability to the particle surface. This is a hint that the concept of a point contact which initialize the freezing is not valid. It seems more likely that a part of the particle surface, or the entire particle surface is involved in the freezing process. The exact cause, which triggers the freezing, is not clear and more research is necessary. A possible experimental setup will be discussed in section 6.1.

5.4 Parametrization of SNOMAX® and BPWW results

It is difficult to distinguish between contact and immersion freezing mode in this kind of experiments. The problem is that the fraction of the particle surface facilitating the freezing is unknown. In case of SNOMAX®, the situation is even more complex due to the fact that only INA protein complexes serve as ice nucleating site. In the following, the distribution of ice-active sites among the SNOMAX® particles is quantified based on the measured values of e_c. To investigate the size dependency of the contact freezing efficiency, SNOMAX® particles between 200 nm and 800 nm have been investigated at a fixed temperature (−21 °C).

The approach suggested in Hartmann et al. [2013] is used to compare volume and surface distribution of ice active sites. We considered two scenarios: the INA protein is located on the surface dS or in the volume dV of a spherical particle with a diameter d_p. The surface of a particle is given by:

$$dS = \pi \cdot d_p^2 \tag{5.3}$$

and the volume by:

$$dV = \frac{1}{6}\pi \cdot d_p^3 \tag{5.4}$$

Assuming that the number of INA proteins is Poisson distributed, the probability of a number of n INA proteins on a particle is given by

$$P(n, \lambda) = \frac{(\lambda)^n e^{-\lambda}}{n!} \tag{5.5}$$

with $\lambda = \lambda' dS$ or $\lambda = \lambda'' dV$. λ' or λ'' is the mean number of INA protein per particle surface dS or particle volume dV, respectively. The probability to find at least one INA protein is given by

$$\sum_{n=1}^{\infty} P(n, \lambda' dS) = 1 - P(0, \lambda' dS) = 1 - e^{-\lambda' dS} \tag{5.6}$$

or

$$\sum_{n=1}^{\infty} P(n, \lambda'' dV) = 1 - P(0, \lambda'' dV) = 1 - e^{-\lambda'' dV} \tag{5.7}$$

Since the freezing probability can not exceed one, which means every colliding particle leads to a freezing event, an amplitude $A = 1$ must be added to the equation.

$$\chi(d_p) = A\left(1 - e^{-\lambda' \cdot \pi \cdot d_p^2}\right) \;\Rightarrow\; \chi(d_p) = 1 - e^{-\lambda' \cdot \pi \cdot d_p^2} \tag{5.8}$$

or

$$\psi(d_p) = 1 - e^{-\lambda'' \cdot \frac{1}{6}\pi \cdot d_p^3} \tag{5.9}$$

Assuming that at low temperatures (on a plateau), the probability to have one protein complex is equal to the probability of freezing, the functions χ and ψ can be used to fit the experimental results. However, we have to make an assumption that the entire particle surface or volume is available for the contact with the droplet. In case of volume-distributed INA proteins, this would mean that the SNOMAX® particle should be deagglomerated on contact with a water droplet.

λ' has a value of $1.35 \cdot 10^{-7}\,\mathrm{nm}^{-2}$ for SNOMAX® (figure 5.13), which means that on an area of about $7.4 \cdot 10^6\,\mathrm{nm}^2$ one INA protein complex exists, and that is the surface area of a spherical particle with a mobility diameter of about 1536 nm. λ''

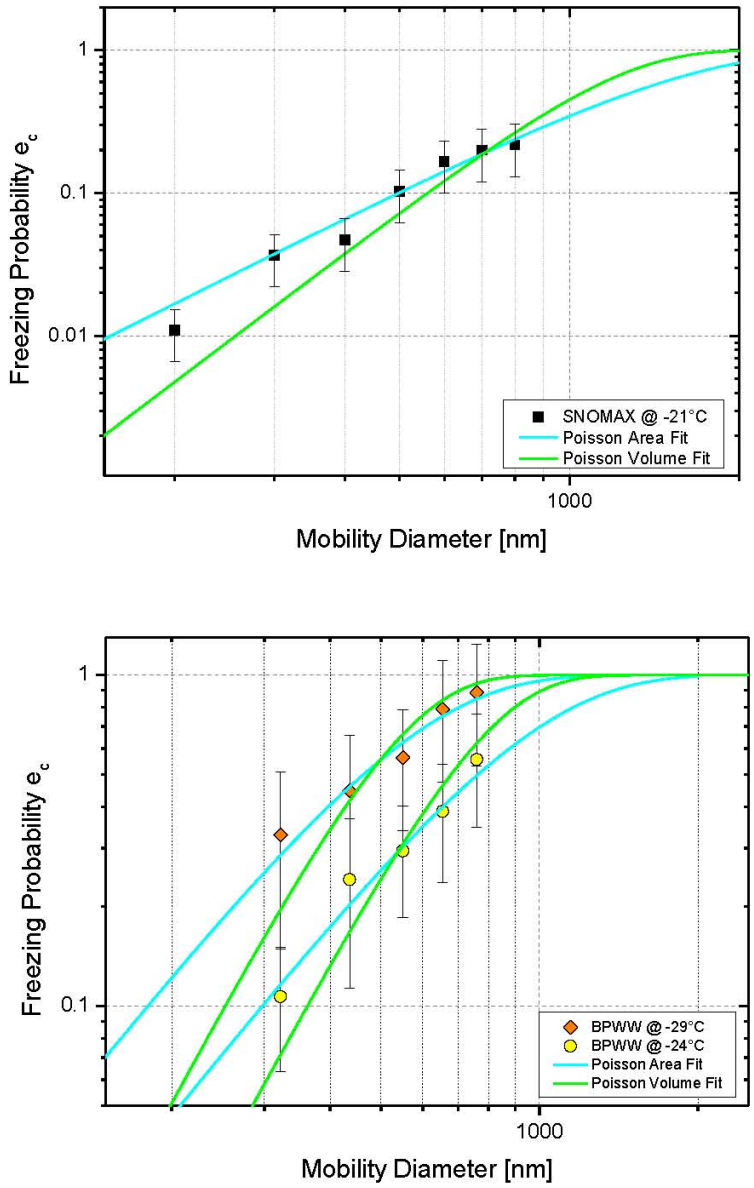

Figure 5.13: Parametrization of the size dependency of the contact freezing probability of SNOMAX® and BPWW, following the parametrization of Hartmann et al. [2013]

has a value of $1.14 \cdot 10^{-9}\,\mathrm{nm}^{-3}$ for SNOMAX® (figure 5.13), whixh means that in a volume of about $8.8 \cdot 10^{8}\,\mathrm{nm}^{3}$ one INA protein complex exists, and that is the volume of a particle with a mobility diameter of about 1188 nm. Figure 5.13 shows both functions and it is easy to see that the surface dependent fit function $\chi(d_p)$ fits the freezing probability much better than the volume dependent function $\psi(d_p)$ as shown by the correlation coefficient (surface fit: $R^2 = 0.96$, volume fit: $R^2 = 0.88$).

Hartmann et al. [2013] gives a value for SNOMAX® particles with mobility diameters of 300 nm and 650 nm of 0.03 and 0.17 INA protein complexes in their volume, respectively. Applying this to our experiment and assuming a particle concentration of $480\,\mathrm{cm}^{-3}$, about $15\,\mathrm{cm}^{-3}$ with a mobility diameter of 320 nm and $82\,\mathrm{cm}^{-3}$ with a mobility diameter of 550 nm carry an INA protein. So the droplets can collect at most 1 or 3 SNOMAX® particles carrying an INA protein complex during a residence time of 30 s in the EDB, respectively. This means, in average every droplet should freeze during 30 s, when the entire volume of the SNOMAX® particle is available as INP, but we see only a freezing probability of 7% for 320 nm particles and 20% for 550 nm.

The parametrizations of our results have a similar outcome: Calculated from the surface parametrization, SNOMAX® particles with a mobility diameter of 320 nm or 550 nm carry about 0.04 or 0.13 INA protein complexes, respectively.

When we use the volume fit, for a SNOMAX® particle with a mobility diameter of 320 nm or 550 nm, 0.02 or 0.1 INA protein complexes would be present, respectively.

Assuming a particle concentration of $480\,\mathrm{cm}^{-3}$, about $19\,\mathrm{cm}^{-3}$ with a mobility diameter of 320 nm and $63\,\mathrm{cm}^{-3}$ with a mobility diameter of 550 nm carrying an INA protein on their surface. So the droplets can collect at most 1 or 2 SNOMAX® particles carry an INA protein complex on the surface during a residence time of 30 s in the EDB, respectively. For the results of the volume fit, about $10\,\mathrm{cm}^{-3}$ with a mobility diameter of 320 nm and $49\,\mathrm{cm}^{-3}$ with a mobility diameter of 550 nm carry an INA protein on their surface. So every second droplet can collect a 320 nm particle carrying an INA protein complex in its volume, or every droplet can collect two SNOMAX® particles carrying an INA protein complex in its volume during a residence time of 30 s in the EDB, respectively.

Similar to the results of the parametrization of Hartmann et al. [2013], the results of our parametrizations provide too high values for the distribution of INA protein complexes to explain the measured freezing probabilities. Since the SNOMAX® particles are agglomerates of bacteria fragments, a possible explanation could be, that the proteins are located on positions, where they can not come into contact with the droplet.

The freezing probability of BPWW particles do not reach a plateau at a certain temperature like SNOMAX®, so we can not assume, that every colliding ice nucleating component (for BPWW we do not know which component that is) initialize freezing. Nevertheless, for BPWW the surface dependent fit function fits better than the

volume function for both temperatures. This shows, even these particles having a viscous structure do not go into solution as soon they collide with the particle.

5.5 Mixture of illite and birch pollen washing water

According to Möhler et al. [2007] it is more likely that biological material is located on mineral dust particles, than that isolated mineral dust and biological materials coexist in the atmosphere. As a model substance possibly relevant for ice formation in the atmosphere, the mixture of illite NX and BPWW has been investigated. The BPWW was prepared with the following concentrations: 1.5 g, 2.2 g, 3 g, and 6 g pollen washed in 100 ml deionized water, respectively, and mixed with 50 g illite NX powder. The increase of the residuals are shown in table 3.2. In the following the different samples are named after the amount of birch pollen which have been used to produce the BPWW. Figure 5.14 shows the results in comparison to the results of pure illite NX and pure BPWW.

The mixture with 1.5 g pollen already shows an increase in the ice activity compared to pure illite NX. The 2.2 g sample increased the freezing probability a little more, but the highest influence showed the 3 g sample. For temperatures lower than −28 °C the ice activity is now as high as the ice activity of pure BPWW, but not for higher temperatures. The idea was to produce a mixture with more and more concentrated solution of BPWW, until the contact freezing behavior of pure BPWW could be reconstructed. The surprising finding was that the ice activity of a mixture with 6 g pollen showed a decrease in the ice activity down to the values corresponding to the 2.2 g sample. To ensure that the high amount of pollen did not clog the filter, we also prepared samples with twice the BPWW of 3 g pollen and mixed it with 50 g of illite NX, but this sample showed the same results. It is obviously not possible to bring more BPWW material onto the illite surface. But something else must have happened, since the freezing probability decreased. Maybe because of the high concentration, a fraction of the material has formed agglomerates in the suspension and was not adhering to the illite particles. None of the mixtures were as ice active as pure BPWW, indicating that the particles were not completely enclosed in the biological material.

Analysis with SEM showed no visual (figure 5.9) or spectral (energy-dispersive X-ray (EDX) spectroscopy) (figure 5.15) differences between pure illite NX and illite NX mixed with BPWW. The EDX spectra showing no signs of BPWW on the illite particles is probably caused by the fact that EDX is not sensitive to small amounts of mostly carbonaceous biological materials, and that the illite particles are obviously not coated completely with a thick layer of BPWW, since they do not show the same ice activity as pure BPWW.

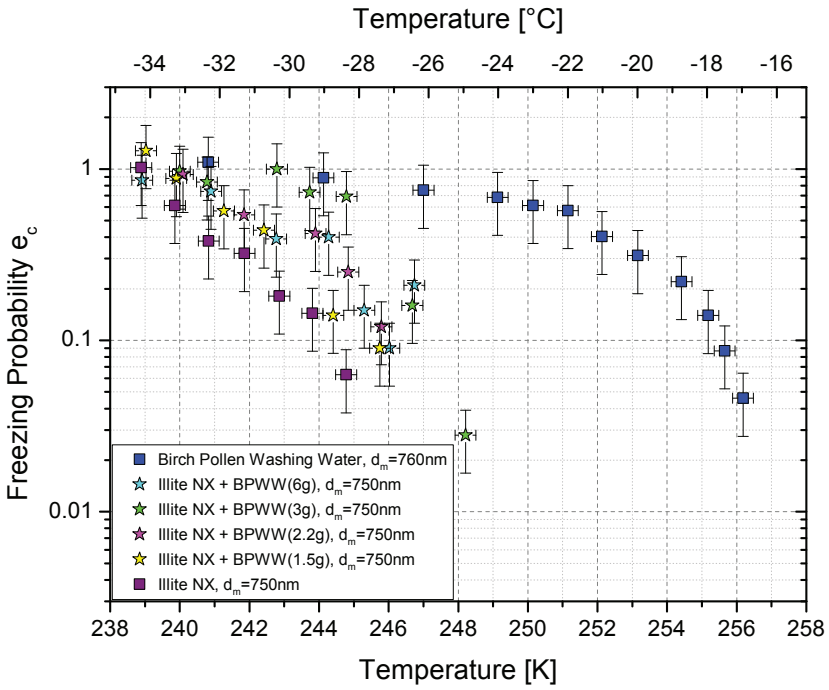

Figure 5.14: Overview of contact freezing results for pure illite NX, pure BPWW, and the mixtures of both substances

To verify that BPWW is located in the pores of the illite particles, the effective surface area of illite NX mixed with BPWW of different concentrations was measured with the Brunauer-Emmett-Teller (BET) method (courtesy of T. Kisely, Institute for Nuclear Waste Disposal, KIT). Table 5.2 shows the results. To verify, whether the method itself has an influence on the particle surface, a mixture of illite NX and deionized water was prepared the same way, the mixtures with BPWW were prepared. The BET surface area showed now difference to the BET surface of pure illite NX powder. The mixture of 1.5 g pollen showed a 10% decrease in the BET surface area. This indicates that the BPWW material is located in the pores inside the particle. For the 3 g sample, the BET surface area is about 30% lower than the BET surface area of pure illite NX, but in the sample with 6 g no further decrease was observed. It seems that all pores of the illite particle surface are already filled with BPWW material and no more material can be absorbed. The BET surface of a 750 nm particle ($A_{\mathrm{BET}} = 5.1 \cdot 10^{-11}\,\mathrm{m}^2$) is still larger than the geometric surface of a sphere with a diameter 750 nm ($A_{\mathrm{geo}} = 1.77 \cdot 10^{-12}\,\mathrm{m}^2$), but the particles are not perfect spheres and irregularities on the particle surface are obviously still present, even if there are less irregularities on the surface than on a pure illite NX particle.

Measuring the effective density of pure illite NX and illite NX mixed with BPWW with APM has shown, that the particles mixed with BPWW have a slightly higher effective density than the pure mineral dust particles (figure 5.16). This result is also

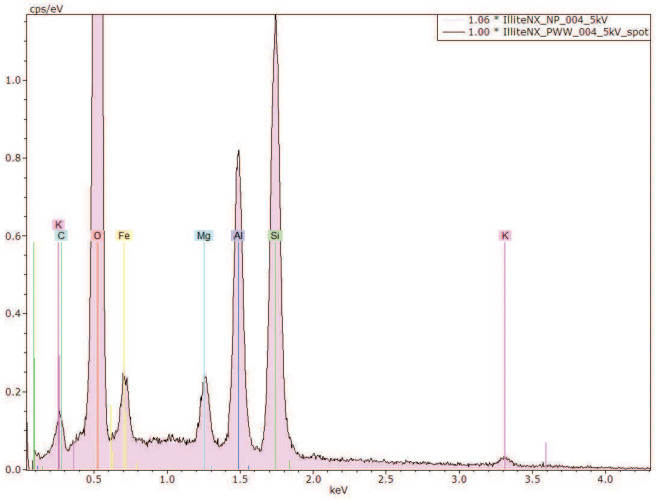

Figure 5.15: EDX spectra of pure illite (purple) and illite mixed with BPWW (black curve), scaled to the total intensity of Si band

Table 5.2: Overview of BET surfaces (measurements courtesy of Tanja Kisely)

Material	Concentration [g/100 ml]	BET surface [m^2/g]
Illite NX		124±12
Illite NX + deionized water		123±12
Illite NX + BPWW	1.5	112±11
Illite NX + BPWW	3	87±8
Illite NX + BPWW	6	88±9

proof that the BPWW material was present on the illite particles.

To get more information about the component in the BPWW, and to find its distribution within illite particles, the samples were analyzed using a confocal fluorescence microscope at the Institute of Toxicology and Genetics (supervised by Dr. Masanari Takamiya). The spectra in figure 5.17 show a fluorescence signal at a excitation wavelength of 405 nm for pure illite NX, illite NX mixed with BPWW (3 g) and illite NX mixed with BPWW (6 g). The spectra of pure illite NX and illite NX mixed with BPWW (3 g) show a small difference, but interestingly there is a much stronger signal for the illite NX mixed with BPWW (6 g) sample. Obviously more fluorescent material – whatever it is – is present in the 6 g sample. Pöhlker et al. [2013] analyzed 29 different pollen species using excitation wavelengths between 220 nm and 550 nm and emission wavelengths between 380 nm and 600 nm. The authors found that "among all dry pollen samples studied, three fluorescence modes appear most prominent: (A) a mode at $\sim$ 280/450 nm ($\lambda_{ex}/\lambda_{em}$), (B) a mode at $\sim$ 355/450 nm, and (C) a mode at $\sim$ 460/520 nm" [Pöhlker et al., 2013]. Fluorescence mode (C)

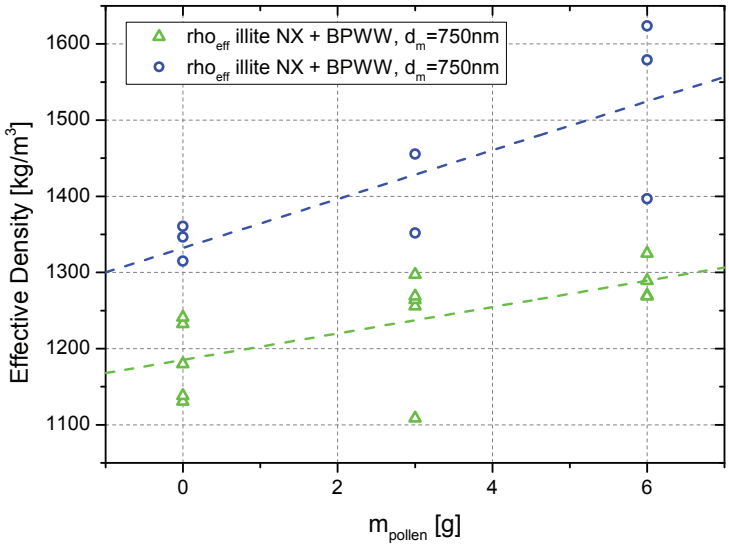

Figure 5.16: Effective density of pure illite NX and illite NX mixed with BPWW (3 g and 6 g)

represents the results found in our analyses best, and this mode is prominent for carotenoids, and thus carotenoids are possibly responsible for the fluorescence of BPWW.

Unfortunately, the resolution of the microscope is not high enough to identify the location of BPWW on the surface of single particles.

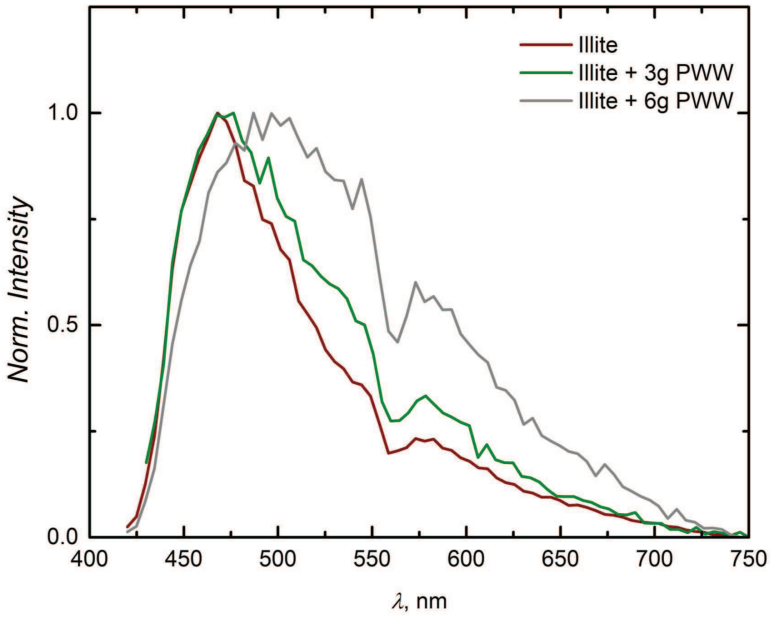

Figure 5.17: Fluorescence spectra of pure illite NX, illite NX mixed with BPWW (3 g) and illite NX mixed with BPWW (6 g). Excitation wavelength 405 nm.

5.6 Immersion freezing results and comparison with contact freezing results

5.6.1 Comparison based on the INAS density concept

To compare the freezing efficiency of INP in contact and immersion modes, a consistent unit is necessary. One possibility to define such a unit is the "ice nucleation active site (INAS) density" as described in Connolly et al. [2009] and Hoose and Möhler [2012]. "The INAS density describes the number of ice nucleation active sites at a certain temperature and supersaturation, normalized by the aerosol surface area. The approach is based on the assumption that the investigated aerosol sample is of uniform composition. Time dependence is not taken into account." [Hoose and Möhler, 2012]

The INAS density n_s can be calculated from:

$$n_s = \frac{\ln(1 - f_{\text{ice}})}{S_{\text{IN}_{\text{tot}}}} \quad \text{with} \quad 1 - f_{ice} = \frac{N_u}{N_0} \tag{5.10}$$

$S_{\text{IN}_{\text{tot}}}$ is the particle surface of all immersed particles.

For contact freezing results, the so-called CINAS density n_{cs} is described by:

$$n_{\text{cs}} = \frac{e_c}{S_{\text{IN}}} \tag{5.11}$$

with the part of the particle surface which is involved in the contact freezing process S_{IN}.

The CINAS density is independent of the particle size, so that the calculation of the CINAS density is also a verification for the correctness of the size selection and calculation of the contact freezing probability. As shown in figure 5.18 the values of CINAS density for all particle sizes for illite and feldspar fall together onto one line.

One source of uncertainty for the CINAS density is that it is not known what part of the particle surface is involved in the freezing process. It is conceivable that the entire surface or only a part of the particle is wetted when the particles come into contact with water. For the calculations shown in figure 5.18 to 5.21 the entire particle surface was assumed to be involved in the freezing process. If only half of the particle surface would have been immersed in the droplet, the CINAS density would increase by a factor of two, so that the given CINAS density should be considered at the lowest possible value.

As mentioned in chapter 4 it is also possible to measure the immersion freezing efficiency of INP with this experimental setup. To achieve that, the droplet is exposed to the aerosol flow for a certain time (usually between 10 and 30 s), allowing for

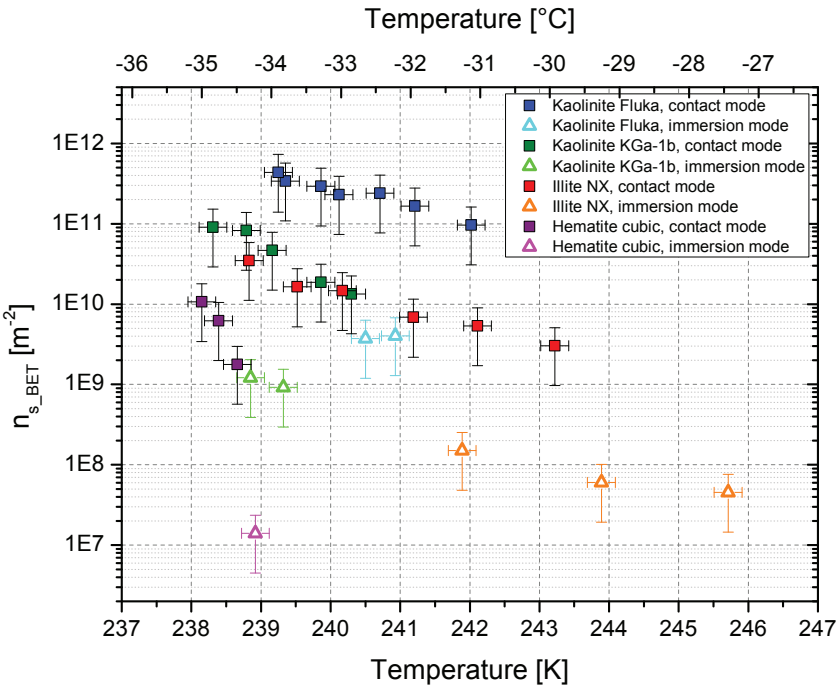

Figure 5.18: Immersion freezing results (INAS density) in comparison to the contact freezing results (CINAS density) of the same aerosol material for kaolinite Fluka, kaolinite KGa-1b, illite NX and hematite

aerosol particles collection. The aerosol is then removed from the flow by switching on the field in the electrostatic precipitator. If the droplet did not freeze on a collision, the average time needed for droplet to freeze would be the measure of INP efficiency in immersion mode.

Figure 5.18 shows the results of immersion freezing experiments with kaolinite, illite and hematite. The ice activity shows the same order as the contact mode. Hematite is the worst INP, illite NX and kaolinite KGa-1b are more ice active and kaolinite Fluka is the most ice active out of all investigated materials. For all materials, the INAS density is lower than the CINAS density. To show that the CINAS density is really higher than the INAS density, I compare some results of immersion freezing experiments reported by other authors.

Figure 5.19a) shows the CINAS density of illite for four different particle sizes and the INAS density compared to the INAS density of Broadley et al. [2012]. Figure 5.19b) shows the CINAS density of feldspar microcline and andesine from Darmstadt and Leeds (cf. section 3.7) compared to the INAS density of Atkinson et al. [2013], and the CINAS and INAS densities of kaolinite KGa-1b. Note, that the CINAS density of different particle sizes fall on one line, which supports the idea of surface dependence of contact freezing efficiency. The INAS density provided by Broadley et al. [2012] is in the range of the CINAS density of illite NX. The INAS densities

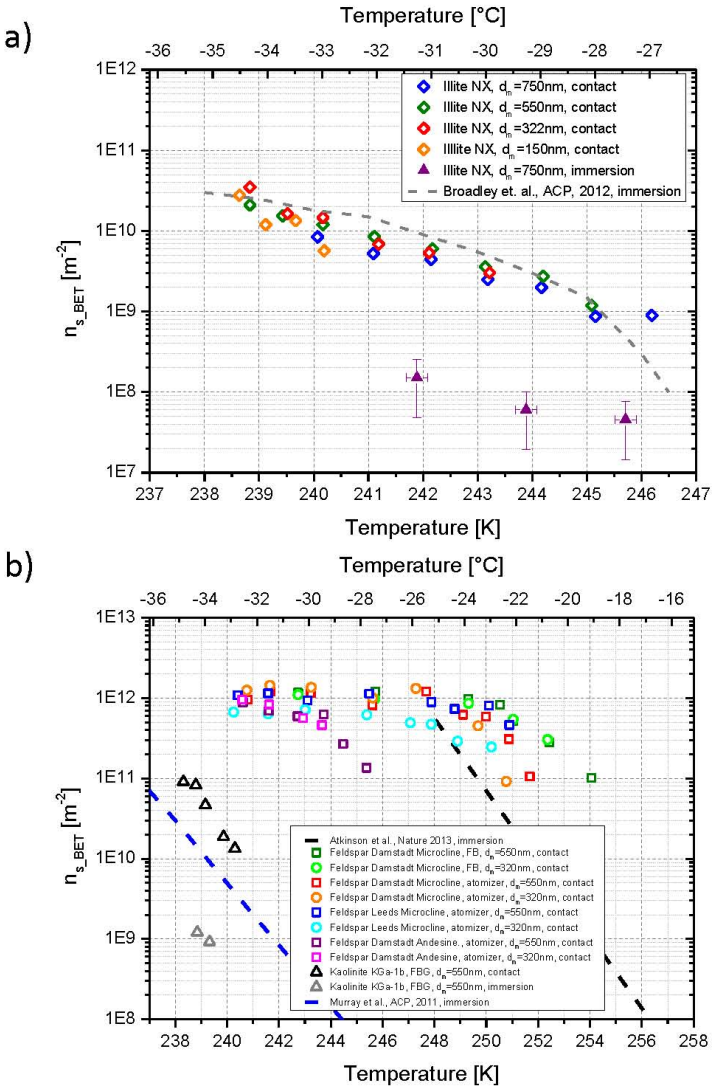

Figure 5.19: a) CINAS and INAS density of illite NX compared to the results of Broadley et al. [2012]; b) CINAS density of feldspar microcline and andesine from Darmstadt and Leeds compared to the results of Atkinson et al. [2013] and CINAS and INAS density of kaolinite KGa-1b compared to the results of Murray et al. [2011]

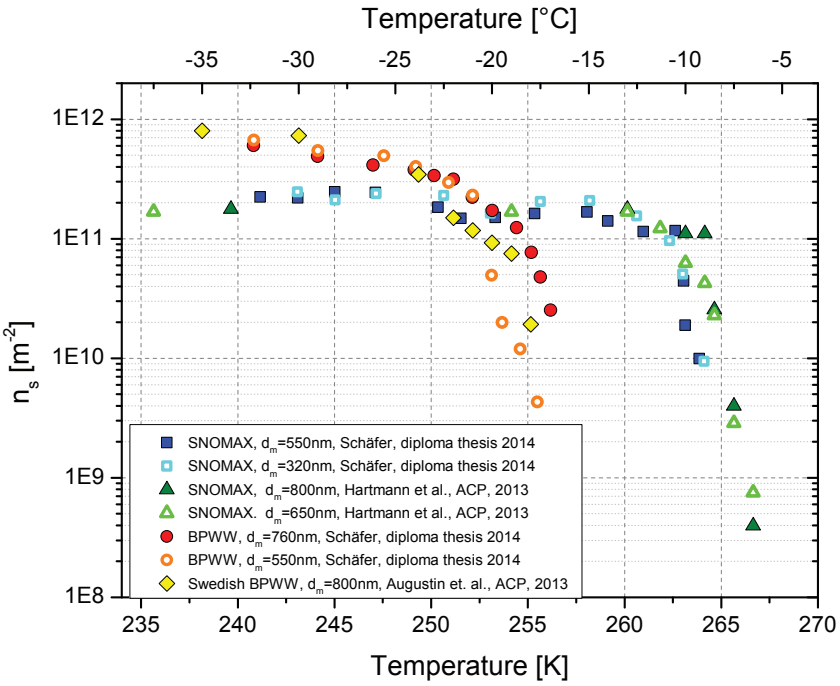

Figure 5.20: Comparison of SNOMAX® INAS density from Hartmann et al. [2013], BPWW INAS density of Augustin et al. [2013] and CINAS density of BPWW and SNOMAX® from Schäfer [2014]

provided by Atkinson et al. [2013] and Murray et al. [2011] for K-feldspar and kaolinite KGa-1b are lower than the CINAS densities. The INAS density of illite NX and kaolinite KGa-1b of this experiments are lower than the INAS density of Broadley et al. [2012] and Murray et al. [2011], respectively, but still well within the boundaries of variability. The methods of Broadley et al. [2012] and Murray et al. [2011] are based on calculating the total particle surface area in the droplet from average weight fraction of mineral dust suspension in water. In contrast, mobility selected particles are collected by the droplet in our experiment.

The CINAS density of SNOMAX® and BPWW show no difference to the INAS density of Hartmann et al. [2013] and Augustin et al. [2013], respectively (figure 5.20). Obviously, it is not possible to distinguish between contact and immersion freezing mode. A further indication that our results can be interpreted as immersion freezing results give the calculation of t_{im} in section 5.6.2.

Hiranuma et al. [2014a] compares ice nucleation experiments of the INUIT partners using illite NX as INP (figure 5.21). The INAS densities of the contact freezing results are calculated using the geometric particle surface. The calculation with BET surface area would increase the values by an order of magnitude, so that they are in the range of the data of Broadley et al. [2012] (purple line) (compare figure 5.19a).

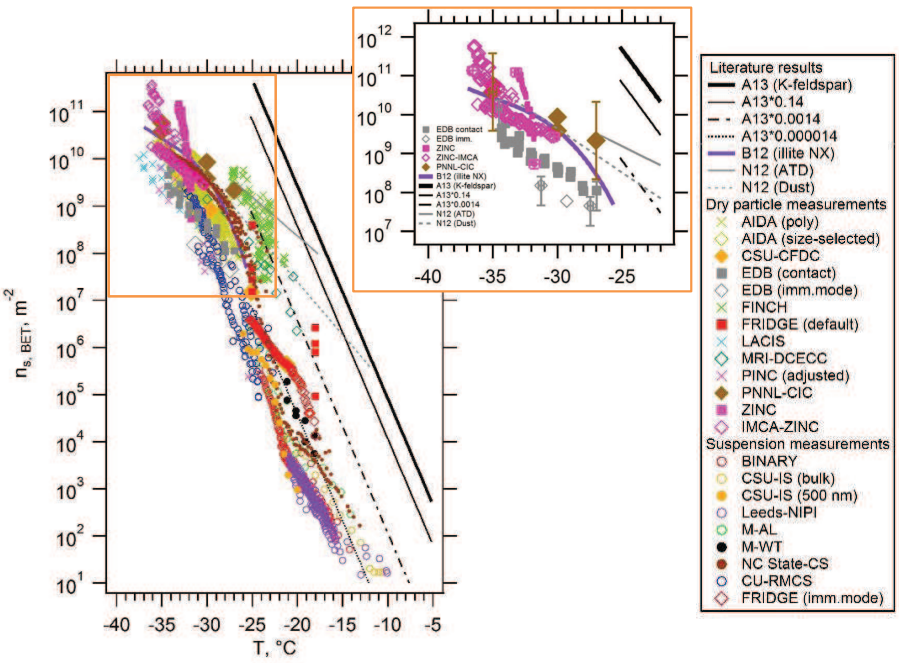

Figure 5.21: Comparison of ice nucleation experiments of the INUIT partners with illite NX [Hiranuma et al., 2014a]

The contact freezing results are located in the upper region of the bulk of results, and the immersion freezing results of our study are located in the lower region.

The immersion freezing results of EDB measurements should be treated with caution, since it is possible that the efficient INP already initiate contact freezing during collection time, and only the inefficient INP are available for immersion freezing, assuming, that efficient contact freezing INP also efficient INP in immersion mode.

5.6.2 Comparison based on characteristic time

Another way to check whether the immersion freezing could dominate in the experiment is to calculate the average time t_{im} after which the immersion freezing would start dominating the contact freezing. The following passage (shown as indented text) is closely citing [Hoffmann et al., 2013a]:

> Using the expressions from eqs. 4.3 and 4.4 the condition for the linearity of the freezing curve $J_c \gg J_i$ can be rewritten
>
> $$e_c \gg \frac{1}{2} S_{\mathrm{INP}} j_i t. \tag{5.12}$$
>
> This leads to us observing a linear freezing curve, which means the probability of contact freezing upon a single collision e_c is higher than the probability of

immersion freezing after waiting the time $t_{\max}$, which was typically set to 30 s in our experiment. The above expression, eq. 5.12, also provides the basis for comparison of the contact and immersion freezing rates for atmospherically relevant types of INP and realistic collision rates: for the given rate of collisions n_c between droplets supercooled to the temperature T_s and INP with characteristic values S_{INP}, j_i, and e_c, one can define the average time t_{im} after which the immersion freezing rate would start dominating the contact freezing:

$$t_{\mathrm{im}} = \frac{2e_c}{S_{\mathrm{INP}}} j_i. \tag{5.13}$$

Only for $t_{\max} \ll t_{\mathrm{im}}$ the simplified equation 4.7 is suitable to calculate the freezing probability, otherwise equation 4.6 must be used. This calculation is only true when we assume that the total particle surface is involved in the freezing process. As shown in section 4.1, it is unlikely that the particle goes into the droplet during the experiment time of 30 s, so the particle has to be wetted at the contact with water.

Even though it is unlikely that the particle penetrates the droplet surface directly at collision, it is possible that the particle is "swimming" on the droplet surface. If the freezing has not been initiated on collision, but occurred after some finite time t_{im} this freezing mechanism should be classified as immersion freezing. To calculate t_{im}, the immersion freezing rate is needed. The immersion freezing rate J_i can be calculated from the frozen fraction f_{ice} which is given by the number of frozen droplets N_f divided by the total number of investigated droplets N_0:

$$\frac{N_u}{N_0} = 1 - f_{\mathrm{ice}} \tag{5.14}$$

$$J_i = \frac{\ln(N_u/N_0)}{t} \tag{5.15}$$

with t the residence time of the particle in the droplet.

Figure 5.22 shows the calculated t_{im} for kaolinite Fluka, illite NX, feldspar microcline, BPWW and SNOMAX®. The frozen fractions used to calculate the immersion freezing rate for kaolinite Fluka (d_m = 300 nm), illite NX (d_m = 300 nm) and feldspar microcline (d_m = 300 nm) are from Augustin-Bauditz et al. [2014], for BPWW (d_m = 800 nm) from Augustin et al. [2013] and for SNOMAX® (d_m = 650 nm) from Hartmann et al. [2013]. The setup these authors used for their experiment is the Leipzig Aerosol Cloud Interaction Simulator (LACIS) [Hartmann et al., 2011]. In this setup, the experiment time is about 1.5 s.

For kaolinite Fluka and illite NX, t_{im} is longer than 30 s, but for feldspar microcline t_{im} = 18 s at −26 °C and t_{im} = 2.3 s at −30 °C, which means especially for low temperatures, immersion freezing could be possible. For BPWW and SNOMAX® t_{im} is between one and two seconds, indicating, that especially for biological materials the immersion mode is not negligible.

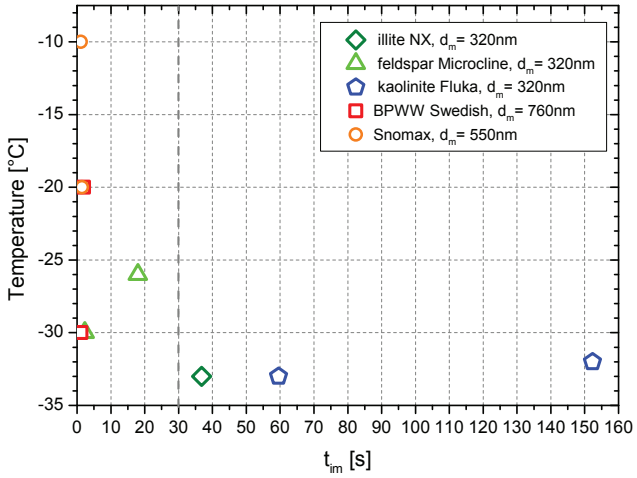

Figure 5.22: Calculation of t_{im} by using f_{ice} from Augustin-Bauditz et al. [2014] for kaolinite Fluka, illite NX and feldspar microcline, Augustin et al. [2013] for BPWW, Hartmann et al. [2013] for SNOMAX®

As shown in the simulations in figure 4.8, for high immersion nucleation rate, meaning t_{im} is shorter than the arrival time of a new colliding particle, the freezing curve is linear and contact and immersion freezing mode can not be distinguished anymore. Figure 5.20 shows that the INAS and CINAS densities of SNOMAX® and BPWW match each other, indicating both the contact and immersion freezing modes can be responsible for freezing in this experiment.

To obtain more information about the residence time of a particle on the droplet surface before initiation of freezing, to explore the various scenarios of particle wetting or immersion on a contact, further studies are necessary. A possible setup is discussed in section 6.1.

5.7 Comparison with the contact freezing results of other research groups

Unfortunately, only a small number of contact freezing results are available from other research groups. The comparison is complicated due to the fact that the number of collisions per droplet and the size distribution of the INP particles in the experiments is not always known. Ladino Moreno et al. [2013] compared contact freezing results of kaolinite experiments of Svensson et al. [2009] (EDB), Pitter and Pruppacher [1973] (wind tunnel), Ladino et al. [2011a] (CLINCH), Hoffmann et al. [2013a] (EDB), and Bunker et al. [2012] (cold plate) (figure 5.23). The results are

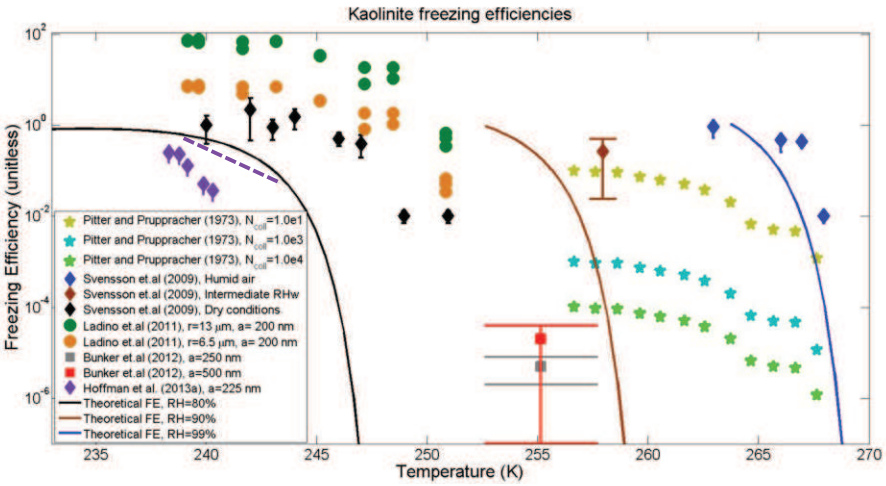

Figure 5.23: Comparison of contact freezing experiments with kaolinite as a function of temperature from different instruments [Ladino Moreno et al., 2013]. Pitter and Pruppacher [1973] do not give a number of collided particles N_{coll}, so Ladino Moreno et al. [2013] assumed different values for N_{coll}. Svensson et al. [2009], Ladino et al. [2011a], and Bunker et al. [2012] used kaolinite Fluka particles for their experiments. Hoffmann et al. [2013a] used kaolinite KGa-1b. a and r give the particle and droplet radius, respectively. The purple dashed line shows the position of kaolinite Fluka of this work.

compared in form of freezing efficiency FE, which is given by the ratio of the frozen fraction f_{ice} to the number of collided particles N_{coll}.

There are huge differences in the freezing efficiencies. The data of Svensson et al. [2009] shows that the humidity conditions influence the ice activity, so that different conditions in the experimental setups could be a reason. One reason, the results of Hoffmann et al. [2013a] are lower than those of Svensson et al. [2009] under dry conditions, and Ladino et al. [2011a] is that they used kaolinite Fluka, and we used kaolinite KGa-1b, which is less ice active than kaolinite Fluka as shown in 5.3.1. The results of Fluka are closer to the results of Svensson et al. [2009], but still a bit lower. Bunker et al. [2012] also used kaolinite Fluka particles for their experiments.

Niehaus et al. [2014a] analyzed three mineral dusts and three strains of bacteria in the contact mode. Figure 5.24 shows the results of K-feldspar and SNOMAX® in comparison to the results of this work. To calculate the CINAS density, the geometrical surface of the collected particles is used. Since in the experiments of Niehaus et al. [2014a] much more particles deposited on the droplet, they were able to measure at higher temperatures than in the experiments of this work. The results for SNOMAX® in both experiments fit very well. The interpretation of the strong discrepancy between the K-feldspar data is by far less obvious because of the

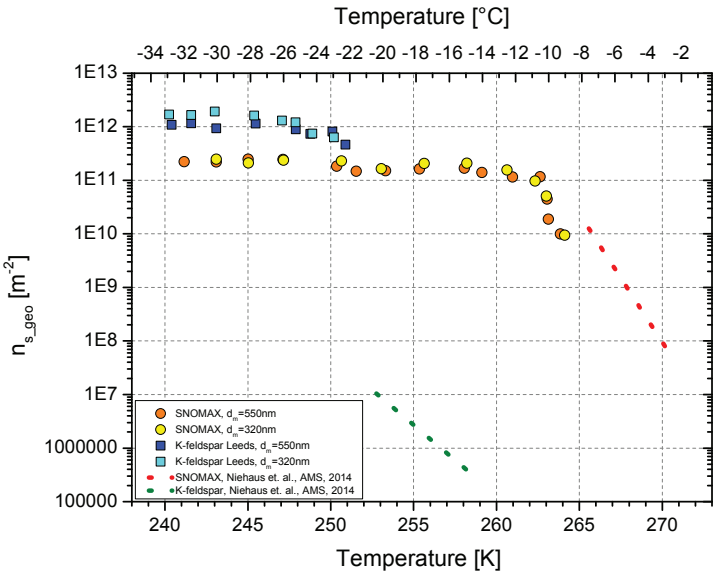

Figure 5.24: CINAS density of K-feldspar and SNOMAX® compared to the results of Niehaus et al. [2014a]. The geometrical particle surface is used to calculate n_s.

non overlapping temperature ranges in the two experiments. It is possible that the contact freezing probability measured in the EDB is falling so rapidly with rising temperature, that a match between the data set could be achieved. The true reason for the observed effect remains to be discovered. The CINAS density would have to decrease four orders of magnitude within 1 °C, which is possible, but has to be verified.

6 Summary and conclusions

The purpose of this work was to characterize the contact freezing mode for representatives of atmospherically relevant aerosol materials. This work was done as part of the DFG research project "Ice Nuclei research UnIT" (INUIT), which was initiated to investigate heterogeneous freezing processes in the atmosphere.

The laboratory studies were focused on the following reference aerosols: hematite, illite, kaolinite, and feldspar as atmospherically relevant mineral dust aerosols. SNOMAX® particles were chosen to represent the ice active bacteria of the strain Pseudomonas Syringae and birch pollen washing water (BPWW) was chosen to represent the potentially ice active secondary biological material. Since every participating institute has been using the same aerosols, it is possible to compare results of different experimental methods and freezing modes. In addition, the plant component cellulose was investigated and, as a model of natural aerosols, the mixture of illite and BPWW was analyzed.

To verify the influence of immersion freezing events on the shape of a $\ln(N_u/N_0)$ curve, simulations with different contact freezing probabilities and immersion freezing rate were done. If more than 5 % of the droplets freeze due to immersion nucleation, the influence on the shape of the freezing curve is strong enough to be identified.

All investigated aerosols showed a similar temperature and size dependency in the contact freezing mode (figure 5.7, 5.8, and 5.11).

Out of the investigated mineral dust particles, the potassium-rich (K-)feldspar was the most ice efficient material and the only one, where the freezing probability reached a plateau. The plateau reaches unity, which means that every colliding particle initializes freezing for particles with a mobility diameter of 550 nm. For particles with a mobility diameter of 320 nm the plateau was located at 0.7 (70% of the colliding particles initialize freezing). The freezing probability of the sodium-rich feldspar has shown a similar behavior, but the freezing probability was lower. For the particles with a mobility diameter of 550 nm a change in the slope of the temperature dependency at −31 °C has been observed, the slope becoming less steep below this temperature. It seems that feldspars have two different types of ice active sites. The other minerals show a linear temperature dependency.

The comparison of K-feldspar generated from water suspension and dry powder has shown that the dry generated particles are slightly more ice active than the particles generated from a suspension. The contact freezing probability of dry generated

particles have been found to be a factor of about 1.5 higher than for suspension generation.

The most ice nucleating efficient biological material was SNOMAX®. Below −15 °C, its freezing probability reaches a plateau at the level of 0.2 for particles with a mobility diameter of 550nm and at the level of 0.07 for particles with a mobility diameter of 320nm. In contrast to feldspar, this behavior is easily to explained, because not every bacteria fragment carries an ice nucleation active protein complex. The BPWW particles behave similarly to feldspar and have two different ice active regimes. The temperature dependency is steeper for temperatures higher than −21 °C. Cellulose is ice active only at temperatures close to the homogeneous freezing limit and shows a very steep temperature dependency. The collection efficiency, calculated assuming sphericity of the cellulose particles, is obviously overestimated, explaining why the freezing probability is higher than one at low temperatures.

The freezing probability of the mixture of illite NX and BPWW was observed between the freezing probabilities of the pure components, as expected (figure 5.14). Surprisingly, at a certain concentration of BPWW the freezing probability did not increase anymore. It was also impossible to increase the concentration of BPWW in the illite particles, which would be high enough to reproduce the temperature dependency of pure BPWW. Obviously, the BPWW does not coat the entire particle surface. BET measurements showed a decrease in the surface area of illite NX particles mixed with BPWW, indicating that the BPWW material was filling interstitial voids separating the illite crystalline faces. Measurements of the effective density of pure illite NX particles their mixture with BPWW have shown a slight increase for the mixed particles, which is also indicative that the BPWW material is located on the illite NX particles.

Another interesting finding was that the contact freezing probability is proportional to the particle surface. Analysis of different particle sizes at a certain temperature can be fitted very well by a function, which is proportional to the square of the particle diameter. The idea of a point contact which initializes the freezing seems to be incorrect. It seems more likely that the particle surface or the entire surface has to be involved in the freezing process. Further studies are necessary to analyze this topic. A possible approach is described in section 6.1.

In our experiments, the particle size was known very precisely, since for each aerosol material and selected mobility diameter a filter sample was taken and analyzed by SEM. From SEM images, the area equivalent diameter can be calculated and the resulting size distributions have been used to calculate the collection efficiency. The quality of size determination is indirectly supported by the fact, that the contact ice nucleation active site density for all investigated particle sizes fall together onto one line (cf. figure 5.19).

Comparing the contact freezing results with the data of heterogeneous freezing published by other research groups can be done based on the values of INAS densities.

The best match between the contact freezing data obtained in this work and other results has been found for measurements of SNOMAX® particles published recently in Niehaus et al. [2014a].

A parametrization of SNOMAX® and BPWW results following the approach suggested by the parametrization of Hartmann et al. [2013] also revealed a surface-like dependency, which indicates that part of the particle or the entire particle is involved in the freezing process. Our parametrization yields a similar number concentration of INA protein complexes for the contact freezing mode.

The existing experimental setup was improved with an electrostatic precipitator to conduct the immersion freezing experiments. In this case the droplets were allowed to collect certain numbers of INPs before the aerosol was filtered out of the gas flow. The time elapsed in the particle-free flow until the "seeded" droplet freeze was used to derive the characteristic immersion freezing rate. The contact and immersion freezing efficiency could then be compared in terms of the contact (CINAS) or immersion (INAS) surface densities. The CINAS density in the experiments with kaolinites Fluka, KGa-1b, illite NX and hematite was always higher than the INAS density (figure 5.18). Comparing with immersion freezing efficiencies reported by other research groups has shown, that the INAS densities for Illite NX [Broadley et al., 2012] and K-rich felspars [Atkinson et al., 2013] are also lower than the CINAS densities (figure 5.19). The INAS density of illite NX measured in this experimental setup is in the lower range of the INAS density of Broadley et al. [2012] and the INAS density of kaolinite KGa-1b compared to Murray et al. [2011] shows a similar result. We attribute this effect to the differences in experimental methods.

6.1 Open questions and outlook

Although considerable progress was achieved in the attempt to quantify the contact freezing mechanism, some questions remain open. The main puzzle of the contact freezing has still not been resolved, namely, the reason for contact freezing enhancement compared to other heterogeneous freezing modes. In the studies planned for the second stage of the DFG research project INUIT, we will address the following questions:

- What is the time gap between the particle contact and the initiation of freezing?
- What part of the particle surface area is involved in the freezing process?
- Do particles penetrate the surface of the droplet or do they stay "afloat"? In the latter case, do they become wetted?

Another interesting experiment work is planed with weathered feldspar particles. We saw a slight difference in the ice activity of K-feldspar particles generated from a suspension and generated from a powder. To see, there is an wash-out process

is going on, the particles can be stored in water over weeks, and the water can be changed from time to time to remove the potentially washed-out ions. If there is an out-wash process, the ice activity should degrade.

Another remaining topic is the analysis of the ice active component of BPWW, and the identification of the amount of BPWW components located on illite NX particles. My guess is, to identify the ice active component the expertise and laboratory equipment of biologists or chemists is better than the possibilities in our laboratory. The identification of the amount of BPWW components located on illite NX particles may be realized using fluorescence microscopy. We saw in section 5.5, that there is a difference in the fluorescence spectrum of pure illite NX and illite NX mixed with BPWW. Now, we have to find a way to quantify that, for example by calibrating the intensity of the spectrum.

There is still a lot to investigate, and some of these open questions will hopefully be answered in the context of the second phase of the INUIT project.

Appendix

A List of Figures

B List of Tables

C Nomenclature

χ	evaporation rate
$\Delta H_\nu \rho_w$	latent heat for water evaporation
Δh_e	molar enthalpy of evaporation
λ	thermal conductivity
Ω	surface area of the i-mer
Bi	Biot number
Kn	Knudsen number
$\mathrm{N_A}$	Avogadro number
Pr	Prandtl number
Re	Reynolds number
ρ_i	density of ice
ρ_w	density of water
ρ_w	density of water
$\sigma_{i,w}$	energy of interfaces between ice nucleus and supercooled water
$\sigma_{p,i}$	energy of interfaces between particle and ice nucleus
$\sigma_{p,w}$	energy of interfaces between particle and supercooled water
σ_w	solution surface tension
c_p	heat capacity
$D_\nu(T)$	temperature dependent diffusion coefficient of water
$D_\nu^{'}$	modified diffusivity of water vapor
d_u	diameter of insoluble particle
J	homogeneous freezing rate
J_{hom}	nucleation rate coefficient
k	Boltzmann constant
$k_a^{'}$	effective thermal conductivity of air
M_i	molar mass of ice
M_w	molecular weight of water
N_f	Number of frozen droplets
n_i	number concentration of water molecules
n_s	number of solute moles
N_u	number of unfrozen droplets

n_w number of water molecules which are in contact with the ice nucleus surface
$p^\circ(T_\infty)$ saturation vapor pressure
R the universal gas constant
S ratio of vapor pressure over water and ice
$S_{\nu,\infty}$ environmental saturation
T_∞ temperature of the environment

D Additional information

D.1 Size distribution of aerosol particles being used

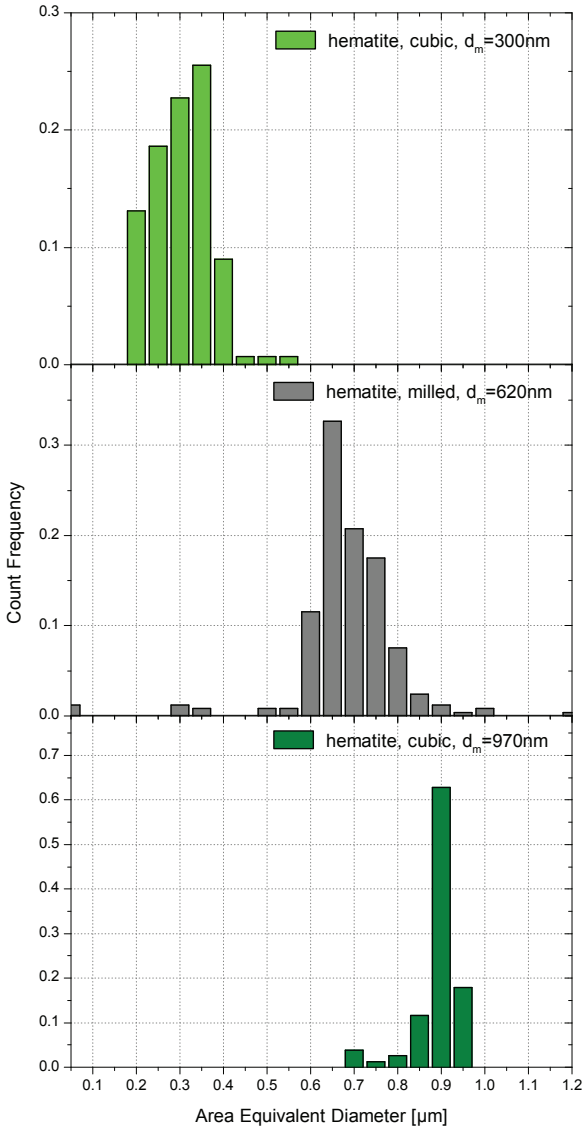

Figure D.1: Size distribution cubic and milled hematite calculated from SEM images

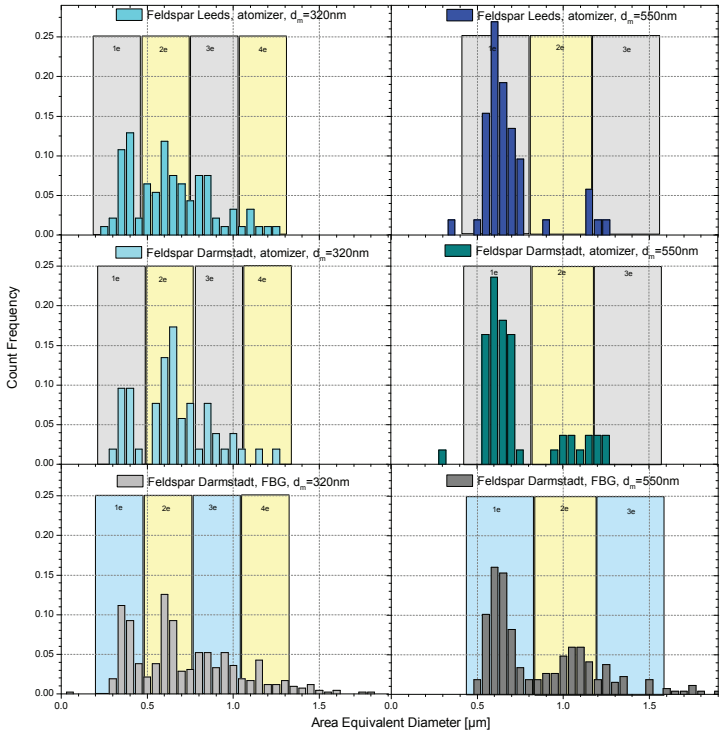

Figure D.2: Size distribution of feldspar from Darmstadt (Microcline) and Leeds (Microcline) generated by an atomizer or FBG calculated from SEM images

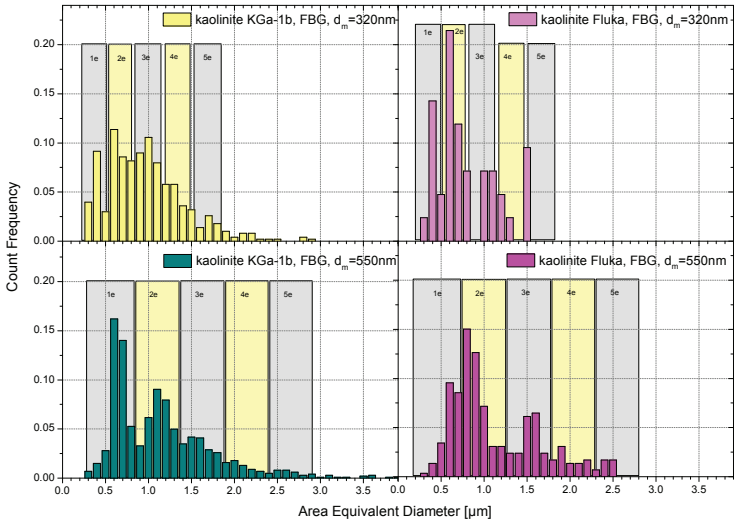

Figure D.3: Size distribution kaolinite KGa-1b and Fluka calculated from SEM images

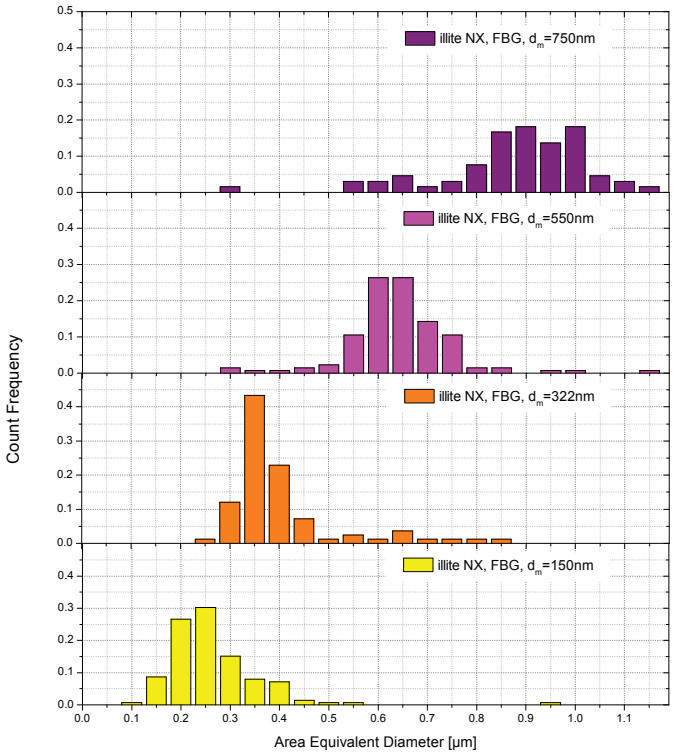

Figure D.4: Size distribution illite NX calculated from SEM images

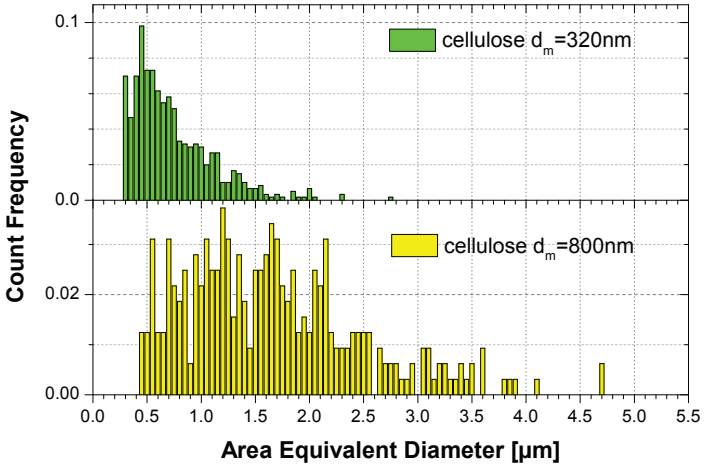

Figure D.5: Size distribution microcrystalline cellulose calculated from SEM images

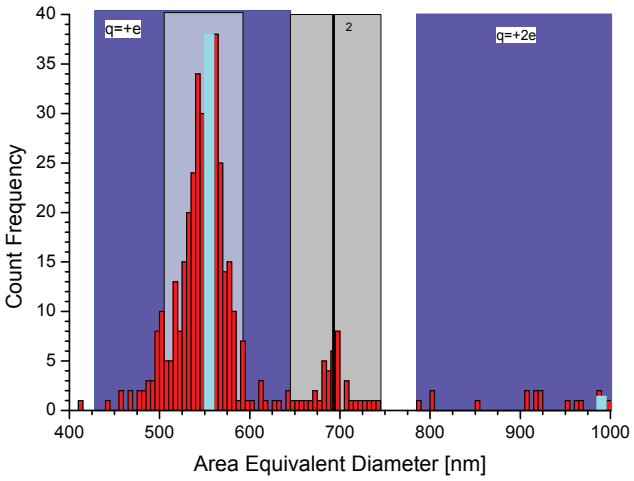

Figure D.6: Size distribution BPWW [Schäfer, 2014]. Peak at 700 nm represents the coagulation of two particles on the filter. As described in section 5.3.2 the BPWW particles have a honey-like structure. To calculate the particle diameter from SEM images, the particle is assumed as a spherical sector. The calculation of the particle diameter is described in [Schäfer, 2014]

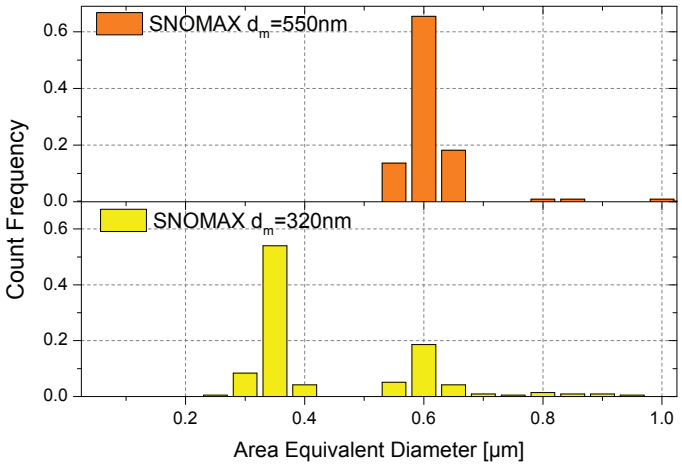

Figure D.7: Size distribution SNOMAX® calculated from SEM images

D.2 BET surface areas

Table D.1: Overview of BET surfaces (measurements courtesy of Tanja Kisely)

Material	BET surface [m^2/g]
Kaolinite KGa-1b	12.2±1
Kaolinite Fluka	8.6±1
K-feldspar Darmstadt	1.8±0.2
K-feldspar Darmstadt washed	3.0±0.3
K-feldspar Leeds	2.6±0.3
Na/Ca-feldspar Darmstadt	1.9±0.2
Illite NX	124±12

E Microscopic art

Analyzing aerosol samples with a SEM is time-consuming work. Sometimes, though, one gets rewarded with art and beauty on a very tiny scale.

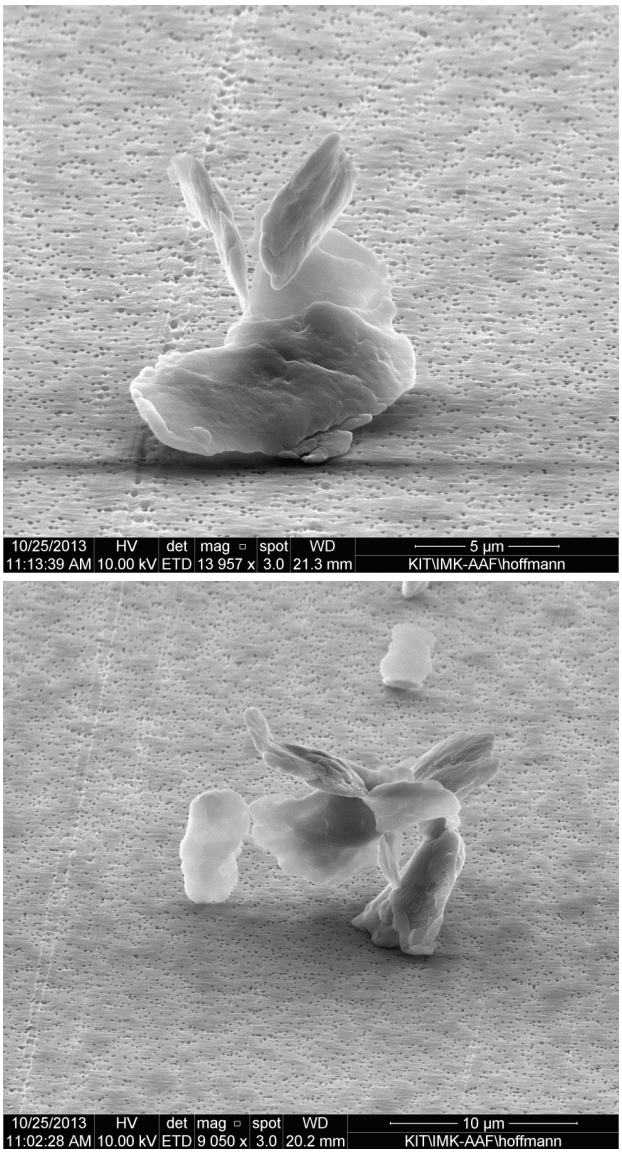

Figure E.1: Cellulose on Nuclepore® filter

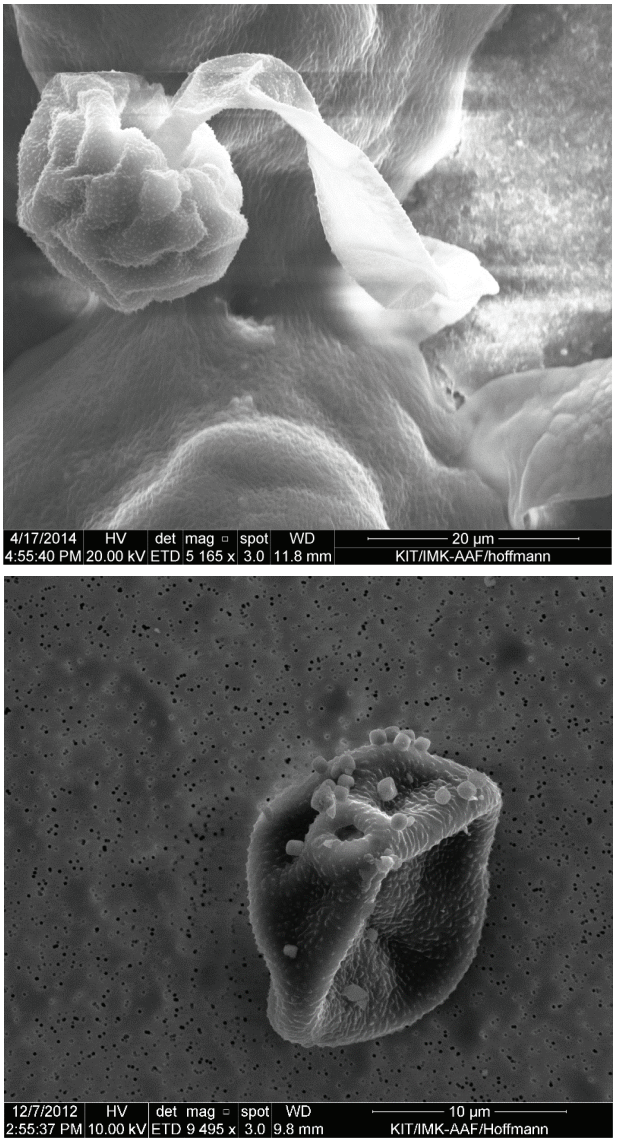

Figure E.2: top: A fungus growing on illite mixed with BPWW (not used in the experiments!), bottom: Birch pollen grain covered with cubic hematite particles on Nuclepore® filter

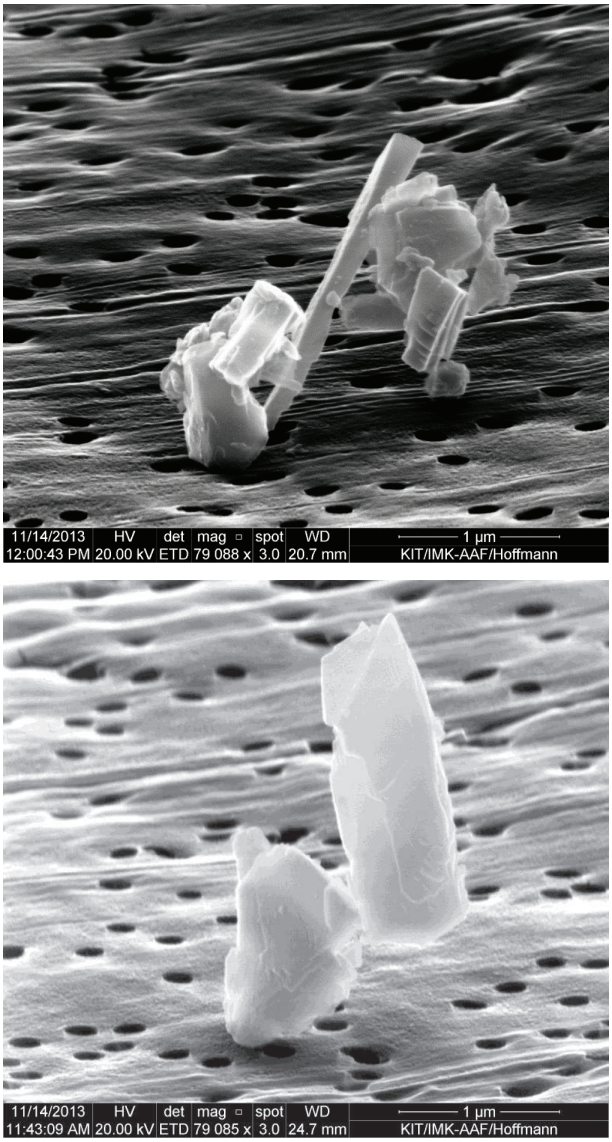

Figure E.3: Feldspar (andesine) on Nuclepore® filter

F Bibliography

Michael D. Allen and Otto G. Raabe. Slip Correction Measurements of Spherical Solid Aerosol Particles in an Improved Millikan Apparatus. *Aerosol Science and Technology*, 1985.

Albert Ansmann. Ice formation in Saharan dust over central Europe observed with temperature/humidity/aerosol Raman lidar. *Journal of Geophysical Research*, 110(D18):D18S12, 2005. ISSN 0148-0227. doi: 10.1029/2004JD005000. URL `http://doi.wiley.com/10.1029/2004JD005000`.

James D. Atkinson, Benjamin J. Murray, Matthew T. Woodhouse, Thomas F. Whale, Kelly J. Baustian, Kenneth S. Carslaw, Steven Dobbie, Daniel O'Sullivan, and Tamsin L. Malkin. The importance of feldspar for ice nucleation by mineral dust in mixed-phase clouds. *Nature*, 498(7454):355–8, July 2013. ISSN 1476-4687. doi: 10.1038/nature12278. URL `http://dx.doi.org/10.1038/nature12278`.

S. Augustin, H. Wex, D. Niedermeier, B. Pummer, H. Grothe, S. Hartmann, L. Tomsche, T. Clauss, J. Voigtländer, K. Ignatius, and F. Stratmann. Immersion freezing of birch pollen washing water. *Atmospheric Chemistry and Physics*, 13(21): 10989–11003, November 2013. ISSN 1680-7324. doi: 10.5194/acp-13-10989-2013. URL `http://www.atmos-chem-phys.net/13/10989/2013/acp-13-10989-2013.html`.

S. Augustin-Bauditz, H. Wex, S. Kanter, M. Ebert, D. Niedermeier, F. Stolz, A. Prager, and F. Stratmann. The immersion mode ice nucleation behavior of mineral dusts: A comparison of different pure and surface modified dusts. *Geophysical Research Letters*, 41(20):7375–7382, October 2014. ISSN 00948276. doi: 10.1002/2014GL061317. URL `http://doi.wiley.com/10.1002/2014GL061317`.

Hans Dieter Baehr and Karl Stephan. *Wärme- und Stoffübertragung*. Springer Vieweg, Berlin, Heidelberg, 8., aktual edition, 2013. doi: 10.1007/978-3-642-36558-4.

H.-P. Blume, G. W. Brümmer, R. Horn, E. Kandeler, I. Kögel-Knaber, R. Kretzschmar, K. Stahr, and B.-M. Wilke. *Scheffer/Schachtschabel Lehrbuch der Bodenkunde*. Spektrum, 2010.

Craig F. Bohren and Donald R. Huffman. *Absorption and Scattering of Light by Small Particles*. John Wiley & Son, New York, 1983.

S. L. Broadley, B. J. Murray, R. J. Herbert, J. D. Atkinson, S. Dobbie, T. L. Malkin, E. Condliffe, and L. Neve. Immersion mode heterogeneous ice nucleation by an illite rich powder representative of atmospheric mineral dust. *Atmospheric*

Chemistry and Physics, 12(1):287–307, January 2012. ISSN 1680-7324. doi: 10.5194/acp-12-287-2012. URL http://www.atmos-chem-phys.net/12/287/2012/acp-12-287-2012.html.

Stephen Brunauer, P. H. Emmett, and Edward Teller. Adsorption of Gases in Multimolecular Layers. *Journal of the American Chemical Society*, 60(2):309–319, February 1938. ISSN 0002-7863. doi: 10.1021/ja01269a023. URL http://dx.doi.org/10.1021/ja01269a023.

K. W. Bunker, S. China, C. Mazzoleni, A. Kostinski, and W. Cantrell. Measurements of ice nucleation by mineral dusts in the contact mode. *Atmos. Chem. Phys. Discuss.*, 12(8):20291–20309, 2012.

P. J. Connolly, O. Möhler, P. R. Field, H. Saathoff, R. Burgess, T. Choularton, and M. Gallagher. Studies of heterogeneous freezing by three different desert dust samples. *Atmospheric Chemistry and Physics*, 9(8):2805–2824, April 2009. ISSN 1680-7324. doi: 10.5194/acp-9-2805-2009. URL http://www.atmos-chem-phys.net/9/2805/2009/acp-9-2805-2009.html.

William A. Cooper. A Possible Mechanism for Contact Nucleation. *Journal of the Atmospheric Sciences*, 31(7):1832–1837, October 1974. ISSN 0022-4928. doi: 10.1175/1520-0469(1974)031<1832:APMFCN>2.0.CO;2. URL http://journals.ametsoc.org/doi/abs/10.1175/1520-0469(1974)031%3C1832%3AAPMFCN%3E2.0.CO%3B2.

J. E. Davis and G. Schweiger. *The Airborne Microparticle – Its Physics, Chemistry, Optics, and Transport Phenomena*. Springer Verlag, Berlin, 2002.

W. A. Deer, R. A. Howie, and J. Zussman. *Rock-Forming Minerals, Volume 4A: Framework Silicates - Feldspars*. Geological Society of London, Unit 7, Brassmill Enterprise Centre, Brassmill Lane, Bath BA 1 3JN, UK, 2nd edition, 2001.

Viviane R. Després, J. Alex Huffman, Susannah M. Burrows, Corinna Hoose, Aleksandr S. Safatov, Galina Buryak, Janine Fröhlich-Nowoisky, Wolfgang Elbert, Meinrat O. Andreae, Ulrich Pöschl, and Ruprecht Jaenicke. Primary biological aerosol particles in the atmosphere: a review. *Tellus B*, 64, February 2012. ISSN 1600-0889. doi: 10.3402/tellusb.v64i0.15598. URL http://www.tellusb.net/index.php/tellusb/article/view/15598/xml.

K. Diehl, S. Matthias-Maser, R. Jaenicke, and S. K. Mitra. The ice nucleating ability of pollen:. *Atmospheric Research*, 61(2):125–133, 2002. URL http://www.sciencedirect.com/science/article/pii/S0169809501001326.

Y. S. Djikaev and E. Ruckenstein. Thermodynamics of heterogeneous crystal nucleation in contact and immersion modes. *The journal of physical chemistry. A*, 112 (46):11677–87, November 2008. ISSN 1520-5215. doi: 10.1021/jp803155f. URL http://dx.doi.org/10.1021/jp803155f.

Denis Duft. *LABOREXPERIMENTE ZUR MIKROPHYSIK DER WOLKEN*. PhD thesis, Technische Universität Illmenau, 2010.

Denis Duft. Flow through the EDB simulate using CFX from ANSYS, personal communication, 2012.

Denis Duft. Simulation of the temperature field around the levitated droplet using COMSOL Multiphysics®, personal communication, 2013.

Adam J. Durant and Raymond A. Shaw. Evaporation freezing by contact nucleation inside-out. *Geophysical Research Letters*, 32(20):2–5, 2005. ISSN 0094-8276. doi: 10.1029/2005GL024175. URL `http://www.agu.org/pubs/crossref/2005/2005GL024175.shtml`.

Kensei Ehara, Charles Hagwood, and Kevin J. Coakley. Novel method to classify aerosol particles according to their mass-to-charge ratio—Aerosol particle mass analyser. *Journal of Aerosol Science*, 27(2):217–234, March 1996. ISSN 00218502. doi: 10.1016/0021-8502(95)00562-5. URL `http://www.sciencedirect.com/science/article/pii/0021850295005625`.

M. Ettner, S. K. Mitra, and S. Borrmann. Heterogeneous freezing of single sulfuric acid solution droplets: laboratory experiments utilizing an acoustic levitator. *Atmospheric Chemistry and Physics*, 4(7):1925–1932, September 2004. ISSN 1680-7324. doi: 10.5194/acp-4-1925-2004. URL `http://www.atmos-chem-phys.net/4/1925/2004/acp-4-1925-2004.html`.

N. H. Fletcher. *The physics of rainclouds*. Cambridge University Press, 1962. ISBN 978-0-521-15479-6.

N. H. Fletcher. Active sites and ice crystal nucleation. *Journal of the Atmospheric Sciences*, 26:1266–1271, 1969. URL `https://www.phys.unsw.edu.au/music/people/publications/Fletcher1969a.pdf`.

Adam P. Fornea, Sarah D. Brooks, Jeffrey B. Dooley, and Auromeet Saha. Heterogeneous freezing of ice on atmospheric aerosols containing ash, soot, and soil. *Journal of Geophysical Research*, 114(D13):D13201, July 2009. ISSN 0148-0227. doi: 10.1029/2009JD011958. URL `http://doi.wiley.com/10.1029/2009JD011958`.

N. A. Fuchs. On the stationary charge distribution on aerosol particles in a bipolar ionic atmosphere. *Pure and Applied Geophysics*, 56(1):185–193, 1963. ISSN 0033-4553.

N. Fukuta and L. A. Walter. Kinetics of hydrometer growth from a vapor-spherical model. *Journal of the Atmospheric Sciences*, 27:1160–1172, 1970.

Norihiko Fukuta. A Study of the Mechanism of Contact Ice Nucleation. *Journal of the Atmospheric Sciences*, 32(8):1597–1603, August 1975. ISSN 0022-4928. doi: 10.1175/1520-0469(1975)032<1597:ASOTMO>2.0.CO;

2. URL http://journals.ametsoc.org/doi/abs/10.1175/1520-0469(1975)032%3C1597%3AASOTMO%3E2.0.CO%3B2.

Christopher P. Garnham, Robert L. Campbell, Virginia K. Walker, and Peter L. Davies. Novel dimeric β-helical model of an ice nucleation protein with bridged active sites. *BMC structural biology*, 11(1):36, January 2011. ISSN 1472-6807. doi: 10.1186/1472-6807-11-36. URL http://www.biomedcentral.com/1472-6807/11/36.

S. N. Grover, H. R. Pruppacher, and A. E. Hamielec. A Numerical Determination of the Efficiency with Which Spherical Aerosol Particles Collide with Spherical Water Drops Due to Inertial Impaction and Phoretic and Electrical Forces. *Journal of the Atmospheric Sciences*, 34(10):1655–1663, October 1977. ISSN 0022-4928. doi: 10.1175/1520-0469(1977)034<1655:ANDOTE>2.0.CO;2. URL http://journals.ametsoc.org/doi/abs/10.1175/1520-0469(1977)034%3C1655:ANDOTE%3E2.0.CO%3B2.

Ross Gunn and R. H. Woessner. Measurements of the systematic electrification of aerosols. *Journal of Colloid Science*, 11(3):254–259, June 1956. ISSN 00958522. doi: 10.1016/0095-8522(56)90050-2. URL http://www.sciencedirect.com/science/article/pii/0095852256900502.

E Hairer, Norsett, and G S. P. Wanner. *Solving Ordinary Differential Equations I: Nonstiff Problems*. Springer, Berlin, Heidleberg, 2009.

D. E. Hare and C. M. Sorensen. The density of supercooled water. II. Bulk samples cooled to the homogeneous nucleation limit. *The Journal of Chemical Physics*, 87(8):4840, October 1987. ISSN 00219606. doi: 10.1063/1.453710. URL http://scitation.aip.org/content/aip/journal/jcp/87/8/10.1063/1.453710.

S. Hartmann, D. Niedermeier, J. Voigtländer, T. Clauss, R. A. Shaw, H. Wex, A. Kiselev, and F. Stratmann. Homogeneous and heterogeneous ice nucleation at LACIS: operating principle and theoretical studies. *Atmospheric Chemistry and Physics*, 11(4):1753–1767, February 2011. ISSN 1680-7324. doi: 10.5194/acp-11-1753-2011. URL http://www.atmos-chem-phys.net/11/1753/2011/acp-11-1753-2011.html.

S. Hartmann, S. Augustin, T. Clauss, H. Wex, T. Šantl Temkiv, J. Voigtländer, D. Niedermeier, and F. Stratmann. Immersion freezing of ice nucleation active protein complexes. *Atmospheric Chemistry and Physics*, 13(11):5751–5766, June 2013. ISSN 1680-7324. doi: 10.5194/acp-13-5751-2013. URL http://www.atmos-chem-phys.net/13/5751/2013/acp-13-5751-2013.html.

Andrew J. Heymsfield and Larry M. Miloshevich. Homogeneous Ice Nucleation and Supercooled Liquid Water in Orographic Wave Clouds. *Journal of the Atmospheric Sciences*, 50(15):2335–2353, August 1993. ISSN 0022-4928. doi: 10.1175/1520-0469(1993)050<2335:HINASL>2.0.

CO;2. URL http://journals.ametsoc.org/doi/abs/10.1175/1520-0469%281993%29050%3C2335%3AHINASL%3E2.0.CO%3B2.

William C. Hinds. *Aerosol technology : properties, behavior, and measurement of airborne particles*. A Wiley-Interscience publication. Wiley, New York [u.a.], 2. ed. edition, 1999. ISBN 0-471-19410-7. URL http://swbplus.bsz-bw.de/bsz080974201cov.htm;http://www.gbv.de/dms/ilmenau/toc/244421706.PDF.

N. Hiranuma, S. Augustin-Bauditz, H. Bingemer, C. Budke, J. Curtius, A. Danielczok, K. Diehl, K. Dreischmeier, M. Ebert, F. Frank, N. Hoffmann, K. Kandler, A. Kiselev, T. Koop, T. Leisner, O. Möhler, B. Nillius, A. Peckhaus, D. Rose, S. Weinbruch, H. Wex, Y. Boose, P. J. DeMott, J. D. Hader, T. C. J. Hill, Z. A. Kanji, G. Kulkarni, E. J. T. Levin, C. S. McCluskey, M. Murakami, B. J. Murray, D. Niedermeier, M. D. Petters, D. O'Sullivan, A. Saito, G. P. Schill, T. Tajiri, M. A. Tolbert, A. Welti, T. F. Whale, T. P. Wright, and K. Yamashita. A comprehensive laboratory study on the immersion freezing behavior of illite NX particles: a comparison of seventeen ice nucleation measurement techniques. *Atmospheric Chemistry and Physics Discussions*, 14(15):22045–22116, August 2014a. ISSN 1680-7367. doi: doi:10.5194/acpd-14-22045-2014. URL http://www.atmos-chem-phys-discuss.net/14/22045/2014/acpd-14-22045-2014.html.

N. Hiranuma, N. Hoffmann, A. Kiselev, A. Dreyer, K. Zhang, G. Kulkarni, T. Koop, and O. Möhler. Influence of surface morphology on the immersion mode ice nucleation efficiency of hematite particles. *Atmospheric Chemistry and Physics*, 14 (5):2315–2324, March 2014b. ISSN 1680-7324. doi: 10.5194/acp-14-2315-2014. URL http://www.atmos-chem-phys.net/14/2315/2014/acp-14-2315-2014.html.

N. Hiranuma, O. Möhler, K. Yamashita, T. Tajiri, A. Saito, A. Kiselev, N. Hoffmann, C. Hoose, E. Jantsch, T. Koop, and M. Murakami. Ice nucleation by cellulose and its potential contribution to ice formation in clouds. *Nature Geoscience submitted*, 2015.

Peter V. Hobbs and Arthur L. Rangno. Ice Particle Concentrations in Clouds. *Journal of the Atmospheric Sciences*, 42(23):2523–2549, December 1985. ISSN 0022-4928. doi: 10.1175/1520-0469(1985)042<2523:IPCIC>2.0.CO;2. URL http://journals.ametsoc.org/doi/abs/10.1175/1520-0469(1985)042%3C2523:IPCIC%3E2.0.CO;2.

N. Hoffmann, A. Kiselev, D. Rzesanke, D. Duft, and T. Leisner. Experimental quantification of contact freezing in an electrodynamic balance. *Atmospheric Measurement Techniques*, 6(9):2373–2382, September 2013a. ISSN 1867-8548. doi: 10.5194/amt-6-2373-2013. URL http://www.atmos-meas-tech.net/6/2373/2013/amt-6-2373-2013.html.

Nadine Hoffmann. Laborexperiment zum Kontaktgefrieren unterkühlter Wolkentropfen, diploma thesis, 2012.

Nadine Hoffmann, Denis Duft, Alexei Kiselev, and Thomas Leisner. Contact freezing efficiency of mineral dust aerosols studied in an electrodynamic balance: quantitative size and temperature dependence for illite particles. *Faraday Discussions*, 165:383, December 2013b. ISSN 1359-6640. doi: 10.1039/c3fd00033h. URL http://pubs.rsc.org/en/content/articlehtml/2013/fd/c3fd00033h.

C. Hoose and O. Möhler. Heterogeneous ice nucleation on atmospheric aerosols: a review of results from laboratory experiments. *Atmospheric Chemistry and Physics*, 12(20):9817–9854, October 2012. ISSN 1680-7324. doi: 10.5194/acp-12-9817-2012. URL http://www.atmos-chem-phys.net/12/9817/2012/acp-12-9817-2012.html.

Corinna Hoose, Jón Egill Kristjánsson, Jen-Ping Chen, and Anupam Hazra. A Classical-Theory-Based Parameterization of Heterogeneous Ice Nucleation by Mineral Dust, Soot, and Biological Particles in a Global Climate Model. *Journal of the Atmospheric Sciences*, 67(8):2483–2503, August 2010. ISSN 0022-4928. doi: 10.1175/2010JAS3425.1. URL http://journals.ametsoc.org/doi/abs/10.1175/2010JAS3425.1.

Hui-Ming Hung, Adam Malinowski, and Scot T. Martin. Kinetics of Heterogeneous Ice Nucleation on the Surfaces of Mineral Dust Cores Inserted into Aqueous Ammonium Sulfate Particles. *The Journal of Physical Chemistry A*, 107(9):1296–1306, March 2003. ISSN 1089-5639. doi: 10.1021/jp021593y. URL http://dx.doi.org/10.1021/jp021593y.

Kazuhiko Kandori, Naoko Yamamoto, Akemi Yasukawa, and Tatsuo Ishikawa. Preparation and characterization of disk-shaped hematite particles by a forced hydrolysis reaction in the presence of polyvinyl alcohol. *Physical Chemistry Chemical Physics*, 4(24):6116–6122, November 2002. ISSN 14639076. doi: 10.1039/b206095g. URL http://pubs.rsc.org/en/content/articlehtml/2002/cp/b206095g.

Aerosol Particle Mass Analyzer Model 3601 APM-II. Kanomax, Kanomax USA, Inc., 219 US Highway. 206, Andover, New Jersey 07821, 2013.

Jung Hyeun Kim, George W. Mulholland, Scott R. Kukuck, and David Y. H. Pui. Slip correction measurements of certified psl nanoparticles using a nanometer differential mobility analyzer (nano-dma) for knudsen number from 0.5 to 83. *Journal of Research of the National Institute of Standards and Technology*, 110(1), 2005. URL http://dx.doi.org/10.6028/jres.110.005.

Michael Koch. Laborexperimente zum Kontaktgefrieren unterkühlter Wassertropfen, Bachelor's thesis, 2014.

Herbert F. Kraemer and H. F. Johnstone. Collection of Aerosol Particles in Presence of Electrostatic Fields. *Industrial & Engineering Chemistry*, 47(12):2426–2434, 1955.

L. Ladino, O. Stetzer, F. Lüönd, A. Welti, and U. Lohmann. Contact freezing experiments of kaolinite particles with cloud droplets. *Journal of Geophysical Research*, 116(D22):D22202, November 2011a. ISSN 0148-0227. doi: 10.1029/2011JD015727. URL http://doi.wiley.com/10.1029/2011JD015727.

Luis Ladino, Olaf Stetzer, Bodo Hattendorf, Detlef Günther, Betty Croft, and Ulrike Lohmann. Experimental Study of Collection Efficiencies between Submicron Aerosols and Cloud Droplets. *Journal of the Atmospheric Sciences*, 68(9):1853–1864, September 2011b. ISSN 0022-4928. doi: 10.1175/JAS-D-11-012.1. URL http://journals.ametsoc.org/doi/abs/10.1175/JAS-D-11-012.1.

L. A. Ladino Moreno, O. Stetzer, and U. Lohmann. Contact freezing: a review of experimental studies. *Atmospheric Chemistry and Physics*, 13(19):9745–9769, October 2013. ISSN 1680-7324. doi: 10.5194/acp-13-9745-2013. URL http://www.atmos-chem-phys.net/13/9745/2013/acp-13-9745-2013.html.

Zev Levin and Saul A. Yankofsky. Contact Versus Immersion Freezing of Freely Suspended Droplets by Bacterial Ice Nuclei. *Journal of Climate and Applied Meteorology*, 22(11):1964–1966, November 1983. ISSN 0733-3021. doi: 10.1175/1520-0450(1983)022<1964:CVIFOF>2.0.CO;2. URL http://journals.ametsoc.org/doi/abs/10.1175/1520-0450(1983)022%3C1964:CVIFOF%3E2.0.CO%3B2.

F. Lüönd, O. Stetzer, A. Welti, and U. Lohmann. Experimental study on the ice nucleation ability of size-selected kaolinite particles in the immersion mode. *Journal of Geophysical Research*, 115(D14):D14201, July 2010. ISSN 0148-0227. doi: 10.1029/2009JD012959. URL http://doi.wiley.com/10.1029/2009JD012959.

Horst Malberg. *Meteorologie und Klimatologie - Eine Einführung*. Springer, 2007.

B. J. Mason. *The physics of clouds*. Oxford: Clarendon Press, 1971.

Mathias Metz Metzler. Thermodynamic assesment of the cellulosic ethanol alternative energy system, October 2014. URL http://www.facstaff.bucknell.edu/mvigeant/thermo_demos/mathiasmetzmetzler/pages/system.htm.

O. Möhler, P. J. DeMott, G. Vali, and Z. Levin. Microbiology and atmospheric processes: the role of biological particles in cloud physics. *Biogeosciences*, 4(6):1059–1071, December 2007. ISSN 1726-4189. doi: 10.5194/bg-4-1059-2007. URL http://www.biogeosciences.net/4/1059/2007/bg-4-1059-2007.html.

O. Möhler, D. G. Georgakopoulos, C. E. Morris, S. Benz, V. Ebert, S. Hunsmann, H. Saathoff, M. Schnaiter, and R. Wagner. Heterogeneous ice nucleation activity of bacteria: new laboratory experiments at simulated cloud conditions. *Biogeosciences*, 5(5):1425–1435, October 2008. ISSN 1726-4189. doi: 10.5194/bg-5-1425-2008. URL http://www.biogeosciences.net/5/1425/2008/bg-5-1425-2008.html.

C. E. Morris, D. G. Georgakopoulos, and D. C. Sands. Ice nucleation active bacteria and their potential role in precipitation. *Journal de Physique IV (Proceedings)*, 121:87–103, December 2004. ISSN 1155-4339. doi: 10.1051/jp4:2004121004. URL http://dx.doi.org/10.1051/jp4:2004121004.

B. J. Murray, S. L. Broadley, T. W. Wilson, J. D. Atkinson, and R. H. Wills. Heterogeneous freezing of water droplets containing kaolinite particles. *Atmospheric Chemistry and Physics*, 11(9):4191–4207, May 2011. ISSN 1680-7324. doi: 10.5194/acp-11-4191-2011. URL http://www.atmos-chem-phys.net/11/4191/2011/.

George Némethy and Harold A. Scheraga. Structure of Water and Hydrophobic Bonding in Proteins. IV. The Thermodynamic Properties of Liquid Deuterium Oxide. *The Journal of Chemical Physics*, 41(3):680, 1964. ISSN 00219606. doi: 10.1063/1.1725946. URL http://link.aip.org/link/JCPSA6/v41/i3/p680/s1&Agg=doi.

Joseph Niehaus, Jennifer G. Becker, Alexander Kostinski, and Will Cantrell. Laboratory Measurements of Contact Freezing by Dust and Bacteria at Temperatures of Mixed-Phase Clouds. *Journal of the Atmospheric Sciences*, 71(10):3659–3667, October 2014a. ISSN 0022-4928. doi: 10.1175/JAS-D-14-0022.1. URL http://journals.ametsoc.org/doi/abs/10.1175/JAS-D-14-0022.1.

Joseph Niehaus, Kristopher W. Bunker, Swarup China, Alexander Kostinski, Claudio Mazzoleni, and Will Cantrell. A Technique to Measure Ice Nuclei in the Contact Mode. *Journal of Atmospheric and Oceanic Technology*, 31(4):913–922, April 2014b. ISSN 0739-0572. doi: 10.1175/JTECH-D-13-00156.1. URL http://journals.ametsoc.org/doi/abs/10.1175/JTECH-D-13-00156.1.

Wolfgang Nolting. *Grundkurs Theoretische Physik 4; Spezielle Relativitätstheorie, Thermodynamik*. Springer, 2012.

M Oettel and S Dietrich. Colloidal interactions at fluid interfaces. *Langmuir : the ACS journal of surfaces and colloids*, 24(4):1425–41, February 2008. ISSN 0743-7463. doi: 10.1021/la702794d. URL http://dx.doi.org/10.1021/la702794d.

Martin Okrusch. *Mineralogie : Eine Einführung in die spezielle Mineralogie, Petrologie und Lagerstättenkunde*. Springer Spektrum, Berlin, Heidelberg, 9., vollst. überarb. u. akt. aufl. 2014 edition, 2014. ISBN 978-364-23466-0-6.

C. Orser, B. J. Staskawicz, N. J. Panopoulos, D. Dahlbeck, and S. E. Lindow. Cloning and expression of bacterial ice nucleation genes in Escherichia coli. *J. Bacteriol.*, 164(1):359–366, October 1985. URL http://jb.asm.org/content/164/1/359.short.

Vaughan T. J. Philips, Leo J. Donner, and Stephen T. Garner. Nucleation Processes in Deep Convection Simulated by a Cloud-System-Resolving Model with Double-Moment Bulk Microphysics. *Journal of the Atmospheric Sciences*, 64(3):738–761,

March 2007. ISSN 0022-4928. doi: 10.1175/JAS3869.1. URL http://journals.ametsoc.org/doi/abs/10.1175/JAS3869.1.

R. L. Pitter and H. R. Pruppacher. A wind tunnel investigation of freezing of small water drops falling at terminal velocity in air. *Quarterly Journal of the Royal Meteorological Society*, 099(421):540–550, July 1973. ISSN 1477870X. doi: 10.1256/smsqj.42110. URL http://www.ingentaselect.com/rpsv/cgi-bin/cgi?ini=xref&body=linker&reqdoi=10.1256/smsqj.42110.

C. Pöhlker, J. A. Huffman, J.-D. Förster, and U. Pöschl. Autofluorescence of atmospheric bioaerosols: spectral fingerprints and taxonomic trends of pollen. *Atmospheric Measurement Techniques*, 6(12):3369–3392, December 2013. ISSN 1867-8548. doi: 10.5194/amt-6-3369-2013. URL http://www.atmos-meas-tech.net/6/3369/2013/amt-6-3369-2013.html.

H. R. Pruppacher and J. D. Klett. *Microphysics of Clouds and Precipitation*. Kluwer Academic Publisher, 2004.

B. G. Pummer, H. Bauer, J. Bernardi, S. Bleicher, and H. Grothe. Suspendable macromolecules are responsible for ice nucleation activity of birch and conifer pollen. *Atmospheric Chemistry and Physics*, 12(5):2541–2550, March 2012. ISSN 1680-7324. doi: 10.5194/acp-12-2541-2012. URL http://www.atmos-chem-phys.net/12/2541/2012/acp-12-2541-2012.html.

Hans Puxbaum and Monika Tenze-Kunit. Size distribution and seasonal variation of atmospheric cellulose. *Atmospheric Environment*, 37(26):3693–3699, August 2003. ISSN 13522310. doi: 10.1016/S1352-2310(03)00451-5. URL http://www.sciencedirect.com/science/article/pii/S1352231003004515.

Arthur L. Rangno and Peter V. Hobbs. Ice particle concentrations and precipitation development in small polar maritime cumuliform clouds. *Quarterly Journal of the Royal Meteorological Society*, 117(497):207–241, January 1991. ISSN 00359009. doi: 10.1002/qj.49711749710. URL http://doi.wiley.com/10.1002/qj.49711749710.

Walter Rau. Über die Wirkungsweise der Gefrierkerne im unterkühlten Wasser. *Zeitschrift für Naturforschung*, 5:667–675, 1950. URL http://zfn.mpdl.mpg.de/data/Reihe_A/5/ZNA-1950-5a-0667.pdf.

Robert J. Pruett and Harold L. Webb. Sampling and Analysis of KGa-1B Well-Chrystallized Kaolin Source Clay. *Clay and Clay Minerals*, 41(4):514–519, 1993.

Walter Roedel. *Physik unserer Umwelt – Die Atmosphäre*. Springer Verlag, Heidelberg, 2000.

Roddy R. Rogers and Man K. Yau. *A short course in cloud physics*. International series in natural philosophy ; 113. Butterworth Heinemann, [Woburn, Mass.], 3. ed., reprint. edition, 1996. ISBN 0-7506-3215-1.

Daniel Rzesanke. *Laborexperiment zum Einfluss elektrischer Ladungen auf Wolkenprozesse*. PhD thesis, Technische Universität Illmenau, 2012.

Murry L. Salby. *Physics of the Atmosphere and Climate*. Cambridge University Press, 2012. ISBN 978-0-521-76718-7.

Asunción Sánchez-Ochoa, Anne Kasper-Giebl, Hans Puxbaum, Andras Gelencser, Michel Legrand, and Casimiro Pio. Concentration of atmospheric cellulose: A proxy for plant debris across a west-east transect over Europe. *Journal of Geophysical Research*, 112(D23):D23S08, August 2007. ISSN 0148-0227. doi: 10.1029/2006JD008180. URL http://doi.wiley.com/10.1029/2006JD008180.

Manfred Schäfer. Kontaktgefrierexperiment mit biologischen Partikeln an unterkühlten Wassertröpfchen, diploma thesis, 2014.

Christina Schmidt. Morphologische Charakterisierung eisaktiver Aerosolpartikel, Bachelor's thesis, 2013.

K. H. Schmitt. Untersuchungen an Schwebstoffteilchen in diffundierendem Wasserdampf. *Zeitschrift für Naturforschung*, 16a:144–149, 1961.

Stefan Schorn et al. Mineralienatlas - Fossilienatlas, October 2014. URL http://www.mineralienatlas.de.

P. Seifert, A. Ansmann, S. Groß, V. Freudenthaler, B. Heinold, A. Hiebsch, I. Mattis, J. Schmidt, F. Schnell, M. Tesche, U. Wandinger, and M. Wiegner. Ice formation in ash-influenced clouds after the eruption of the Eyjafjallajökull volcano in April 2010. *Journal of Geophysical Research*, 116:D00U04, September 2011. ISSN 0148-0227. doi: 10.1029/2011JD015702. URL http://doi.wiley.com/10.1029/2011JD015702.

John H. Seinfeld and Spyros N. Pandis. *Atmospheric chemistry and physics : from air pollution to climate change*. Wiley, Hoboken, NJ, 2. ed. edition, 2006. ISBN 0-471-72018-6; 0-471-72017-8; 978-0-471-72017-1; 978-0-471-72018-8. URL http://swbplus.bsz-bw.de/bsz256623341cov.htm;http://www.gbv.de/dms/goettingen/50408920X.pdf. Previous ed.: 1998.

Gautam Sen. *Petrology : Principles and Practice*. SpringerLink : Bücher. Springer, Berlin, Heidelberg, 2014. ISBN 978-364-23880-0-2. URL http://dx.doi.org/10.1007/978-3-642-38800-2.

Jianying Shang, Markus Flury, James B Harsh, and Richard L Zollars. Comparison of different methods to measure contact angles of soil colloids. *Journal of colloid and interface science*, 328(2):299–307, December 2008. ISSN 1095-7103. doi: 10.1016/j.jcis.2008.09.039. URL http://www.sciencedirect.com/science/article/pii/S0021979708011612.

Raymond A. Shaw and Dennis Lamb. Experimental determination of the thermal accommodation and condensation coefficients of water. *The Journal of Chemical Physics*, 111(23):10659, December 1999. ISSN 00219606. doi: 10.1063/1.480419. URL http://scitation.aip.org/content/aip/journal/jcp/111/23/10.1063/1.480419.

Raymond A. Shaw, Adam J. Durant, and Youshi Mi. Heterogeneous Surface Crystallization Observed in Undercooled Water. *The Journal of Physical Chemistry B*, 109:9865–9868, 2005. URL http://pubs.acs.org/doi/pdfplus/10.1021/jp0506336.

W. G. N. Slinn and J. M. Hales. A Reevaluation of the Role of Thermophoresis as a Mechanism of In- and Below-Cloud Scavenging. *Journal of the Atmospheric Sciences*, 28(8):1465–1471, November 1971. ISSN 0022-4928. doi: 10.1175/1520-0469(1971)028<1465:AROTRO>2.0.CO;2. URL http://journals.ametsoc.org/doi/abs/10.1175/1520-0469(1971)028%3C1465%3AAROTRO%3E2.0.CO%3B2.

Chris Somerville. Cellulose synthesis in higher plants. *Annual review of cell and developmental biology*, 22:53–78, January 2006. ISSN 1081-0706. doi: 10.1146/annurev.cellbio.22.022206.160206. URL http://www.annualreviews.org/doi/abs/10.1146/annurev.cellbio.22.022206.160206.

P. Squires. Penetrative Downdraughts in Cumuli. *Tellus A*, 10(3):381–389, 1958. doi: DOI:10.1111/j.2153-3490.1958.tb02025.x.

Björn Steiner, Burkhard Berge, Ralf Gausmann, Jens Rohmann, and Eckart Rühl. Fast in situ Sizing Technique for Single Levitated Liquid Aerosols. *Applied Optics*, 38(9):1523, March 1999. doi: 10.1364/AO.38.001523. URL http://ao.osa.org/abstract.cfm?URI=ao-38-9-1523.

Olaf Stetzer, Björn Baschek, Felix Lüönd, and Ulrike Lohmann. The Zurich Ice Nucleation Chamber (ZINC)-A New Instrument to Investigate Atmospheric Ice Formation. *Aerosol Science and Technology*, 42(1):64–74, January 2008. ISSN 0278-6826. doi: 10.1080/02786820701787944. URL http://dx.doi.org/10.1080/02786820701787944.

Peter Stöckel. *Untersuchung der homogenen Nukleation in levitierten Tröpfchen aus stark unterkühltem H2O und D2O*. PhD thesis, Freie Universität Berlin, 2001.

T.F. Stocker, D. Qin, G.-K. Plattner, M. Tignor, S.K. Allen, J. Boschung, A. Nauels, Y. Xia, V. Bex, and P.M. Midgley, editors. *Summary for Policymakers*. Cambridge University Press, Cambridge, United Kingdom and New York, NY, USA, 2013. doi: 10.1017/CBO9781107415324.004.

Tadao Sugimoto and Kazuo Sakata. Preparation of monodisperse pseudocubic α-Fe2O3 particles from condensed ferric hydroxide gel. *Journal of Colloid and Interface Science*, 152(2):587–590, September 1992. ISSN 00219797. doi: 10.

1016/0021-9797(92)90062-Q. URL http://www.sciencedirect.com/science/article/pii/002197979290062Q.

Changquan Calvin Sun. True density of microcrystalline cellulose. *Journal of pharmaceutical sciences*, 94(10):2132–4, October 2005. ISSN 0022-3549. doi: 10.1002/jps.20459. URL http://www.ncbi.nlm.nih.gov/pubmed/16136576.

E. A. Svensson, C. Delval, P. von Hessberg, M. S. Johnson, and J. B. C. Pettersson. Freezing of water droplets colliding with kaolinite particles. *Atmospheric Chemistry and Physics*, 9:4295–4300, January 2009. ISSN 1680-7375. doi: 10.5194/acp-9-4295-2009.

Daniel C. Taflin, S. H. Zhang, Theresa Allen, and E. James Davis. Measurement of droplet interfacial phenomena by light-scattering techniques. *AIChE Journal*, 34(8):1310–1320, August 1988. doi: 10.1002/aic.690340809. URL http://doi.wiley.com/10.1002/aic.690340809.

Karl Terzaghi, Ralph B. Peck, and Gholamreza Mesri. *Soil Mechanics in Engineering Practice*. 3rd edition, 1996. ISBN 978-0-471-08658-1.

Kevin E. Trenberth, John T. Fasullo, and Jeffrey Kiehl. Earth's Global Energy Budget. *Bulletin of the American Meteorological Society*, 90(3):311–323, March 2009. ISSN 0003-0007. doi: 10.1175/2008BAMS2634.1. URL http://journals.ametsoc.org/doi/abs/10.1175/2008BAMS2634.1.

Electrostatic Classifiers Model 3080-Series. TSI, TSI Incorporated, 500 Cardigan Road, Shoreview, MN 55126, USA, 2001.

Ultrafine Condensation Particle Counter Model 3776. TSI, TSI Incorporated, 500 Cardigan Road, Shoreview, MN 55126, USA, 2007.

Cynthia H. Twohy, Paul J. DeMott, Kerri A. Pratt, R. Subramanian, Gregory L. Kok, Shane M. Murphy, Traci Lersch, Andrew J. Heymsfield, Zhien Wang, Kim A. Prather, and John H. Seinfeld. Relationships of Biomass-Burning Aerosols to Ice in Orographic Wave Clouds. *Journal of the Atmospheric Sciences*, 67(8): 2437–2450, August 2010. ISSN 0022-4928. doi: 10.1175/2010JAS3310.1. URL http://journals.ametsoc.org/doi/abs/10.1175/2010JAS3310.1.

G. Vali. Nucleation Terminology. *Bulletin of the American Meterological Society*, 66: 1426–1427, 1985.

G. Vali, P. DeMott, O. Möhler, and T. F. Whale. Ice nucleation terminology. *Atmospheric Chemistry and Physics Discussions*, 14(15):22155–22162, 2014. doi: 10.5194/acpd-14-22155-2014. URL http://www.atmos-chem-phys-discuss.net/14/22155/2014/.

N. B. Vargaftik. *Handbook of Physical Properties of Liquids and Gases*. Hemisphere Pub. Corp., Washington, 2nd edition, 1983.

N. B. Vargaftik, B. N. Volkov, and L. D. Voljak. International Tables of the Surface Tension of Water. *Journal of Physical and Chemical Reference Data*, 12(3):817–820, 1983.

Roland Vinx. *Gesteinsbestimmung im Gelände*. Spektrum-Akad.-Verl., Heidelberg, 4. aufl. edition, 2015. ISBN 978-3-642-55417-9.

Max Volmer. *Kinetik der Phasenübergänge*. Th. Steinkopff Dresden, 1939.

Nadine von Blohn, Subir K. Mitra, Karoline Diehl, and Stephan Borrmann. The ice nucleating ability of pollen. *Atmospheric Research*, 78(3-4):182–189, December 2005. ISSN 01698095. doi: 10.1016/j.atmosres.2005.03.008. URL `http://www.sciencedirect.com/science/article/pii/S0169809505001341`.

Peter Warneck. *Chemistry of the Natural Atmosphere*. Academic Press, 2000.

A. Welti, F. Lüönd, O. Stetzer, and U. Lohmann. Influence of particle size on the ice nucleating ability of mineral dusts. *Atmospheric Chemistry and Physics*, 9(18): 6705–6715, September 2009. ISSN 1680-7324. doi: 10.5194/acp-9-6705-2009. URL `http://www.atmos-chem-phys.net/9/6705/2009/acp-9-6705-2009.html`.

H. Wex, S. Augustin-Bauditz, Y. Boose, C. Budke, J. Curtius, K. Diehl, A. Dreyer, F. Frank, S. Hartmann, N. Hiranuma, E. Jantsch, Z. A. Kanji, A. Kiselev, T. Koop, O. Möhler, D. Niedermeier, B. Nillius, M. Rösch, D. Rose, C. Schmidt, I. Steinke, and F. Stratmann. Intercomparing different devices for the investigation of ice nucleating particles using Snomax®, as test substance. *Atmospheric Chemistry and Physics*, 15(3):1463–1485, February 2015. ISSN 1680-7324. doi: 10.5194/acp-15-1463-2015. URL `http://www.atmos-chem-phys.net/15/1463/2015/acp-15-1463-2015.html`.

Stephen Whitaker. Forced convection heat transfer correlations for flow in pipes, past flat plates, single cylinders, single spheres, and for flow in packed beds and tube bundles. *AIChE Journal*, 18(2):361–371, March 1972. ISSN 0001-1541. doi: 10.1002/aic.690180219. URL `http://doi.wiley.com/10.1002/aic.690180219`.

A. Wiedensohler and H. J. Fissan. Aerosol charging in high purity gases. *Journal of Aerosol Science*, 19(7):867–870, January 1988. ISSN 00218502. doi: 10.1016/0021-8502(88)90054-7. URL `http://www.sciencedirect.com/science/article/pii/0021850288900547`.

A. Wiedensohler, E. Lütkemeier, M. Feldpausch, and C. Helsper. Investigation of the bipolar charge distribution at various gas conditions. *Journal of Aerosol Science*, 17(3):413–416, January 1986. ISSN 00218502. doi: 10.1016/0021-8502(86)90118-7. URL `http://www.sciencedirect.com/science/article/pii/0021850286901187`.

Martin Wild, Doris Folini, Christoph Schär, Norman Loeb, EllsworthG. Dutton, and Gert König-Langlo. The global energy balance from a surface perspective. *Climate Dynamics*, 40(11-12):3107–3134, 2013. ISSN 0930-7575. doi: 10.1007/s00382-012-1569-8. URL http://dx.doi.org/10.1007/s00382-012-1569-8.

P. K. Wolber, C. A. Deininger, M. W. Southworth, J. Vandekerckhove, M. van Montagu, and G. J. Warren. Identification and purification of a bacterial ice-nucleation protein. *Proceedings of the National Academy of Sciences*, 83(19): 7256–7260, October 1986. ISSN 0027-8424. doi: 10.1073/pnas.83.19.7256. URL http://www.pnas.org/content/83/19/7256.short.

Paul Wolber and Gareth Warren. Bacterialice-nucleation proteins. *Trends in Biochemical Sciences*, 14(5):179–182, May 1989. ISSN 09680004. doi: 10.1016/0968-0004(89)90270-3. URL http://www.sciencedirect.com/science/article/pii/0968000489902703.

J. D. Yakobi-Hancock, L. A. Ladino, and J. P. D. Abbatt. Feldspar minerals as efficient deposition ice nuclei. *Atmospheric Chemistry and Physics*, 13(22):11175–11185, November 2013. ISSN 1680-7324. doi: 10.5194/acp-13-11175-2013. URL http://www.atmos-chem-phys.net/13/11175/2013/acp-13-11175-2013.html.

Kenneth C. Young. The role of contact nucleation in ice phase initiation in clouds. *Journal of the Atmospheric Sciences*, 31:768–776, 1974.

Frank Zimmermann, Martin Ebert, Annette Worringen, Lothar Schütz, and Stephan Weinbruch. Environmental scanning electron microscopy (ESEM) as a new technique to determine the ice nucleation capability of individual atmospheric aerosol particles. *Atmospheric Environment*, 41(37):8219–8227, December 2007. ISSN 13522310. doi: 10.1016/j.atmosenv.2007.06.023. URL http://www.sciencedirect.com/science/article/pii/S1352231007005882.

Frank Zimmermann, Stephan Weinbruch, Lothar Schütz, Heiko Hofmann, Martin Ebert, Konrad Kandler, and Annette Worringen. Ice nucleation properties of the most abundant mineral dust phases. *Journal of Geophysical Research*, 113(D23): D23204, December 2008. ISSN 0148-0227. doi: 10.1029/2008JD010655. URL http://doi.wiley.com/10.1029/2008JD010655.

B. Zobrist, T. Koop, B. P. Luo, C. Marcolli, and T. Peter. Heterogeneous Ice Nucleation Rate Coefficient of Water Droplets Coated by a Nonadecanol Monolayer. *Journal of Physical Chemistry C*, 111(5):2149–2155, February 2007. ISSN 1932-7447. doi: 10.1021/jp066080w. URL http://pubs.acs.org/cgi-bin/doilookup/?10.1021/jp066080w.

G Acknowledgements

First, I would like to thank the German Research Society (DFG) under contract MO668/4-1 and FOR 1525 INUIT for funding the phd position, and I would like to thank the following people for technical support:

Tanja Kisely (Institute for Nuclear Waste Disposal, KIT) for BET measurements, which were very helpful, Sarah Jäger for synthesizing hematite particles, Prof. Dr. Dagmar Gerthsen (Laboratory for Electron Microscopy, KIT) for providing an Environmental Scanning Electron Microscope, and Volker Zibat and Dr. Alexei Kiselev for teaching me how to use it, Dr. Masanari Takamiya and Maryam Rastegar (Institute of Toxicology and Genetics, KIT) for providing the Confocal Fluorescence Microscope and their support in applying it to this work, as well as Artiom Skripka for doing the microscope analyses, and Jens Nadolny for providing the voltage supply and LabView control of the electrostatic precipitator.

An dieser Stelle möchte ich mich herzlich bei Prof. Dr. Leisner für die Möglichkeit bedanken eine Doktorarbeit am Institut für Meteorologie und Klimaforschung – Atmosphärische Aerosolforschung schreiben zu dürfen und seine Rolle als Erstgutachter. Dank geht auch an Prof. Dr. Pfeilsticker der sich bereit erklärt hat als Zweitgutachter zu fungieren. Ein großes Dankeschön geht auch an Dr. Alexei Kiselev für die Betreuung der Doktorarbeit, die vielen hilfreichen Diskussionen und die Möglichkeit neben den Kontaktgefrierexperimenten auch die Benutzung eines SEM zu erlernen.

Vielen Dank auch an Dr. Daniel Rzesanke, der leider schon zu Beginn meiner Doktorandenzeit das Institut verlassen hat, aber ohne dessen „Vorarbeit“ und Unterstützung schon während meiner Diplomandenzeit die Doktorandenzeit nicht so problemlos hätte starten können. Für die große Unterstützung bei LabView-Problemen möchte ich mich bei Dr. Denis Duft und Jens Nadolny bedanken, sowie bei allen Mitarbeitern des IMK-AAF für die allgegenwärtige Hilfsbereitschaft und das freundliche Arbeitsklima.

Danke geht natürlich auch an meine Familie und Freunde, die für den nötigen Ausgleich gesorgt haben. Ein besonders großes Dankeschön geht an Thorsten sowie an Eva und Sigrid, die in allen Lebenslagen zur Stelle waren.